Using optical coherence tomography to quantify biofilm structure and mass transfer in combination with mathematical modeling

zur Erlangung des akademischen Grades eines
DOKTORS DER INGENIEURWISSENSCHAFTEN (Dr.-Ing.)

der Fakultät für Chemieingenieurwesen und Verfahrenstechnik des
Karlsruhe Institut für Technologie (KIT)
genehmigte

DISSERTATION
von
M.Sc. Chunyan Li
aus Anhui, China

Referent: Prof. Dr. Harald Horn

Korreferent: Prof. Dr. Marc Wichern

              Prof. Dr. Susanne Lackner

Tag der mündlichen Prüfung: 17.12.2015

Abstract

As the dominant life form of microorganisms on Earth, biofilms play a significant role in global ecology. Despite the various risks associated to them, beneficial use of biofilms contributes significantly to the welfare of our society. There is great interest in visualizing as well as quantifying the biofilm structures as the structure is closely related to its function. Various imaging tools, such as confocal laser scanning microscopy (CLSM), magnetic resonance imaging (NMR), have been applied for the investigation of biofilm structure. However, there is no universal approach that can meet the requirements of every application. Meanwhile, mathematical modeling has become an indispensable tool to improve our mechanistic understanding of biofilm processes. However, there have been seldom studies connecting these two major approaches that are often used separately.

Instead of the common practice of two dimensional (2D) imaging with OCT, the great potential of optical coherence tomography (OCT) in three-dimensional (3D) imaging was explored In the present study to monitor the development of biofilm structure on carriers of different geometries (honeycomb) used in lab-scale moving bed biofilm reactors (MBBRs). Biofilm images were taken regularly with light microscope (2D) and OCT (3D). For the first time, the structure of biofilms on carriers in MBBRs was visualized in 3D and its temporal development was tracked. The biofilms established faster on the carriers with smaller compartment size. The carriers with bigger compartment size could hold more biomass when the carriers were fully filled. Comparison between biofilm development under different aeration rate revealed favored faster initial growth at the low aeration rate. 2D imaging can replace 3D imaging to monitor the evolution of biofilm thickness and filling degree before the carrier compartments were blocked with biomass. However, 3D OCT imaging provided more descriptive information, such the heterogeneous biofilm surface, biomass volume, etc. The results proved the great capability of OCT in monitoring biofilm structure development in 3D for its advantages in terms of *in situ*, staining-free, fast image acquisition and compromise between the field of view and image resolution by imaging at the meso-scale.

With the aim of connecting the two basic but often isolated approaches in biofilm research, a biofilm model was successfully developed with OCT cross-sectional images incorporated as the structural template. Hydrodynamics, substrate transport and biochemical reactions were taken into account. The method proved to be a promising approach for biofilm research. The model resulted in detailed simulation of the hydrodynamic conditions and substrate distribution in the vicinity of the liquid-biofilm interface, namely thorough description of the mass transfer boundary layer at micro-scale. Slight difference in biofilm structure led to substantially different local hydrodynamics. The presence of the spikes that make biofilm heterogeneous disturbed the flow, leading to weak

mass transfer. Compared to the flat biofilm structure, biofilms with rough surface structure showed superior performance under the condition of pure diffusive mass transport due to the extended bulk-biofilm interface providing more contact to substrates. Rough biofilms also exhibited slightly better mass transfer fluxes, under the condition of enhanced mass transfer due to high flow velocity over biofilms which renders the whole biofilm surface to be active.

The combined approach developed in this study was further applied to investigate the impact of the attachment of organic particles onto biofilm surface on mass transfer in a lab-scale flume. The attachment of organic particles of different size classes originating from municipal waste water was visualized with OCT. Estimation of the number of the attached particles revealed loose attachment of few large particles and large amount of closely bounded small particles. The method developed combining imaging and modeling was applied by incorporating selected representative $2D$ cross-sectional images before and after particle attachment for all the particle size classes. The model included the processes of fluid flow, substrate transport and biochemical conversion of the substrates. The results from this study provides for the first time a mechanistic explanation for the reduced removal of the dissolved substrates after the attachment of the particles at biofilm surface that have been observed for decades. The presence of the organic particles at biofilm surface affected the flow over the biofilm surface and forced the concentration boundary layer to shift towards the bulk liquid. Therefore, the mass transfer from bulk liquid into biofilm matrix was hindered, with mass transfer flux reduced by 20% for the small particles.

Zusammenfassung

Biofilme sind die dominanteste Lebensform auf Erden und spielen somit eine bedeutende Rolle in der globalen Ökologie. Trotz der verschiedenen mit ihnen verbundenen Risiken, kann die sinnvolle Verwendung von Biofilme einen beachtlichen Beitrag für das Wohl unserer Gesellschaft leisten. Da die Biofilmstruktur stark mit dessen Funktionen zusammenhängt, besteht ein großes wissenschaftliches Interesse an der Visualisieren und der Quantifizieren der Biofilmstruktur. Verschiedene bildgebende Methoden, z.B. Konfokalen Laser-Scanning-Mikroskop (CLSM), Magnetresonanzbildgebung (MRI), werden bereits für die Untersuchung von Biofilmstrukturen eingesetzt. Allerdings gibt es keine allgemeingültige Vorgehensweise für die Untersuchung von Biofilmen, die die Anforderungen jeder Anwendung erfüllen kann. Inzwischen ist die mathematische Modellierung zu einem notwendigen Werkzeug für das bessere Verständnis von Biofilmprozessen geworden. Es gibt jedoch kaum Studien, die die beiden genannten Methoden, die oft getrennt angewendet werden, kombinieren.

In der vorliegenden Studie wurde das große Potenzial der optischen Kohärenztomographie (OCT) in der dreidimensionalen (3D) Bildgebung von Biofilmen untersucht, komplementär zu der üblichen angewendeten zweidimensionalen (2D) Bildgebung mittels OCT. Durch diesen experimentellen Ansatz kann die Entwicklung der Biofilmstruktur auf Trägermaterialein (mit Waben) verschiedener Geometrien zeitaufgelöst beobachtet werden welche in einem Moving Bed Biofilm Reaktor (MBBR) im Labormaßstab kultiviert worden sind. Für das Monitoring der Biofilmstruktur wurden Bilder mittels einem Lichtmikroskop (2D) und OCT (3D) aufgenommen. Wobei die das zeitliche aufgelöste Monitoring von Biofilmen auf Trägermaterialen zum erstem mal in 3D visualisiert wurde. Die Ergebnisse zeigen, dass sich die Biofilme schneller auf Trägermaterialien etablieren, die eine kleinere Wabengröße aufweisen. Im Gegensatz dazu, können Trägermaterialen mit größerer Wabengröße mehr Biomasse halten, wenn die Träger vollständig gefüllt sind . Die Biofilme wurden unter verschiedenen Belüftungsraten kultiviert um den Einfluss auf das Wachstum der Biofilme zu untersuchen. Die Ergebnisse zeigen, dass bei niedrigen Belüftungsraten, das initiale Biofilmwachstum begünstigt ist. Für das Biofilmmonitoring, könnte die Bildgebung in 2D mit dem Lichtmikroskop, die 3D Bildgebung ersetzten um die Biofilmdicke und den Füllungsgrad des Trägermaterials mit Biomasse zu beobachten. Dies ist jedoch nur so lange praktikabel bis der Träger komplett mit Biofilm gefüllt ist. Trotzdem bietet die 3D Bildgebung mittels OCT mehr deskriptive Informationen, wie z.B. die heterogene Biofilmoberfläche, das Volumen der Biomasse usw. Die Ergebnisse bestätigen das große Potential uns die Leistung der OCT Methode für die Beobachtung der Entwicklung von der Biofilmstruktur in 3D. Die Bildgebnung mittels OCT ist komplett in-situ, keine Anfärbung ist nötig und die Aquise von Bildern ist sehr schnell. Desweiteren hat das OCT den Vorteil auf der Meso-skala Bilder erheben zu können, was einen Kompromiss zwischen dem Field

of View und der Bildauflösung darstellt.

Um die beiden grundlegenden, aber oft isolierten, Ansätze in der Biofilmforschung zu verbinden, wurde ein Biofilmmodell erfolgreich entwickelt, das echte Biofilmstrukturen durch das Integrieren von OCT-Schnittbildern berücksichtigt. Weiterhin bindet es Hydrodynamik, Stofftransport und biochemische Reaktionen ein. Dieses Modell erwies sich als ein vielversprechender Ansatz für die Biofilmforschung. Das Modell ermöglicht eine detaillierte Simulation der hydrodynamischen Bedingugnen und der Substratverteilung in der Nähe der Biofilm-Bulkwasser-Grenzfläche Dabei ist die gründliche mathematische Beschreibung der Massentransfergrenzschicht auf der Mikroskala essentiell. Die Ergebnisse zeigen, dass kleine Änderungen in der Biofilmstruktur einen erheblichen Unterschied in der lokalen Hydrodynamik bedingen. Beispielsweise führt eine heterogene Biofilm-struktur mit hervorragenden Biofilmteilen durch die Störung des Flussfeldes zu einem verminderten Stofftransport. Im Vergleich zu glatten Biofilmstrukturen, zeigen raue Biofilmoberflächen eine bessere Performance in Diffusions dominierten Bedingungen. Dies ist durch die erweiterte Grenzfläche zwischen der Flüssigkeit (Bulkwasser) und dem Biofilm zu erklären, die mehr direkten Kontakt mit den Substraten ermöglicht. Eine raue Biofilmstruktur bedingt weiterhin leicht verbesserten Stofftransport durch höhere Strömungsgeschwindigkeiten an der Biofilmoberfläche, welche die gesamte Aktivität des Biofilms steigert.

Der in dieser Studie entwickelte kombinierte Ansatz wurde weiterhin angewendet, um die Auswirkungen von organischen Partikeln, die auf der Biofilmoberfläche gebunden sind, auf dem Massen-transfer in den Biofilm (unter Strömungsbedingungen) im Labormaßstab zu untersuchen. Die Anlagerung der organischen Partikel verschiedener Größenklassen, gewonnen aus kommunalem Abwasser, wurde mittels OCT visualisiert. Die Ergebnisse zeigen, dass wenig große Partikel an den Biofilm anlagern, diese jedoch locker gebunden sind. Im Gegensatz lagern sich viele kleine organische Partikel an, die wiederum fester angebunden sind. Die entwickelte Kombination von Bildgebung und Modellierung wurde durch die Integration von ausgewählten repräsentativen 2*D* Schnittbilder vor und nach der Befestigung der Teilchen von aller Größenordnung realisiesiert. Das Modell umfasst die Prozesse der Fluidströmung, den Massentransport und die biochemische Umwandlung von Substraten in dem Biofilmsystem. Die Ergebnisse dieser Studie liefern erstmals eine mechanistische Erklärung der schon seit Jahrzehnten beobachten Phänomene, nämlich der verminderten Entfernung der gelösten Substrate nach der Anlagerung der organischen Partikel an Biofilmoberfläche. Das Vorhandensein der organischen Partikeln an der Biofilmoberfläche beein-flusst die Strömung über die Biofilmoberfläche und zwing die Konzentrationsgrenzschicht zu einer Verschiebung in Richtung Bulk. Aus diesem Grund wird die Massenübertragung von dem Bulk-wasser zur Biofilmmatrix hin behindert. Der Stoffaustauschfluss verringert sich um 20 % wenn kleine organische Partikel angelagert sind.

Acknowledgment

My favorite, not one of, explanation of PhD is **P**ermanent **H**ead **D**amage. As my head has probably been damaged enough, it's time to finish this special phase of life. During this process, I received countless help from many, many people. Although it is only my name that appears on the cover, I would like to thank all of you for being there for me.

First of all my most sincere gratitude to Prof. Horn. You are the reason for me to be in Karlsruhe. You provided me a free environment to choose what I want to do and offered full support whenever it is needed. Many thanks to Prof. Wichern for taking your time to reviewer my thesis.

Michael, how to express my gratitude to you? From lab to image analysis, to manuscript writing, to correction, to all the daily details, whenever there was a problem that could not be solved by myself, the first one that came to my mind to ask for help was always you. And you almost always had a solution. I was always amazed how it was possible for you to pay so much attention to the details, so small mistakes. Whenever a piece of writing came back from you, it was full of red comments. :D Without your comments, my work could not have been possible to be accepted by the journals. Also as friends, thank you and Steffi so much for your help repairing bike, offer to talk and to help at tough times, for example about Fahrschule.

Many, many thanks to Susanne. Your lovely personality attracts people to be around you. Talking to you is always enjoyable. It is so amazing to me that how you could have achieved so much in research and still have made your hobby to Olympic level. Respect!!! Discussion with you is always fruitful. Your questions and suggestions drove me to think more.

Many thanks to Frau Abbt-Braun for your support and encouragement. I used your trick on how to reply tough questions at the IWA conference. It worked pretty well. ;) Also thank you for your explanations of German culture. Many thanks to Frau Schäfer for your support. Whenever I came to you, you can solve all my problems. Sylvia, our friendship will last. You promised to come to visit my parents. They are waiting for you in China.

Axel, thank you very much for your help setting up the reactor, for your explanation about German culture, for bringing me to Taekwondo course... Leider habe ich deine Kürbissuppe Rezept verloren. Elly, my sister, there is always so much fun whenever you are around. We miss the source of fun. We miss you. I enjoyed so much guiding the Praktikum with you. Dunja, many, many thanks for your help with computer staff, finding a free bike for me, for the hot water delivery service, for .... A lot to thank for. Uli and Reinhard, thank you for helping me bring sludge and wastewater from Neureut. Mattias, thank you for your help in TOC measurement. Rafael, although there is not much overlap between our work, I thank you for always give me a big smile.

Sharing one office with Pia is one of the most lucky experiences I ever had. Pia, you are an incredibly open, optimistic, energetic and lovely office mate, as I have told you many times already. We talked about family members, about clothes, about movies, about complaints, about politics once in a while, about future, about everything. You always cheered me up when I was low. You offer help without being asked. You are full of ideas. You are just incredible. Pia, I will miss you.

Jueying, Di and Meijie, being $8000\,km$ away from home, it feels so nice to have someone to talk Chinese. I thank you all for your accompany, which makes me feeling not totally disconnected from Chinese culture. Eva, I owe you a lot. From the very beginning till the end of your stay here, when I came to your office, the first thing you asked was always "What can I do for you?". You are incredibly intelligent and hardworking. You will rock EnviroChemie. Shelesh, I strongly believe that you have perpetual engine installed in your body. Fabi, you are so cute. I enjoyed the time for the particle experiments with you. Mark, I never get bored teasing you :D. Florian, you are a super confident genius. Thank you for the discussions on OCT usage. Elham, you know that I love you, right ;)? Dominik, I am impress by your determination to be a vegan, especially the reason behind. I don't think I can ever do that. Respect!!! Thank you all for being supportive, for the lovely atmosphere in the institute. Laure, Oliver and Isa, wish you all the best for your PhD.

Andrea, Marius, Ulrike, Florencia, Frau Gordalla, although there is no overlap between our work, it was so pleasant to talk to you. Thank you for the lovely talks, for caring about my problems, for offering help.

There are no words to express my gratitude to Prof. Wolfgang Geiger. You changed my life track. Without your guidance and help, I am just one ordinary Chinese girl staying and leading an ordinary life in China. Without your financial support to bring me to Germany, I could not have the opportunity to come out of China to see the bigger world, let along to go for master and PhD. This needs to be paid back throughout my life time.

Last but not least, my gratitude to my family. Lost the opportunity to go to university himself due to historical reasons, my dad had all his expectations on me. So far, I did not let him down. Meanwhile, it was not until this spring when my mom went to hospital have I realized that they really needed me. My sister is great. She protected me by telling my mom not to ask me too often when I would finally get married. I owe my brother big thanks for the fact that he has 3 kids for my parents to be busy with therefore less time to care too much about me.

Publication

Chapter 4 and 7 of this dissertation have been published in the two peer reviewed articles.

Li C., Felz S., Wagner M., Lackner S. and Horn H. (2016). Investigating biofilm structure developing on carriers from lab-scale moving bed biofilm reactors based on light microscopy and optical coherence tomography. Bioresour Technol 200, $128 - 136$

Li C., Wagner M., Lackner S. and Horn H. (2015). Assessing the influence of biofilm surface roughness on mass transfer by combining optical coherence tomography and two-dimensional modeling. Biotechnol Bioeng. *in press. DOI* : $10.1002/bit.258$

Contents

List of Tables

List of Figures

Nomenclature

Abbreviation

CA	cellular automata	
CLSM	confocal laser scanning microscopy	
COD	chemical oxygen demand	$(mg \cdot L^{-1})$
CP-OCT	cross-polarization OCT	
CV	crystal violet	
DO	dissolved oxygen	$(mg \cdot L^{-1})$
EPS	extracellular polymeric substances	
FISH	fluorescene *in situ* hybridization	
FR	filling ratio	
FSI	fluid-structure interaction	
H	heterotrophic biomass	
HRT	hydraulic retention time	
IbM	individual-based model	
LM	light microscopy	
MBBR	moving bed biofilm reactor	
MRM	magnetic resonance microscopy	
MRI	magnetic resonance imaging	
OCT	optical coherence tomography	
Ω_B	biofilm domain in the model	
Ω_L	liquid domain in the model	
QS	quorum sensing	
SD-OCT	spectral-domain OCT	
SE	surface enlargement factor	
SEM	scanning electron microscopy	
UMCCA	unified multi-component cellular automaton	
T_2	spin-spin relaxation	(s)
TSS	total suspended solids	$(g \cdot L^{-1})$

Mathematical symbols

A	biofilm area	(mm^2)
α	surface enlargement factor	$(-)$
BV_{3D}	biomass volume in one compartment	(mm^3)
$BV_{A,tot}$	total biomass volume on Carrier A	(mm^3)
$BV_{B,tot}$	total biomass volume on Carrier B	(mm^3)
D_{COD}	diffusivity of COD in water	$(m^2 \cdot s^{-1})$

D_{O_2}	diffusivity of O_2 in water	$(m^2 \cdot s^{-1})$
d_P	particle diameter	(μm)
η_{2D}	compartment coverage based on $2D$ images	$(\%)$
η_{3D}	compartment coverage based on $3D$ images	$(\%)$
Φ	biofilm porosity	$(-)$
h_{no}	average thickness above the reference plane before particle attachment	(μm)
h_{with}	average thickness above the reference plane after particle attachment	(μm)
$h_{particle}$	average thickness of the particle layer	(μm)
J_{COD}	COD flux	$(g \cdot m^{-2} \cdot d^{-1})$
J_C	local convective flux	$(g \cdot m^{-2} \cdot d^{-1})$
J_D	local diffusive flux	$(g \cdot m^{-2} \cdot d^{-1})$
J_{O_2}	oxygen flux	$(g \cdot m^{-2} \cdot d^{-1})$
$\bar{J}_{O_2}$	mean oxygen flux over the liquid-biofilm interface	$(g \cdot m^{-2} \cdot d^{-1})$
K_{COD}	half-saturation coefficient for COD	$(g \cdot m^{-3})$
K_{DO}	half-saturation coefficient for DO	$(gO_2 \cdot m^{-3})$
k_L	mass transfer coefficient	$(m \cdot d^{-1})$
L_f	biofilm thickness	(μm)
$\bar{L}_{f,2D}$	mean biofilm thickness based on $2D$ images	(μm)
$\bar{L}_{f,3D}$	mean biofilm thickness based on $3D$ images	(μm)
L_C	concentration boundary layer thickness	(μm)
L_h	the characteristic length used to calculate Sh	(mm)
L_S	the length of the substratum	(mm)
L_Γ	length of the liquid-biofilm interface	(mm)
m_0	mass of the empty pycnometer	(g)
m_1	mass of the pycnometer filled with water	(g)
m_2	mass of the pycnometer filled with the particles	(g)
m_3	mass of the pycnometer filled with particles and water	(g)
μ	dynamic viscosity of the liquid	$(N \cdot s \cdot m^{-2})$
μ_H	maximum specific growth rate of X_H	(d^{-1})
M_W	molecular weight	(kDa)
P	pressure	(Pa)
ΔP	pressure drop	(Pa)
P_Γ	perimeter	(μm)
R_a	surface roughness	(μm)

R'_a	roughness coefficient	$(-)$
r_i	turnover rate of substrate i	$(g \cdot m^{-3} \cdot d^{-1})$
ρ	liquid density	$(kg \cdot m^{-3})$
ρ_w	density of water	$(kg \cdot m^{-3})$
ρ_s	density of the particulate organic matter	$(kg \cdot m^{-3})$
SA_{3D}	area of liquid-biofilm interface	(cm^2)
$SA_{A,tot}$	total area of liquid-biofilm interface on Carrier A	(cm^2)
$SA_{B,tot}$	total area of liquid-biofilm interface on Carrier B	(cm^2)
SE_{2D}	surface enlargement based on $2D$ images	$(-)$
SE_{3D}	surface enlargement based on $3D$ images	$(-)$
Sh	Sherwood number	$(-)$
$\overline{Sh}$	spatially average Sherwood number	$(-)$
S_i	concentration of substrate i	$(mg \cdot L^{-1})$
$S_{i,0}$	concentration of S_i in bulk liquid	$(mg \cdot L^{-1})$
$S_{i,\Gamma}$	concentration of S_i at liquid-biofilm interface	$(mg \cdot L^{-1})$
Γ	liquid-biofilm interface	
$\mathbf{u}$	velocity field in the domain	$(m \cdot s^{-1})$
$u_{f,2D}$	biofilm growth velocity based on $2D$ images	$(\mu m \cdot d^{-1})$
$u_{f,3D}$	biofilm growth velocity based on $3D$ images	$(\mu m \cdot d^{-1})$
V_b	biovolume	(μm^3)
X_H	density of heterotrophic biomass	$(g \cdot m^{-3})$
Y_H	yield coefficient of heterotrophic biomass on substrate	$(g \cdot g^{-1})$
$\overline{\delta_b}$	mean concentration boundary layer thickness	(μm)

Chapter 1

Introduction

Biofilms are essentially microorganisms embedded in a matrix of extracellular polymeric substances (EPS) of their own origin (Flemming and Wingender, 2010). As the dominant form of microbial life on earth (Wuertz et al., 2003), the presence of biofilms can cause severe problems in various field, such as infections in the medical field, health issues related to deterioration due to bacteria in food and beverage industry, biocorrosion on metal surface and biofouling on membranes used for drinking water production. However, beneficial use of biofilms can also contribute to the welfare of our society, such as bioreactors for waste water treatment, subsurface biofilm barriers for the remediation of groundwater containment (Cunningham et al., 2003), etc. Compared to the planktonic lifestyle, aggregating into thin biofilm at interfaces offers the advantages to protect microorganisms against, i.e. desiccation, antibiotics and protozoa (Flemming and Wingender, 2010). According to Stoodley et al. (1997) a distinctive characteristic that separates biofilms from planktonic lifestyle is the structural organization. Biofilms can exhibit smooth and flat, rough, fluffy or filamentous structures (Flemming and Wingender, 2010). Mushroom-like macrocolonies and biofilm streamers have also been reported (Klausen et al., 2003; Stoodley et al., 1998b). The EPS matrix contains diverse biopolymers, such as polysaccharides, proteins, extracellular DNA, lipids and water (Flemming and Wingender, 2010). Although a single strain of bacteria may form biofilm, most of biofilms in nature are composed of several species (Yang et al., 2011; Patel et al., 2005). However, the chemical composition and bacterial community structure are not the focus in the current study. The topic is restrained to the physical structure and morphology of biofilms. The physical structure also exerts significant impact on the immediate environment, most prominently on the local hydrodynamics (Picioreanu et al., 2000). This interaction between biofilm structure and the surrounding environment is of great importance to understand the biofilm processes, thus of great interest in biofilm research. On the one hand, much effort has been made to visualize as well as to quantify the physical structure of biofilms through imaging with different image techniques. On the other hand, modeling of biofilms with different analytical and mathematical models has con-

tributed tremendously to the understanding of the processes and mechanisms related to biofilms. However, these two approaches are mostly used separately. There is an urgent need to connect the two separated approaches for the study of biofilm processes.

1.1   Biofilm structure

The physical structure of biofilms is influenced by various factors, including substrate surface loading (Flemming and Wingender, 2010; van Loosdrecht et al., 1995; Stoodley et al., 1998a), hydrodynamic conditions (Stoodley et al., 1998a; Wagner et al., 2010b; Telgmann et al., 2004), microbial community structure (van Loosdrecht et al., 1995), inter-cellular communication (Flemming and Wingender, 2010; Purevdorj et al., 2002), predation by protozoa (Derlon et al., 2012), surface properties of the substratum (Heijnen et al., 1992; Carlén et al., 2001; Percival et al., 1999; Artyushkova et al., 2015; Battin et al., 2007), the type of substrate used (Villasenor et al., 2000; Srinandan et al., 2012) as well as the concentration of the ions presents (Eldyasti et al., 2013). Besides these influencing factors at macro-scale, quorum sensing (QS) at cell scale has also been found to impact the formation of *P. aeruginosa* biofilms (Davies, 1998; Kievit, 2009; Purevdorj et al., 2002).

Based on the observation of different biofilm morphologies developed on the carriers in biofilm airlift suspension reactors, van Loosdrecht et al. (1995) postulated that the two major governing forces forming biofilm structures were the flux of nutrients into the biofilm and the detachment rate induced by shear stress. Many biofilm processes are influenced by hydrodynamics, since the hydrodynamic conditions determine mass transfer and fluid induced shear stress. In the experiment of Lewandowski and Walser (1991) the maximum thickness of a mixed-culture biofilm was achieved near the transition between laminar and turbulent flow. Both higher and lower Reynolds numbers led to reduced biofilm thickness. Thus, the authors hypothesized that an optimal hydrodynamic conditions might exist. Above this level high detachment rate hinders the accumulation of biomass, while below this rate biofilm growth is limited by mass transfer. The mixed-species biofilms cultivated by Stoodley et al. (1998a) with limiting glucose showed significant differences in their morphology. Under laminar flow conditions biofilm were patchy and characterized by interstitial voids that separate the roughly circular cell clusters. The biofilms under turbulent flows developed ripples and elongated 'streamers'. And the streamers oscillated in flow. Wagner et al. (2010b) imaged the heterotrophic biofilms fed with methanol grown on glass slides under laminar, transient and turbulent flow conditions. The visual impression revealed heterogeneous structures for biofilms in both laminar and transient flow and more homogeneous structure for biofilms under turbulent flows. The biofilms were substantially different with porosity of 0.65 for the heterogeneous biofilms grown at laminar and transient flow conditions and 0.36 for biofilms under turbulent

flow conditions.

Another major influencing factor is related to substrate loading, which influences not only the thickness but also the compactness of biofilms (Stoodley et al., 1998a; Wijeyekoon et al., 2004; Fu et al., 2010). Denser and thinner biofilms with low porosity are expected with high substrate loading and low substrate loading leads to thicker but looser biofilms with high porosity and significant amount of filamentous bacteria present (Wijeyekoon et al., 2004; Fu et al., 2010). Stoodley et al. (1998a) observed rapid growth of ripples and oscillating streamers into compact biofilms when glucose concentration was increased from 40 to $400\,mg \cdot L^{-1}$ for 21 days old biofilms under turbulent conditions, as well as the increase of the maximum biofilm thickness from 30 to $130\,\mu m$. The process was reversible and the patches of ripples were reestablished by reducing the glucose concentration back to $40\,mg \cdot L^{-1}$. The simulation of Picioreanu et al. (1998) with the hybrid discrete-differential approach revealed that porous biofilms with 'finger-like' colonies developed in a substrate transfer limited regime and compact and dense biofilms were obtained at high substrate-transfer rate.

Not only the loading of substrate, but also the type of substrate used has a direct impact on biofilm structure. In biofilm airlift suspension reactors fed with different carbon substrate more dense biofilms were observed with more reduced substrates or substrates that allow a lower biomass growth rate (Villasenor et al., 2000). Experiments by Srinandan et al. (2012) concluded that the frequently used carbon sources influenced not only the nitrate removal efficiency, but also the structure of biofilms formed. The biofilms fed with acetate and ethanol were characterized by voids. Compact and dense biofilms were established, when the reactors were fed with glucose and methanol.

Disturbances are inevitable for many natural and engineered biofilms, such as hydraulic shocks, dose of biocides or predation by higher organisms. Predation directly alters the biofilm structures (Derlon et al., 2012; Böhme et al., 2009). Compact and thick biofilms covered the membrane surface in absence of predators. Predation by protozoa on biofilms developed on gravity-driven ultrafiltration systems resulted in open and heterogeneous biofilm structures, which increased the permeate flux substantially (Derlon et al., 2012). Depending on the predators, the effect of grazing on the biofilm structure varies (Böhme et al., 2009). Operated in small flow cells, larger microcolonies were promoted by *Dexiostoma campylum* in comparison to ungrazed biofilms. The presence of *Chilodonella. uncinata* and *Spumella sp.* resulted in reduced biofilm volume, but increased biofilm porosity and biofilm surface to volume ratio, which might improve the mass transfer of nutrients to the biofilm base under slow flow conditions (Böhme et al., 2009). Disturbances through pulse injection of biocide monochloramine revealed that the disturbance frequency affected the biofilm morphology. In the daily treated reactor, the biofilms was morphologically simple and stable. While the weekly treated biofilms could quickly reestablish the complex structure before the next pulse injection (Milferstedt et al., 2013).

The presence of different ions, such as Ca^{2+} and Mg^{2+}, exerts significant impact on biofilm struc-

ture (Eldyasti et al., 2013; Goode and Allen, 2011; Song and Leff, 2006; Huang and Pinder, 1995). Below certain range, the increase of Ca^{2+} concentration in the growth medium resulted in increased biomass accumulation (Huang and Pinder, 1995). There is significant difference in the surface shape and structures of biofilms at different Ca^{2+} concentrations. Patchy and fluffy structure were observed at low Ca^{2+} concentration for biofilms developed in lab-scale denitrifying fluidized bed bioreactors. Compact and uniform round-shape biofilms were present at high Ca^{2+} concentration (Eldyasti et al., 2013). Huang and Pinder (1995) suggested Ca^{2+} concentration between 100 to $120 \, mg \cdot L^{-1}$ to be the optimum for the substrate consumption by biofilms formed by anaerobic acidogenic in fixed-bed recycle reactors.

1.2   The application of MBBRs
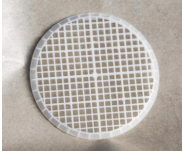
As a promising process, MBBR incorporate plastic carriers into waste water treatment process to adopt the favorable features of suspended growth as well as the fixed-biofilm process (Ødegaard, 2006). The carriers provide large protected surface area for microorganisms to attach and grow on. Compared to the convectional activated sludge system, MBBR offers the benefits of being compact, easy maintenance due to no sludge recirculation, flexibility in upgrading by varying the filling ratio of the carriers used, utilization of specialized biofilms for carbon and nitrogen removal (Ødegaard, 2006; Andreottola et al., 2000). Due to these benefits, it has gained more and more popularity for waste water treatment. Till 2006 there has been more than 300 plants in operation or under construction worldwide (Ødegaard, 2006). The process can be incorporated into aerobic, anoxic or anaerobic processes, for BOD removal, nitrification and denitrification for municipal as well as industrial waste water treatment.

Intensive research on MBBRs has been devoted to the carrier filling ratio (FR) (Feng et al., 2012; Calderón et al., 2012; Gu et al., 2014; Wang et al., 2005), microbial community analysis (Almstrand et al., 2014; Zhang et al., 2013), the influence of carrier geometry (Levstek and Plazl, 2009), hydrodynamics in the reactors (Nogueira et al., 2015), mathematical simulation of the processes (Alpkvist et al., 2007; Plattes et al., 2007, 2008). As a key design parameter, Ødegaard (2006) recommended the FR lower than 70% when K1 carrier (see Table 1.1) is used to make sure the carriers move freely in the reactor. Studies by Wang et al. (2005), Calderón et al. (2012) and Gu et al. (2014) with different types of carriers under diverse reactor environmental conditions to treat different waters concluded on the same optimal FR of 50%. The combination of cryosectioning and fluorescence *in situ* hybridization (FISH) was adopted to study the microbial community shift in biofilm development on the carriers in a nitritation-anammox MBBR (Almstrand et al., 2014). $3D$ stratification was revealed with the domination of aerobic nitrifying bacteria close to the bulk-biofilm interface and the residence of anammox bacteria in the deeper layer of the biofilms.

Currently dozens of types of carriers are available on the market, see Table 1.1 for few examples of carriers from AnoxKaldnes. The carriers show significantly different geometries, so as the protected surface area provided by the carriers. The study of Levstek and Plazl (2009) with two types of carriers with fundamentally different geometry did not provide an answer to the question. Another important design parameter for MBBR process is the biofilm surface area. Manufacturers like to claim high specific surface area of their carriers. Boltz and Daigger (2010) pointed out that excessive growth of biofilm leads to reduction of biofilm surface area. It is still not clear whether it is the specific surface area or the effective biofilm surface area after biofilm growth that determines the performance of the process.

Table 1.1: Examples of biofilm carriers

		$K1$	$K3$	$K5$	$ChipP$	$ChipM$
Photo						
Diameter	mm	10	25	25	45	48
Thickness	mm	7	10	3.5	3	2.2
Area	$m^2 \cdot m^{-3}$	500	500	800	800	120

Dealing with MBBR, it is often assumed that the concentration of suspended solids is too low to be accounted for. However, according to Piculell et al. (2014) the contribution of the suspended biomass to the total reactor performance shall not be overlooked. Furthermore, the constant movement of biofilm carriers result in complex hydraulic conditions in the reactor(s), which has not been well understood and characterized (Boltz and Daigger, 2010). Nogueira et al. (2015) proceeded one step further in describing the mass transfer characteristics by developing a method to determine the external mass transfer coefficient, which was found to vary substantially depending on the mixing intensity in the reactor.

Ødegaard (2006) provided simple qualitative description of biofilm structure in MBBR process. High substrate loading resulted in compact biofilms. Fluffy biofilms are promoted by low substrate loading. So far there has been no study investigating the structure of biofilms developed on the carriers. With the various image tools available, the biofilm structures shall be investigated to extend the understanding of the process.

1.3   Visualization of biofilm structure

Imaging with different optical and spectroscopic techniques has become an indispensable tool in biofilm research to qualitatively visualize the structure of biofilms, which otherwise is not visible

to bare eyes, as well as to quantitatively characterize the biofilm structure. Various imaging techniques such as light microscopy (LM), magnetic resonance imaging (MRI), confocal laser scanning microscopy (CLSM) and scanning electron microscopy (SEM), have found wide applications in biofilm research. As a natural characteristic of biofilms, both the visualization and quantification of heterogeneity vary significantly from micrometers (cellular level) up to centimeters (microbial mats) (Lewandowski et al., 1999; Murga et al., 1995; Milferstedt et al., 2006). Morgenroth and Milferstedt (2009) proposed the concept of different spatial scales in biofilm research: micro-, meso- and macro-scale. It is possible that biofilms may show greater heterogeneity at the meso-scale due to the presence of cell clusters and interstitial voids. Meanwhile it can also appear to be homogeneous at the micro-scale due to the fact that the images taken at the micro-scale ($< \mu m$) can cover only small field of view thus being not representative and at the macro-scale that the micro-channels separating cell clusters may become imperceptible thus not contributing to the heterogeneity detected (Gjaltema et al., 1994; Milferstedt et al., 2008). Therefore linking the different scales can provide a more comprehensive understanding of structural characteristics of biofilms. Wagner et al. (2010b) classified the often used imaging techniques, such as SEM, CLSM, OCT, MRI and LM, according to their field of view and their suitability corresponding to the concept of the spatial scales proposed by Morgenroth and Milferstedt (2009). Based on extensive literature review and the experience dealing with biofilm imaging, the techniques were compared from several aspects, provided in Table 1.2.

Table 1.2: Summary of the applications of different imaging techniques in biofilm structure characterization

	Dimen.[1]	Scale	L_f	Reso.[2]	Inva.[3]	*In situ*	Speed	Species[4]	Cost.[5]
SEM	2D	Micro	surface	High	Yes	No	Slow	No	High
CLSM	3D	Micro	$< 200\,\mu m$	High	Yes	No	Slow	Yes	High
MRI	3D	Meso	$> 500\,\mu m$	Low	No	No	Slow	No	High
OCT	3D	Meso	$\sim 500\,\mu m$	Middle	No	Yes	Quick	No	Middle
LM	2D	Macro	~$100\,\mu m$	Low	No	Yes	Quick	No	Low

1. Dimen. is the abbreviation of dimension. 2. Reso. denotes resolution. 3. Inva. tells if the technique is invasive to biofilm structure or not. 4. Species indicate if the imaging technique can distinguish bacteria species. 5. Cost. stands for instrumental cost.

Biofilm properties at the micro-scale have been relatively well studied with different approaches. According to Milferstedt et al. (2009), to relate biofilm structural information to mass transport phenomena, a characteristic length of $400\,\mu m$ in biofilm images is required. This length scale lies in the range of the meso-scale, which is the focus of the current study. According to Wagner et al. (2010b), MRI and OCT are the suitable candidates for the investigation of biofilms at the meso-scale.

1.3.1 Imaging using MRI

In the past decades, there has been wide applications of MRI in biofilm research (Manz et al., 2003; Herrling et al., 2014; Phoenix et al., 2008; Ramanan et al., 2013). Large field of view of MRI renders it to be suitable for biofilm structure characterization at the meso-scale proposed by Morgenroth and Milferstedt (2009) and Wagner et al. (2010b). It allows non-invasive and even on-line measurement of biofilm development (Wagner et al., 2010b). It is especially suitable for the investigations on biofilms that are too thick for photo based imaging (Ramanan et al., 2013).

In the study of Manz et al. (2003), the surface structural data of heterotrophic biofilms cultivated in tube reactors were spatially resolved based on T_2 (spin-spin relaxation) weighted images. The biofilms on the complete cross section of the tubes were quantified with respect to mean biofilm thickness ($\overline{L}_f$) and surface roughness coefficient (R_a') under both flow and stagnant conditions. Gjersing et al. (2005) presented a series of time lapse T_2 maps, which illustrated the structure of biofilms within a capillary bioreactor as a function of growth. Visualization of biofilm structure has been conducted by several other studies too (Ramanan et al., 2013; Herrling et al., 2014).

In addition to revealing the heterogeneous biofilm structures, MRI is capable of mapping flow field around the biofilm structure (Wagner et al., 2010a; Gjersing et al., 2005; Herrling et al., 2014) as well as to investigate transport behavior in and around biofilm matrix (Phoenix et al., 2008; Ramanan et al., 2013; Cao et al., 2012), which is of great importance in biofilm research. Those studies have demonstrated MRI to be a powerful tool to image the structure of biofilms non-invasively in large scale, characterizing flow condition in $3D$ and mass transport phenomenon. However, its application is limited in certain aspects. Due to its high instrumentation cost, it is not readily available for many research institutes and has high requirement on the operation of the instrument as well as the subsequent data analysis (Neu et al., 2010). The relatively low resolution of MRI at submilimeter ($22\,\mu m$) (Ramanan et al., 2013) prevents it from being used to study the heterogeneity at the micro-scale. Meanwhile no differentiation of microbial species can be made based on MRI images.

1.3.2 Imaging using OCT

Originally invented for medical imaging (Huang et al., 1991), OCT has recently been introduced into biofilm research to reliably monitor biofilm development at mm-scale (meso-scale) (Xi et al., 2006). The capability of OCT in the visualization and quantification of biofilm structure has been exemplified by Xi et al. (2006), Haisch and Niessner (2007) and Wagner et al. (2010b). OCT enables fast, *in situ* and non-invasive $3D$ visualization of biofilm structure at meso-scale and thus exhibits high potential in biofilm research. One of the advantages worth to be emphasized is that no biofilm preparation is required. Thereby the structural integrity can be well preserved.

Principle of OCT

Imaging with OCT is analogous to ultrasound imaging. The difference is that OCT employs near-infrared light instead of ultrasound. Essentially the depth-resolved information is acquired by detecting the phase shift of the backreflected and backscattered light from the sample compared to the source light. Figure 1.1 illustrates the system components and the basic principle of OCT. Light from a low-coherence light source is directed to a beam splitter, where the incident light is split into sample and reference arm. Light directed to reference arm travels to the reference mirror and is directed back to the beam splitter. The light in the reference mirror and backscattered light from the sample are combined here. Interference is created. The electronic signals detected are processed. At a focal spot the processed signals provide information on depth-resolved reflectivity, which is called A-scan. An assembly of A-scans, when scanning along one lateral direction, provides a two-dimensional cross-sectional depth profile of the sample, termed as B-scan. Three dimensional volumetric dataset, termed as C-scan, is obtained by scanning along another lateral direction, which is compile of B-scans in the scanning direction.
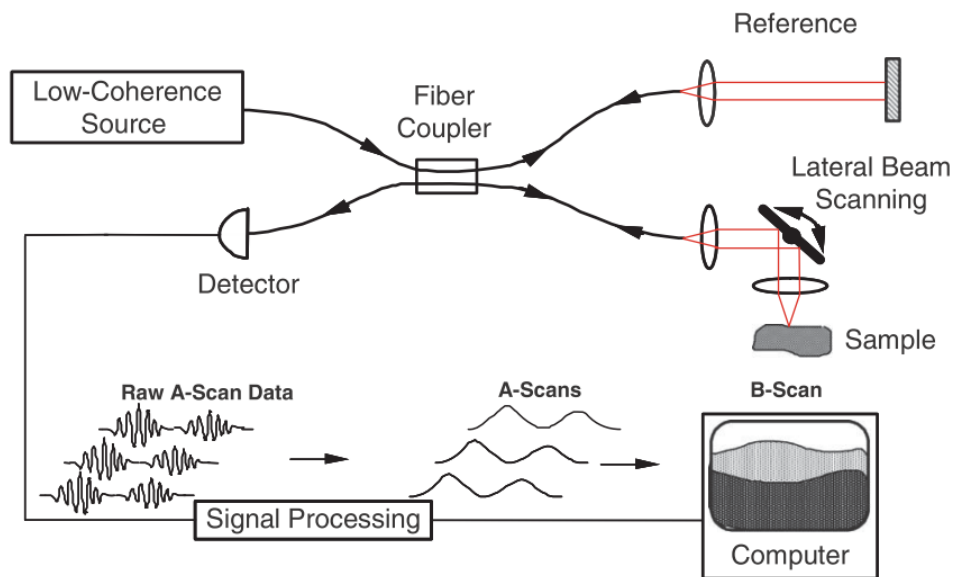
Figure 1.1: A simplified schematic drawing of a generic OCT system (from Drexler and Fujimoto, 2008).

Biofilm structure characterization

First $3D$ visualization of biofilm structure with OCT was achieved by Xi et al. (2006). Time domain OCT with central wavelength at $800\,nm$ was adopted to monitor *P. aeruginosa* PAO1 biofilm growth in a single-channel flow cell. A volume of $1 \times 1 \times 2\,mm^3$ was imaged. Bacterial colonies separated by interstitial voids and water channels were clearly identified in the $3D$ rendered images of biofilm

developed on the inner surfaces of the flow cell. Visual inspection of the images revealed that biofilm on the bottom of the flow cell exhibited more heterogeneous structural features such as "mushrooms". Dynamic monitoring of the biofilm growth revealed incremental increase of biofilm on the bottom of the flow cell. A self-constructed OCT initially for clinic use was adopted by Haisch and Niessner (2007) to monitor biofilm growth as well as the detachment process in a lab-scale tube reactor. Biofilm structures were visualized in both $2D$ and $3D$. By thresholding the pixel intensities, the biofilm structure was presented with a basal layer of high density and upper layer with relative lower density. The property of high-speed image acquisition enabled OCT to observe the dynamic detachment of biofilm by the application of H_2O_2 (0.3%).

Although Xi et al. (2006) and Haisch and Niessner (2007) visualized the biofilm structure in a qualitative manner, no quantification of biofilm structure was conducted. Wagner et al. (2010b) imaged heterotrophic biofilm cultivated under different hydraulic conditions with a SD-OCT with a central wavelength of $930\,nm$. There was distinct difference in biofilm structure between biofilm cultivated under laminar and transient flow conditions (porous matrix and heterogeneous surface) and biofilm cultivated under turbulent flow conditions (compact biofilm matrix and flat surface). The structures were further quantified with respect to biofilm thickness and volumetric porosity. Biofilm cultivated under turbulent flow conditions with a porosity of 0.36 was distinctly different from the biofilms grown under laminar and transient flow conditions with a porosity as high as 0.67.

The structure of biofilms develop on the surface of gravity driven ultrafiltration system was characterized by means of SD-OCT (Derlon et al., 2012, 2013) . Structural parameters, mean biofilm thickness ($\overline{L}_f$), roughness (R_a) and roughness coefficient (R_a'), were calculated based on the $2D$ cross-sectional images. The total amount and also the structure of biofilm were significantly influenced by predation. System with predation developed biofilm with open and heterogeneous structure. The system without predation was homogeneously covered with flat, compact and thick structure (Derlon et al., 2012, 2013). Janjaroen et al. (2013) investigated the mechanisms of *E. coli* attachment onto biofilms fed with groundwater. The meso-scale physical structure of biofilm was analyzed with SD-OCT with a central wavelength of $800\,nm$. After biofilms grew for 8 weeks, it was found that the adhesion rate coefficient was positively correlated to biofilm roughness determined from OCT images.

Quantification of biomass

Attempts have been made by Haisch and Niessner (2007) and Chen et al. (2012) to correlate the pixel intensity to biofilm density. However, no quantification of biofilm density was conducted by the authors. Instead of biofilm density, biofilm biomass was quantified by Chen et al. (2012) with cross-polarization OCT (CP-OCT) for *ex vivo* dental biofilm. They claimed that 99.9% of the original polarization state (P-state) of the reflected light from water surface can be filtered

out by CP-OCT, which allows the measurement of the scattered light from biofilm components. Biofilm biomass was calculated by integrating the scattering intensity. Meanwhile biomass was also quantified with crystal violet (CV). The integration of CP-OCT scattering intensity of biofilm showed very strong positive correlation with the quantification based on CV assay (Spearman's $\rho = 0.92$) during the growth phase of the biofilm. However, after biofilms grew mature (thicker than $500\,\mu m$), biofilms became too thick to be penetrated by OCT due to light attenuation. In this case the integration of scattering intensity showed very low correlation with the biomass quantified with CV assay.

1.3.3   Comparison of the imaging techniques

Each technique has its advantages and drawbacks. Information extracted from the macro- and meso-scale approaches are useful for the analysis of the large features. While the approaches at micro-, even nano-scale, can provide detailed information at intracellular domain. Selection of the appropriate imaging technique depends on many factors, such as the features desired to investigate, the availability of the instrument, the capability of the staff to operate the instrument and appropriate image analysis afterward. As the meso-scale properties are the focus of this study, the emphasis was paid to the comparison of the applicability of MRI and OCT. Both MRI and OCT are not invasive to biofilm structure. The resolution of MRI images is much lower than that of OCT images. The high instrumental cost and long time needed for image acquisition limits the application of MRI, especially for time series imaging to track the development of biofilms. On the contrary, the relatively low instrumental cost, higher resolution, fast image acquisition renders OCT to be the optimal technique for the investigation of the temporal development of biofilm characteristics at the meso-scale.

1.4   Quantification of biofilm structure based on image analysis

Biofilm images obtained with aforementioned imaging techniques provide researchers the opportunity to visualize the biofilm structures cultivated under different environmental conditions. They can be further analyzed to provide the basis for quantitative evaluation, for example to compare the structure difference of biofilms. As has been summarized in Section 1.1 that the physical structure of biofilms depends on the combined effect of various environmental conditions, such as hydrodynamic conditions, substrate loading, the type of substrate, etc. It is therefore expected that by characterizing the difference in biofilm structure, the effect of the environmental conditions can also be analyzed in a quantitative manner. For example, Srinandan et al. (2012) compared the difference of biofilm structure with respect to biovolume, $\overline{L}_f$, average diffusion distance, etc. to study

the impact of different carbon sources on the formation of biofilms. Wagner et al. (2010b) evaluated the difference in $\overline{L}_f$ and volumetric porosity (Φ) for biofilm cultivated at laminar, transient and turbulent flow to examine the effect of hydrodynamics on biofilm structure. In the work of Heydorn et al. (2000) biofilm structures were quantified with respect to the parameter set incorporated in the software COMSTAT, which revealed different structure of biofilms formed by four different *Peusdomonas* strains. Further analysis of biofilms of *P. aureofaciens* revealed the difference in L_f with different concentration of the cultivation media. The incorporation of the structural parameters, α, R_a', biofilm solids hold up, fractal dimension and biofilm compactness, into biofilm models by Picioreanu et al. (1998) and Picioreanu et al. (2000) improved the mechanistic understanding of the influence of biofilm structure on the mass transport phenomena.

Dozens of parameters have been proposed by many biofilm researchers for the quantification of biofilm structure. Based on the types of images used as input for image analysis, the parameters can be generally classified as textural parameters and areal ($2D$) or volumetric ($3D$) parameters.

According to Beyenal et al. (2004), textural information can be extracted from the variation of gray level based on gray scale images to characterize micro-scale heterogeneity with respect to density and thickness variation in biofilms. Therefore gray scale images are required as input, with no binarization required. Although dozens of textural descriptors have been proposed by Haralick et al. (1973) and used by the group of Milferstedt, only few of them are often used for image analysis in biofilm research. Milferstedt et al. (2008) argued that information loss is inevitable for low magnification and low resolution images when the images are binarized. However, except the group of Milferstedt, there has been no other group using this method for biofilm image analysis. This is probably due to the high complexity of the method itself and the fact that it is less intuitive to correlate the textural parameters to biofilm processes or the environmental conditions in which the biofilms are cultivated (Renslow et al., 2011).

To calculate areal ($2D$) and volumetric ($3D$) parameters, the gray scale images have to be segmented first. The resulted binary images are used for the further quantification of biofilm structure features. A large set of structural parameters have been used in various studies, such as areal porosity, surface coverage, average run length, average diffusion distance, mean biofilm thickness, roughness, roughness coefficient, fractal dimension, surface enlargement factor, perimeter, biovolume, surface to volume ratio, porosity, etc. Solids hold up and biofilm compactness were proposed by Picioreanu et al. (1998) to quantify the biofilm structure resulting from biofilm models. Yang et al. (2000) stated that some features could predict biofilm behavior better than the others. Although a handful of structural parameters have been used by different authors, some of them are more popular than the others, such as areal porosity, mean biofilm thickness, roughness coefficient. Resat et al. (2014) pointed out that there is still a lack of scientific basis for the selection of structural parameters. Probably because they can provide more intuitive correlation between the structural feature and

biofilm processes (Renslow et al., 2011). Table 1.3 lists several commonly used parameters from literature.

Table 1.3: List of areal and volumetric biofilm structure parameters

Parameter		Dim.	Equation	Explanation	Reference
Mean biofilm thickness	$\overline{L}_f$	2D & 3D	$\frac{1}{N}\sum L_{fi}$	a measure of the spatial size of biofilms; most common variable	Manz et al. (2003); Shen et al. (2015); Derlon et al. (2012, 2013); Heydorn et al. (2000); Srinandan et al. (2012); Zielinski et al. (2012)
Roughness	R_a	2D & 3D	$\frac{1}{N}\sum(\lvert L_{fi} - \overline{L}_f\rvert)$	absolute variance of biofilm thickness measured, N is the number of thickness measurement, L_{fi} is the ith individual thickness measurement	Murga et al. (1995); Milferstedt et al. (2006); Derlon et al. (2012, 2013); Janjaroen et al. (2013); Shen et al. (2015); Wu et al. (2012)
Roughness coefficient	R_a'	2D & 3D	$\frac{1}{N}\sum(\frac{\lvert L_{fi}-\overline{L}_f\rvert}{\overline{L}_f})$	dimensionless form of R_a which facilitate comparison of biofilm structure cultivated under different conditions	Murga et al. (1995); Derlon et al. (2012, 2013); Janjaroen et al. (2013); Shen et al. (2015); Wu et al. (2012); Picioreanu et al. (1998, 2000); Manz et al. (2003)
Surface enlargement factor	α	2D & 3D		measures the increase of real surface by the heterogeneous surface structure compared to the bare substratum	Shen et al. (2015); Picioreanu et al. (1998); Manz et al. (2003)
Perimeter	P_Γ	2D		the total number of pixels at cell cluster boundary	Beyenal et al. (2004); Renslow et al. (2011)
Biovolume	V_b	3D		the volume of total amount of biomass with a dimension of μm^3	Bridier et al. (2011); Chávez de Paz, Luis E et al. (2012); Habimana et al. (2010)

1.5   Biofilm modeling

Mathematical modeling has been proven to be a powerful tool for the study of biofilm processes. The models that have been developed span a range of complexity, from simple empirical correlations to computationally intensive algorithms simulating $3D$ biofilm structure. The challenge in biofilm modeling lies in combining the knowledge of microbiology, fluid mechanics, biochemistry, rheology as well as quorum sensing. This section provides a brief overview of the development in biofilm modeling and their successful application in improving the understanding of biofilm processes. Extensive review of biofilm modeling has been conducted by Wanner (2006), Wang and Zhang (2010)and Horn and Lackner (2014). For engineering practices one-dimensional ($1D$) biofilm models provide sufficiently accurate prediction for soluble substrate flux (Boltz et al., 2010). The uncertainty in results comes mainly from the uncertainty in the description of reactor hydrodynamics and biofilm dynamics (Boltz and Daigger, 2010). However, reactor scale simulations related primarily to engineering practices are not the focus of this thesis. Instead the focus was given to the incorporation of biofilm images as structural template into biofilm models. Based on the dimensionality and incorporation of the physical processes, the models are classified into different groups: $1D$ continuum models, multidimensional discrete-continuum models and fluid-structure interaction models.

1.5.1 $1D$ models

Steady state biofilm growth were mostly assumed in the early biofilm models, including substrate concentration and biofilm thickness. The mostly used $1D$ model is the multi-substrates, multi-species, continuum model developed by Wanner and Gujer (1986). The model is based on the principle of mass conservation and assumes a continuum approach to describe the biomass and change of properties only in the direction perpendicular to the substratum. The model allows to predict development in biofilm thickness, the distribution of microbial species and substrate distribution. Equations describing the growth of biofilms can be referred to Wanner and Gujer (1986). Reactor hydrodynamics is not explicitly described, but can be incorporated by including an external mass transfer limitation. The key feature with respect to the displacement velocity of a cell at a location equals to the newly generated biomass of all microbial species in the distance from the substratum to the location. The change of biofilm thickness in time is described using a moving boundary. Biomass detachment due to shear stress and sloughing is possible within the model. The extended model allows to incorporate simultaneous detachment and attachment of cells at biofilm surface in a more flexible way (Wanner and Reichert, 1996). The extended model also includes a more flexible description of the transport of dissolved components, the diffusive transport of particulate components in biofilm matrix and changes of the liquid phase volume fraction (porosity)

of the biofilms.

All these features are incorporated into a computer program, AQUASIM, which has been widely used in biofilm research to incorporate active and/or inactive particulate biological and/or inorganic components (Horn et al., 2003; Horn and Morgenroth, 2006; Wichern et al., 2008). However, due to its property of covering one dimension, it inherently has certain limitations. The assumption of having all the changes only perpendicular to the substratum renders the model not applicable for the cases when the strong spatial gradients in the direction parallel to the substratum cannot be overlooked (Wanner, 2006). Another limitation lies in the exclusion of the description of the bulk-liquid hydrodynamics. Even though the hydrodynamic effects can be incorporated, an accurate estimation of the concentration boundary layer thickness (L_C) has to be provided as input into the model, which introduces uncertainty into the results (Boltz et al., 2010).

1.5.2 Multi-dimensional models

With the development of imaging techniques, especially the introduction of CLSM into biofilm research, biofilms were shown to exhibit heterogeneous structure. Despite the wide applications of $1D$ models, they are, however, not able to incorporate the heterogeneous biofilm structure, which has been proven to have significant effect on local mass transfer (Picioreanu et al., 2000). To overcome these drawbacks, multi-dimensional biofilm models, both discrete and continnum models, have been in development to provide a more accurate description of biofilm activity and biofilm structure (Picioreanu et al., 1998; Kreft et al., 2001; Klapper and Dockery, 2002). The multidimensional models allow the relaxation of some assumptions commonly used in $1D$ models, such as division of biomass in layers, uniform biofilm thickness, using mass transfer boundary layer to simplify the hydrodynamics, etc.

The fundamental processes governing the growth of bacterial cells in the discrete models are similar to $1D$ models. The discrete models are generally referred to Cellular Automata (CA) and Individual-based models (IbM). In these models, cells can grow and biofilm can expand in more than one direction. In CA models, the simulation domain is divided into rectangular uniform grid ($2D$) or cubical elements ($3D$) (Wimpenny and Colasanti, 1997; Picioreanu et al., 1998). A set of simple rules is used to describe the displacement of the newly generated daughter cells. Depending on the environmental conditions, CA models could generate heterogeneous $2D$ or $3D$ structures resemble those visualized with CLSM (Picioreanu et al., 1998). Quantification of the generated biofilms revealed that substrate transfer limited regime resulted in 'finger-like' biofilms with channels and voids. At high substrate-transfer rate and low growth rate of biofilms, dense biofilms could be expected. The hybrid discrete-differential unified multi-component cellular automaton (UMCCA) model of Laspidou and Rittmann (2004b) could predict the spatial and temporal change

of the biofilm composite density for three biofilm components: EPS, active and inert biomass. The key feature of the model was biofilm consolidation due to the pressure induced by fluid over the biofilm. Compared to the random distribution of the newly generated biomass in Picioreanu et al. (1998), the UMCCA model moved the excess biomass along the path of least resistance, which is more efficient in the distribution process (Laspidou and Rittmann, 2004b). Yamamoto and Ueda (2013) incorporated a stochastic adhesion process that follows a probability function into the CA model. Detachment has also been simulated with biofilm models based on CA (Picioreanu et al., 2001; Chambless and Stewart, 2007; Yamamoto and Ueda, 2013; Laspidou, 2014).

The Individual-based modeling (IbM) developed by Kreft et al. (2001) treats each bacterial cell as a fundamental entity. IbM models are fully quantitative. The deterministic spreading mechanism overcomes the drawback of random shuffling of newly generated biomass of the biomass-based model (BbM) (Picioreanu et al., 1998). With respect to the overall growth of the biofilm, there is no significant difference between IbM and BbM but the shape due to the different biomass spreading mechanisms adopted (Kreft et al., 2001). Laspidou et al. (2010) compared the two approaches, UMCCA and IbM, in modeling the growth and development of biofilm structures. With the consolidation feature incorporated, CA seemed to be superior in fitting the experimental data for aged biofilms. While for young biofilms without cavities, IbM proved better due to the spreading rule that compensates the drawback of random placement in CA.

In the early application of IbM models, the hydrodynamics were not considered (Kreft and Wimpenny, 2001). In the study of Xavier et al. (2005a) the fluid flow was for the first time incorporated into the biofilm models by solving the Navier-Stokes equation. This enabled more realistic description of fluid flow to replace the estimation of L_C. The level-set method was included into the particle-based multi-species biofilm models in Xavier et al. (2005b) to investigate biomass detachment. Later Lardon et al. (2011) developed a platform iDynoMiCS for the implementation of IbM, in which improvements were incorporated, such as a pressure-driven biomass spreading or consolidation and the continuous-in-time EPS excretion.

Due to detailed description of each bacterial cell, the IbM approach posed a high demand on computational resources, especially in modeling systems with large-scale heterogeneity. The particle-based approach developed by Picioreanu et al. (2004) used a larger biomass particles (10 to $20\,\mu m$ in diameter) to replace the cell level biomass representation. The shoving or pushing rule for biomass spreading is still the same as that for IbM. The multi-dimensional model showed superior feature in predicting the distribution of intermediate products that needed to be transported from the production site to the consumption site. Meanwhile the growth of slowly growing or minority species can be better predicted compared to $1D$ models.

To overcome the stochastic placement of newly generated biomass used by CA, continuum models were developed (Eberl et al., 2001; Klapper and Dockery, 2002). The spatial spreading of biomass

is density driven in the continuum model of Eberl et al. (2001), while it is pressure driven in the model of Klapper and Dockery (2002), which is the key difference between the two models. Later, Alpkvist et al. (2006) combined the continuum approach developed by Klapper and Dockery (2002) for the description of the EPS matrix and the particle-based approach of Xavier et al. (2005a) to represent microbial particles. The model revealed that the consolidation in mature biofilms was due to the generation of a negative pressure in the lower part of the biofilm after the EPS and cells degradation. The model was capable of simulating the multi-dimensional gradients and fluxes of intermediate metabolic products.

The application of the above models has significantly improved our understanding of biofilm processes. However, most of them did not incorporate one of the key influential factors, namely the fluid flow, which has fundamental influence on the structure of natural biofilm. When experienced with shear forces, biofilms exhibit viscoelastic behavior (Böl et al., 2013). Shear induced compression and/or detachment has substantial influence on biofilm structure as well as mass transfer into biofilm matrix. The first fluid-structure interaction (FSI) model in biofilm systems was developed by Böl et al. (2009). The model incorporated the real biofilm structure from CLSM images to investigate the influence of few factors, such as Young's modulus, Reynolds number and biofilm structure, on biofilm detachment. The 2D FSI model of Taherzadeh et al. (2010) aimed to simulate the oscillatory movement of biofilm streamers observed by Stoodley et al. (1998b).

1.5.3   Conclusion

Depending on the complexity of the problems to be solved, biofilm models embracing different levels of complexity have been developed in the last decades, from simple 1D models to complex multi-dimensional models. The processes of adhesion, growth, competition for space and substrates, detachment and consolidation etc. can be incorporated. Depending on the methods used, the fluid dynamics governing the environment can be well described. These models have significantly enhanced our understanding of the underlying processes affecting biofilm development, such as the influences of different environmental conditions on biofilm structure as well as the impact of biofilm structure on the surroundings. However, there has been seldom studies that combined biofilm imaging and mathematical modeling for the investigation of biofilm related processes and properties.

1.6   Interaction between organic particles and biofilms

In municipal waste water a large part of COD is associated to the particulate organic matter with size ranging from few submicron to several hundred of microns (Levine et al., 1985; Tchobanoglous

et al., 2003). However, they can not be directly assimilated by microorganisms. The organic particles have to go through hydrolysis processes that reduce the particle size and release the hydrolytic products to be available for microorganisms (Gujer et al., 1999). Due to broad size range and the complexity of the organic particles with respect to their chemical composition (Huang et al., 2010), research conducted so far mostly used model compounds of simplified composition and well-defined characteristics for the investigation of hydrolysis mechanism. The model compounds often used include bovine serum albumin ($65000\,Da$) (Confer and Logan, 1998), soy proteins (molecular weight (M_W) up to $75kDa$) (Mosquera-Corral et al., 2003), dextran (average $M_W = 70000\,Da$) (Confer and Logan, 1998; Kommedal et al., 2006), etc. So far no study has been conducted to examine the hydrolysis process of the highly complex organic particles originating from real municipal waste water .

Boltz and La Motta (2007) suggested to separate the removal process of organic particles into four steps: transport of the particles to the biofilm surface, attachment of particles, hydrolysis of the particles and followed by the release of the hydrolytic products and biochemical reaction of the products. The latter two steps have been relatively well studied. There are only few studies touched the first two steps. The attachment of particles in biofilm systems can be further divided into two steps: the physical process of transporting the particles from bulk liquid to the liquid-biofilm interface and the chemical process of attachment of particles onto biofilm surface (Bouwer, 1987). Boltz and La Motta (2007) named the attachment process as bioflocculation and described it with a first-order kinetic expression. Nevertheless, no study has been carried out to visualize the process of attachment of organic particles onto biofilm surface. Further, a negative influence of the attachment of organic particles onto the biofilm surface on the removal of dissolved substances was reported by Särner and Marklund (1985). The authors speculated that it was due to the degradation of the organic particles caused a local oxygen shortage. However, no further experimental or modeling work has been conducted to verify the assumption.

1.7   Scope of the thesis

Based on the analysis above, the objective of this work is to quantify the meso-scale biofilm structures with OCT and to study the mass transfer characteristics at liquid-biofilm interface. The context of this work can be divided into different stages:

- First of all, a method using OCT was developed to monitor the temporal structure development of biofilms grown on carriers used in lab-scale moving bed biofilm reactors (MBBRs) as model system. Procedure for image analysis was compiled.

- The influence of biofilm structure and the mass transfer characteristics in the vicinity of biofilm surface was investigated by incorporating the real biofilm structure obtained from OCT imaging into fluid flow simulation. Thereby research with biofilm imaging and modeling can be connected.

- The imaging method developed was further employed to visualize the attachment of organic particles originating from municipal waste water onto biofilm surface. Estimation of the particles attached was conducted based on image analysis. The mechanism of the negative impact on the removal of soluble substrates after the attachment of organic particles was investigated with the method developed in this thesis.

1.8 Structure of the thesis

In Chapter 1 the background on biofilm structure is provided with respect to the factors that impact biofilm structure, comparison of the commonly used imaging techniques at different spatial scales and quantification of biofilm structure based on the images obtained. The application of and relevant research on MBBR process are briefly reviewed as the biofilms used in this study were cultivated in lab-scale MBBRs. The progress on mathematical modeling of biofilms in the last decades is summarized. Research on the hydrolysis of particulate organic matter in municipal waste water is shortly introduced. Chapter 2 presents detailed imaging procedure with OCT and the procedure on subsequent $3D$ imaging analysis. Both temporal and spatial development of biofilms on carriers used in lab-scale MBBRs are analyzed. A model combining the OCT images as biofilm structure template and mathematical description of hydrodynamics, substrate transport and biochemical reaction is illustrated in Chapter 3. Chapter 4 provides the results on the visualization of the attachment of particulate organic matter onto biofilm surface by means of OCT. The OCT image data are further incorporated into mathematical models to study the mechanism of the negative impact on the removal of soluble substrates after the attachment of particulate organic matter on biofilm surface. The results of the thesis are summarized in Chapter 5.

Chapter 2

Investigation on biofilm structure development in lab-scale MBBRs with OCT

2.1 Introduction

Biofilms are agglomerates of microorganisms embedded in a gel matrix consisting of extracellular polymeric substances produced by the microorganisms, such as polysaccharides, proteins, lipids, humic and nucleic acid (Flemming and Wingender, 2010). Depending on the environmental conditions with respect to substrate availability and hydrodynamics etc., various physical structures of biofilms have been reported (Stoodley et al., 1999; Wagner et al., 2010b). Different imaging techniques were introduced to investigate the physical structure as well as the biochemical properties, such as light microscopy (Milferstedt et al., 2013), MRI (Manz et al., 2003), the mostly used CLSM (Lawrence and Neu, 1999), Raman microscopy (Ivleva et al., 2009) and SEM (Priester et al., 2007). Microscopic images can cover large area at the macro-scale. However, its application is limited by its low resolution. Studies on biofilm structure and function at the micro-scale have been advanced through CLSM, SEM etc. However their applications are restricted by limited staining efficiency (CLSM), altering of biofilm structure due to drying (SEM), not being representative because of the small imaging area covered (CLSM, SEM).

Milferstedt et al. (2009) recommended a representative elemental area of $3.4\,mm^2$ for the quantification of gray level and correlation to characterize biofilm structure. To analyze mass transport phenomena in biofilms, a characteristic length of at least $400\,\mu m$ is required in biofilm images to provide the relevant structural information (Milferstedt et al., 2009). This is the meso-scale from sub-millimeter to centimeter defined by Morgenroth and Milferstedt (2009). According to Wagner et al. (2010b), MRI and optical coherence tomography could be the optimal candidates for biofilm imaging at the meso-scale.

As a newly developed imaging technique in medical science (Huang et al., 1991), optical coherence tomography (OCT) has recently been introduced into biofilm research (Xi et al., 2006). The capability of OCT in the visualization and quantification of biofilm structure has been demonstrated by Xi et al. (2006), Haisch and Niessner (2007) and Wagner et al. (2010b). It compensates the aforementioned limitations and enables fast, *in situ* and non-invasive $3D$ visualization of biofilm structure at the meso-scale and thus exhibits high potential in biofilm research. One advantage worth emphasizing is that no biofilm preparation is required. Thereby the structural integrity is well preserved. Derlon et al. (2012) characterized the structure of biofilms developed on the surface of gravity driven ultrafiltration system with respect to $\overline{L}_f$, R_a and R'_a by means of OCT. Janjaroen et al. (2013) investigated the mechanisms of $E.coli$ attachment onto biofilms fed with groundwater and successfully correlated the adhesion of $E.coli$ cells to the physical structural of biofilms. Compaction and de-compaction of biofilms under different permeate flux applied was observed by Dreszer et al. (2014) with OCT. Additionally, biofilm thickness calculated based on OCT images increased over time and can be correlated to pressure drop and the biofilm resistance. However, all the quantification in these studies was based only on $2D$ cross-sectional images. So far only Wagner et al. (2010b) conducted $3D$ quantification with respect to biofilm thickness and porosity for biofilm grown in a flume.

Moving bed biofilm reactors (MBBR) incorporate plastic carriers into waste water treatment process, thereby provide large protected surface area for microorganisms to attach and grow on. In comparison to the convectional activated sludge process, MBBRs offer the benefits of having small footprint, easy upgrade by varying carriers used, low maintenance and less sludge production (Ødegaard et al., 1994; Ødegaard, 2006). Most of the studies on MBBRs so far focused on optimizing its performance, such as the optimal filling degree (Gu et al., 2014), effect of carrier geometry (Levstek and Plazl, 2009) or microbial community structure (Biswas et al., 2014). There has been no study investigating the biofilm structure development on the carriers in MBBR yet. Although not intended for biofilm structure analysis, Almstrand et al. (2014) observed the funnel like structure in the compartments of the chip carrier from the composite FISH images. However, the imaging depth was limited to only $400\,\mu m$ in depth from carrier surface.

The objective of the current study is to characterize the structure of biofilms developed on the carriers from a lab-scale MBBR. For this purpose, light microscopic ($2D$) and OCT ($3D$) images were obtained. Comparison between the results derived from $2D$ and $3D$ images were conducted to investigate if complex $3D$ imaging is necessary to characterize the biofilm structure. Moreover, the study intends to provide a scheme on how to image biofilms on MBBR carriers and how to quantify their structure.

2.2 Material and methods

2.2.1 Reactor performance

Experiments were conducted in two lab-scale MBBRs. The custom-made cylindrical Plexiglas®
reactors have an effective volume of $2.2\,L$. Each reactor was filled with two different types of carrier
(AnoxKaldnes$^{\text{TM}}$), named Carrier A and Carrier B, shown in Figure 2.1. The characteristics of the
carriers are provided in Table 2.1. Each reactor contained 190 carriers, 95 carriers of each type,
resulting in a filling ratio of 13.6% and a total surface area of $0.213\,m^2$ ($97\,m^2 \cdot m^{-3}$).
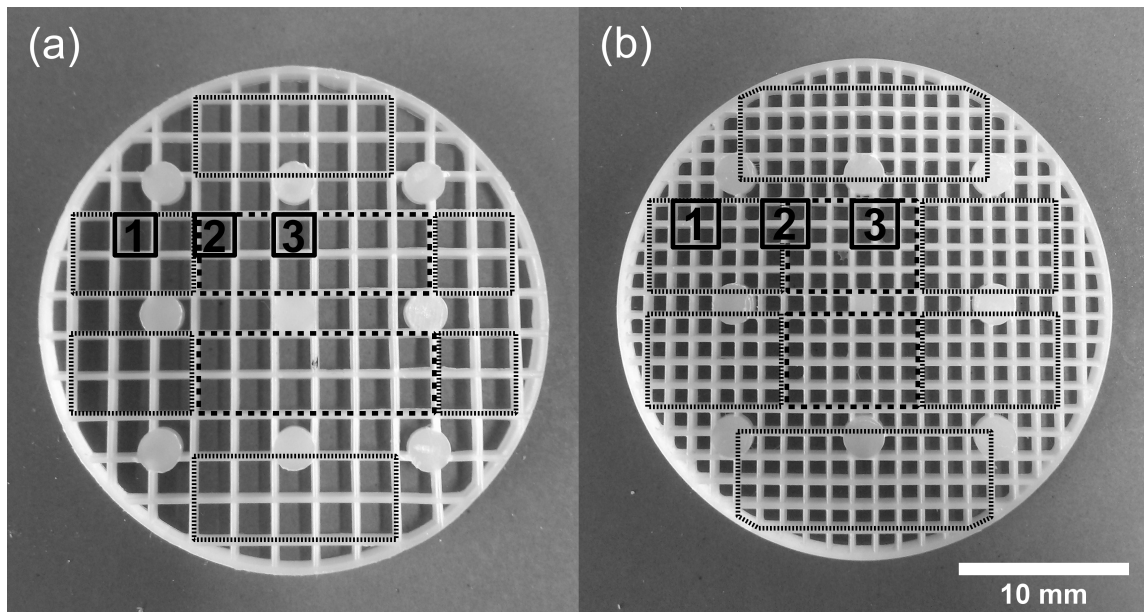
Figure 2.1: Areas covered by light microscopy and OCT imaging on (a) Carrier A and (b) Carrier
B. Border regions are framed with densely dotted lines . Center regions are framed with sparse
dotted lines. Compartments numbered with 1, 2, 3 mark the OCT imaging positions. Diameter
of both carriers is $30\,mm$. The compartment size of Carrier A and B are $2.4 \times 2.4 \times 1.05\,mm^3$ and
$1.4 \times 1.4 \times 1.05\,mm^3$, respectively.

Table 2.1: The characteristics of the carrier material

Carrier	Carrier thickness	Diameter	Compartments per Carrier	Protected surface area
	(mm)	*(mm)*	*(−)*	*(cm²)*
A	1.05	30	103	8.84
B	1.05	30	300	13.63

Medium was pumped continuously from two influent tanks, one containing substrate, the other the
macro nutrients. The pH value was maintained between 6.5 and 7.5 through a Wago SPS unit using
a $0.1\,mol \cdot L^{-1}$ $KHCO_3$ solution. The flowrate of the influent was verified by daily measurement

of the effluent. Compressed air was regulated by two air flow meters (Krohne DK $800/N$) and supplied at the bottom of the reactor through perforated pipes installed on one side only.

Each reactor was inoculated for 24 hours with $2L$ of activated sludge (TSS $3.5\,g \cdot L^{-1}$) from sewage plant in Neureut, Karlsruhe. Continuous operation started after discarding the activated sludge and washing the carriers. Reactors were operated at room temperature (20 ± 1^oC) with a hydraulic retention time (HRT) of $4.4\,h$ and were cleaned once a week. The experiments were performed twice at different aeration rates, with a high aeration rate of $250\,L \cdot h^{-1}$ (H) and a low aeration rate of $150\,L \cdot h^{-1}$ (L). Temperature and pH values were measured on-line (Wago SPS Unit in combination with Endress+Hauser Liquiline M CM42). Dissolved oxygen (DO) was measured daily with a DO meter (WTW Multi 350i). The experiment was terminated when all carriers were completely covered with biomass.

Cultivation medium was prepared twice a week according to Wagner et al. (2010b). It consisted of $100 - 300\,mg \cdot L^{-1}$ D-(+)-Glucose H_2O, nutrients (in $mg \cdot L^{-1}$): $(NH_4)_2SO_4$ ($20 - 40$), $CaCl_2 \cdot 2H_2O$ ($5.6 - 11.2$), $MgSO_4 \cdot 7H_2O$ ($14 - 28$), $FeSO_4 \cdot 7H_2O$ ($10 - 20$), $NaNO_3$ ($12 - 24$), KH_2PO_4 ($2.25 - 4.5$), trace elements in (µ$g \cdot L^{-1}$): H_3BO_3 ($300 - 600$), $CoSO_4 \cdot 7H_2O$ ($130 - 260$), $CuCl_2$ ($8 - 16$), $MnSO_4 \cdot H_2O$ ($20 - 40$), $Na_2MoO_4 \cdot 2H_2O$ ($26 - 52$), $NiCl_2 \cdot 6H_2O$ ($10 - 20$), $ZnSO_4 \cdot 7H_2O$ ($2 - 4$). The concentrations were increased twice by 100% and 50% of the initial concentrations for COD and mineral medium, respectively. Concentrations of COD and nitrogen species ($NH_4^+ - N$, $NO_2^- - N$, $NO_3^- - N$) in the reactor medium were measured with Hach-Lange Test Kit three times a week and once a week ($NH_4^+ - N$, $NO_2^- - N$, $NO_3^- - N$), respectively.

2.2.2   Image acquisition

Images were acquired three times a week by means of light microscopy ($2D$) and OCT ($3D$) from one carrier of each type and reactor. Inspection of three chips with light microscope showed no significant visual difference in biomass distribution. During image acquisition the carrier was immersed in filtered bulk liquid. As both light microscopy and OCT are non-invasive to biofilms, the carrier imaged was returned to the reactor after taking images. So the filling ratio of the carriers kept constant throughout the experiment.

Imaging with light microscopy ($2D$)

$2D$ images were taken using light microscopy SMT4 (Mikroskop Technik Rathenow) in combination with a DSLR camera (Canon EOS 600D). Camera setting was fixed at: 18 megapixel resolution, exposure time $1/10\,s$, ISO 100 and manual whitening balance. Magnification of the microscope was set at $16\times$, resulting in an image dimension of $8.5 \times 5.7\,mm^2$ with a resolution of $611\,pixels \cdot mm^{-1}$.

To simplify image processing, only the full compartments framed in Figure 2.1 were considered, neglecting the irregular compartments. The carriers were divided into border and center regions. Thereby 60% for Carrier A (62 compartments included) and 70% for Carrier B (210 compartments included) were imaged and quantified, respectively.

Imaging with OCT ($3D$)

$3D$ images were acquired using a Thorlabs Ganymede with a central wavelength of $930\,nm$ and ThorImage 4.2 (Thorlabs GmbH, Dachau, Germany). The volume captured was $3.20 \times 3.20 \times 1.47\,mm^3$ ($450 \times 450 \times 700\,pixel^3$) for Carrier A and $3.30 \times 3.30 \times 1.47\,mm^3$ ($450 \times 450 \times 700\,pixel^3$) for Carrier B. For Carrier A, each image covered one compartment. For Carrier B, each image covered 4 compartments. The refractive index was set to 1.33, which equals to the refractive index of water, since biofilm consists of around 90% of water (Bakke et al., 2001; Melo, 2005). Three locations, marked in Figure 2.1, from border to center of the carrier were imaged to investigate the spatial distribution of biofilm on a single carrier. Images at the same position from both top and bottom side of the carriers were taken to cover the whole depth of biofilm growing on the carriers.

2.2.3   Image analysis

Image analysis was carried out in Fiji (ImageJ 1.49g) (Schindelin et al., 2012) to extract structural information from the biofilm images. In the current study, only volumetric parameters were considered. Textural parameters based on pixel/voxel intensity variation were not taken into account.

$2D$ light microscopic images

$2D$ images were first converted to $8-bit$ gray scale images. Illumination correction method developed by Landini was applied to eliminate uneven illumination artifacts. Contrast enhancement was implemented prior to automatic thresholding. Finally the resulting binarized images have intensity values of 1 for biofilm and 0 for the void area in the center of the compartment. Measurement of the void area was performed by Fiji's 'analyze particles' plugin. Quantification of the biofilm structure based on $2D$ images is illustrated in Figure 2.2, with respect to average biofilm thickness ($\overline{L}_{f,2D}$) (Murga et al., 1995), compartment coverage (η_{2D}) and surface enlargement (SE_{2D}) (Picioreanu et al., 1998). The detailed calculations are provided as following:

- Average biofilm thickness ($\overline{L}_{f,2D}$): calculated by converting the void area A_V into an equivalent square of same area. The distance between the border of the compartment and the border of the empty square gives $\overline{L}_{f,2D}$:

$$\overline{L}_{f,2D} = \frac{a_0 - \sqrt{A_V}}{2} \quad [mm] \tag{2.2.1}$$
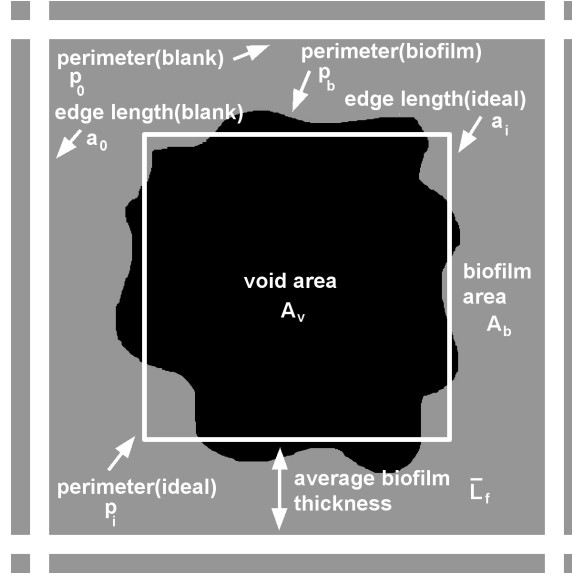
Figure 2.2: Schematic of the calculation of $2D$ parameters based on light microscopic images. The white thick lines define the boundary of one compartment. Biofilm is presented in gray. The void area in a compartment is presented in black.

- Biofilm growth rate ($u_{f,2D}$): the time derivative of $\overline{L}_{f,2D}$. A positive value indicates growth of biofilm, while a negative value implies detachment of biofilm. i denotes the day involved in the calculation.

$$u_{f,2D} = \frac{\overline{L}_{f,2D}(i+1) - \overline{L}_{f,2D}(i)}{day(i+1) - day(i)} \quad [mm \cdot d^{-1}] \tag{2.2.2}$$

- Compartment coverage (η_{2D}): percentage of biofilm area to the total area of one compartment (A_{toto}). This value represents the coverage of a carrier by biofilm.

$$\eta_{2D} = \frac{A_b}{a_0 \times a_0} \times 100 \quad [\%] \tag{2.2.3}$$

- Surface enlargement (SE_{2D}) (Picioreanu et al., 1998): ratio of the length of biofilm front (p_b) to the substratum length (p_0). It also indirectly measures the heterogeneity of biofilm surface.

$$SE_{2D} = \frac{p_b}{p_0} \quad [-] \tag{2.2.4}$$

$3D$ OCT images

Figure 2.3 presents the procedure for $3D$ image analysis. To facilitate the comparison, the images were firstly cut to the same size, one and four compartment(s) for Carrier A and B, respectively. The images were converted to $8-bit$ gray scale images. Brightness and contrast was adjusted manually

to achieve the best signal-to-noise ratio. During image acquisition, the carriers were slightly bent, which resulted in tilted images. To facilitate the following processing, the images were subjected to a tiltness correction. Then the beams of the carriers were outlined and removed. 'Gaussian Blur 3D' and automatic thresholding were applied to separate biomass from the background. The whole depth of the biofilms was achieved by concatenating the image stacks from top and bottom view, with each part contributing 60% and 40% to the whole carrier depth, respectively. Isolated noise was removed by the 'find connected regions' plugin. Subsequently the biofilm surface was measured with 'BoneJ Isosurface' plugin (Doube et al., 2010). In the end, all white pixels in the whole stack were summed to represent the amount of biomass available.
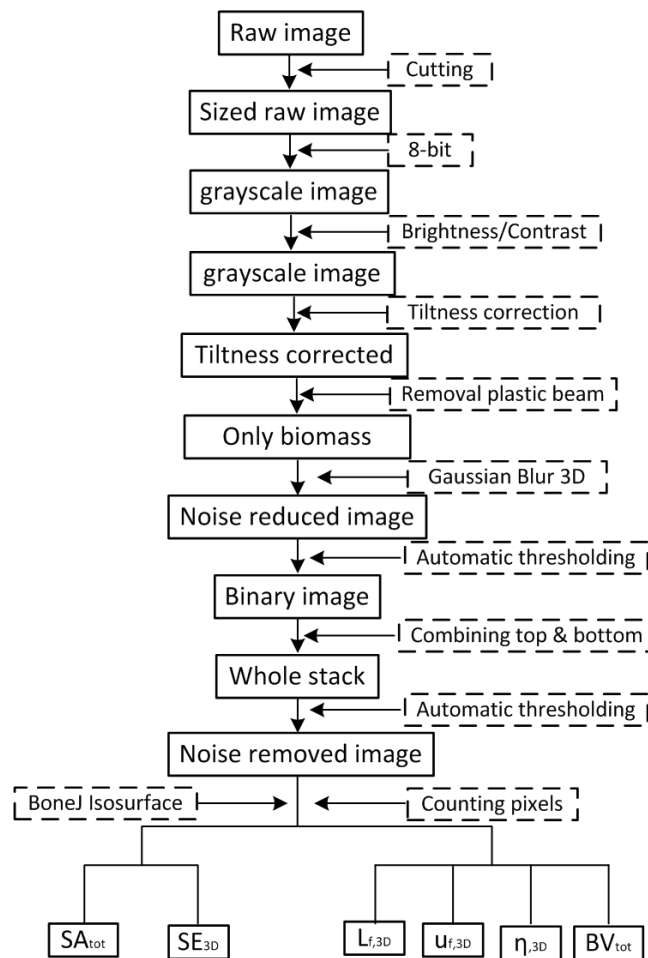
Figure 2.3: The procedure for 3D image processing. Closed frames are the images for the next step. Dotted frames are the image processing steps.

Quantification of biofilm structure based on 3D datasets was conducted with respect to the following parameters:

- Average biofilm thickness ($\bar{L}_{f,3D}$)) (Heydorn et al., 2000; Murga et al., 1995): The 3D dataset was firstly resliced to obtain top view images (xy cross-section). The average biofilm

thickness was calculated for each slice (495 slices in total) with the same formula used to calculate $\overline{L}_{f,2D}$. The values were averaged again over the number of slices, resulting in $\overline{L}_{f,3D}$.

- Biofilm growth rate ($u_{f,3D}$): similar to the calculation of $u_{f,2D}$

$$u_{f,3D} = \frac{\overline{L}_{f,3D}(i+1) - \overline{L}_{f,3D}(i)}{day(i+1) - day(i)} \quad [mm \cdot d^{-1}] \tag{2.2.5}$$

- Compartment filling degree (η_{3D}): calculated as the ratio between voxels of biomass and the total number of voxels of a blank compartment.

$$\eta_{3D} = \frac{total\, number\, of\, biomass\, voxels\, (sample)}{total\, number\, of\, voxels\, (blank)} \times 100 \tag{2.2.6}$$

- biomass volume (BV_{tot}) (Heydorn et al., 2000): reflects the total amount of biomass on the whole carrier. It is calculated differently for Carrier A and B due to the different size of the compartments as well as the total coverage of the carriers.

$$BV_{3D} = \eta_{3D} \times volume\, of\, one\, compartment \quad [mm^3] \tag{2.2.7}$$

$$BV_{A,tot} = BV_{3D,A} \times 62 \times \frac{100}{60} \quad [mm^3] \tag{2.2.8}$$

$$BV_{B,tot} = BV_{3D,B} \times 210 \times \frac{100}{70} \quad [mm^3] \tag{2.2.9}$$

- Surface area (SA_{tot}): the area of liquid-biofilm interface. It was measured by BoneJ Isosurface plugin. As BoneJ measures the area of all the surfaces exposed, the surface area of the inner walls of the compartment has to be subtracted. An increase of SA_{3D} indicates a more heterogeneous biofilm growth.

$$SA_{3D} = SA_{3D}(sample) - SA_{3D}(blank) \quad [cm^2] \tag{2.2.10}$$

$$SA_{A,tot} = SA_{3D,A} \times 62 \times \frac{100}{60} \quad [cm^2] \tag{2.2.11}$$

$$SA_{B,tot} = SA_{3D,B} \times 210 \times \frac{100}{70} \quad [cm^2] \tag{2.2.12}$$

- Surface enlargement (SE_{3D}): Similar to SE_{2D}, it was calculated by dividing biofilm surface area to the area of the substratum.

$$SE_{3D} = \frac{SA_{3D}(sample)}{SA_{3D}(blank)} \quad [-] \tag{2.2.13}$$

2.3 Results and discussion

2.3.1 Reactor operation

During the reactor operation with high and low aeration rate, the operation parameters were in the expected range (Table 2.2). Reactor performance was evaluated with respect to COD turnover ($g \cdot d^{-1}$), provided in Figure A.1. Influent COD was increased for both aeration rates from 100 to 300 $mg \cdot L^{-1}$. At low aeration rate, COD turnover increased more rapidly than at high aeration rate. The maximum turnover for both aeration rates was $1.42\, g \cdot d^{-1}$. Nevertheless, the MBBRs were simply used for the cultivation of biofilms on the carriers. We focus on imaging and biofilm structure analysis.

Table 2.2: Reactor operation parameters

Experiment	Duration	pH	T	DO	HRT	Max. COD removal
	(d)	$(-)$	(^oC)	$(mg \cdot L^{-1})$	(h)	$(g \cdot d^{-1})$
High	39	6.9 ± 0.2	21.2 ± 0.6	7.1 ± 0.3	4.1 ± 0.4	1.42
Low	25	6.9 ± 0.3	21.7 ± 0.5	7.6 ± 0.3	4.4 ± 0.2	1.42

2.3.2 Spatial and temporal development of biofilm structure

Examples of 2D and 3D images are provided in Figure 2.4. Results obtained from image analysis for Carrier A at low aeration rate were presented as an example to demonstrate the applicability of the method for biofilm structure analysis.

Figure 2.4(a) shows biofilm growing as expected from carrier walls towards the center, with more biomass in the corners. The cross-sectional image shown in Figure 2.4(b) revealed that there was more biomass at the vertical center of the carrier and less biomass at the tips of the plastic beams. Such a distribution pattern can be better visualized by the 3D rendered image presented in Figure 2.4(c). Limited amount of biomass was present close to the tip of the beams. Following the carrier compartment depth (z direction), the amount of biomass progressively increased and grew into the center of the compartment. Similar funnel-like biofilm structure was also observed by Almstrand et al. (2014) with cryosectioning and assembled FISH images on the mini-chips used for Anammox bacteria in MBBR. However, the biofilm structure was obtained only for the first 400 μm out of the 2 mm depth of the whole carrier (Almstrand et al., 2014). In this study, OCT enabled us to investigate the 3D biofilm structure non-invasively over the whole depth of carriers. Such pattern of biomass distribution inside the compartments of the carriers is presumably controlled by collision of the carriers against each other as well as detachment induced by shear forces at carrier surface.
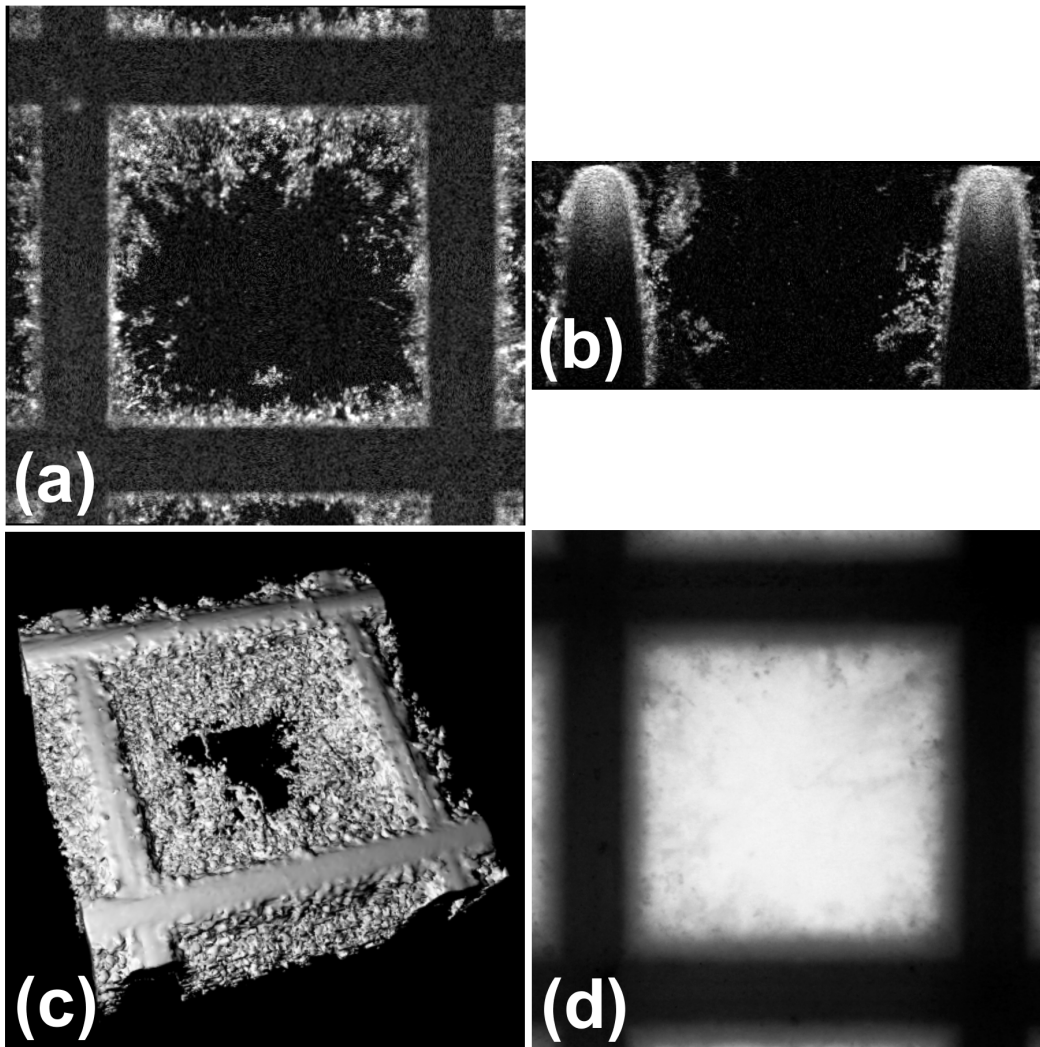
Figure 2.4: Examples of biofilm structure developed on carrier A after 7 days visualized with OCT (a-c) and light microscopy (d) of one compartment. (a) top view achieved by reslicing OCT B-Scan stack, (b) cross-sectional view achieved with B-Scan, (c) $3D$ biofilm representation achieved with BoneJ Isosurface rendering of C-Scan, (d) top view by light microscopy. Image dimensions: (a) $3.2 \times 3.2\,mm^2$, (b) $3.2 \times 1.05\,mm^2$, (b) (c) $3.2 \times 3.2 \times 1.1\,mm^3$, (d) $3.2 \times 3.2\,mm^2$.

Quantification of the structure based on $3D$ images is presented in Figure 2.5. The results are the average values over the three image locations marked in Figure 2.1 to consider the carrier as a whole to investigate the temporal development of biofilm structure. The average biofilm thickness ($\overline{L}_{f,3D}$) presented in Figure 2.5(a) advanced gradually and reached its maximum of $0.57\,mm$ on day 23. $u_{f,3D}$ increased from day 4 to its maximum of $0.085\,mm \cdot d^{-1}$ on day 9. Afterwards $u_{f,3D}$ fluctuated, reaching also negative values on day 16 and 25, which implies detachment of biomass. By definition for the calculation of η_{3D} and BV_{3D} by counting the biomass pixels available, similar to that for $\overline{L}_{f,3D}$, the two values displayed in Figure 2.5(b) show same trend as $\overline{L}_{f,3D}$. Both parameters reached their maximum values of 82% and $342\,mm^3$ on day23.
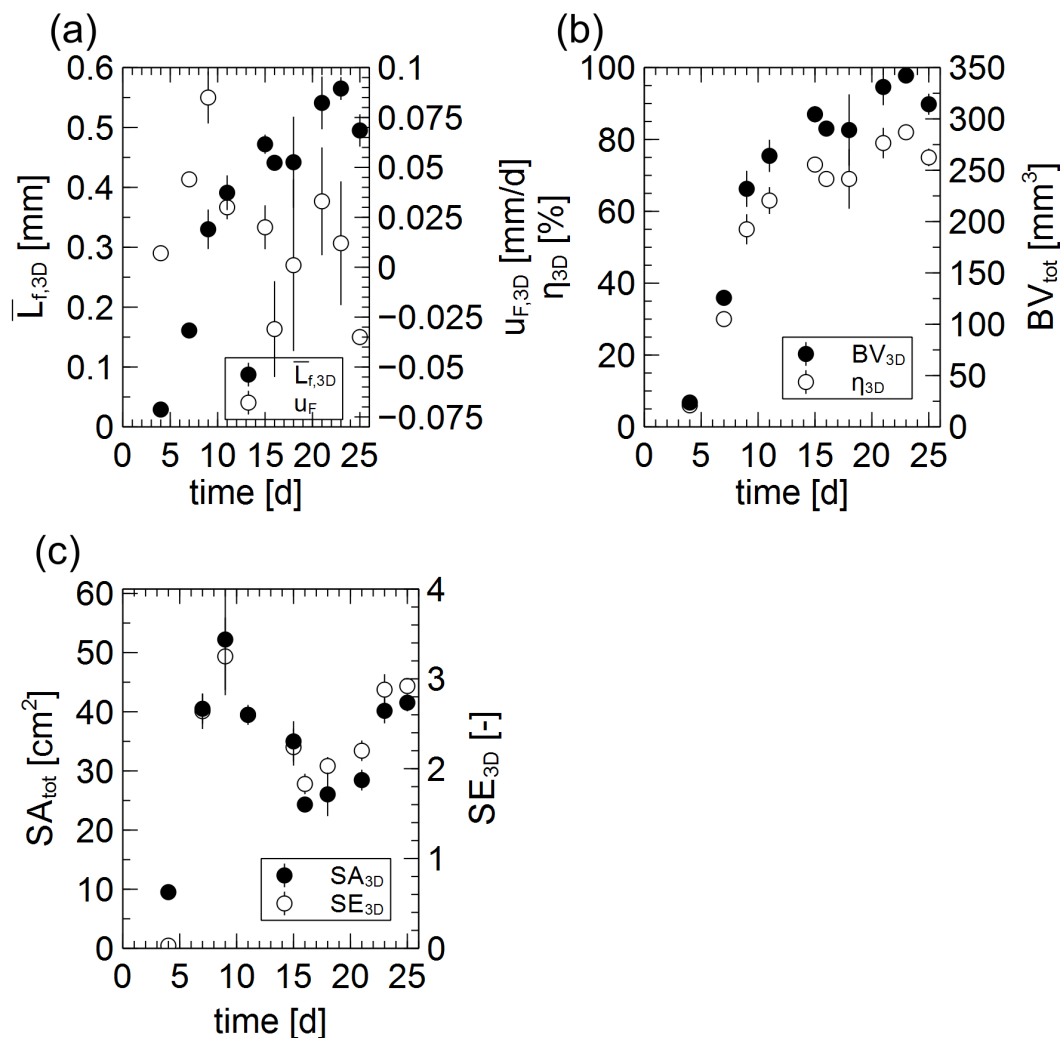
Figure 2.5: Temporal development of biofilm structure on Carrier A at low aeration rate based on 3D image analysis for (a) average biofilm thickness ($\overline{L}_{f,3D}$) and growth rate ($\mathbf{u}_{f,3D}$), (b) compartment filling degree (η_{3D}) and biomass volume (BV_{3D}), (c) surface area (SA_{3D}) and surface enlargement (SE_{3D}).

Figure 2.5(c) displayed the development of biofilm surface area (SA_{3D}) and surface enlargement

(SE_{3D}), which is different from the evolution of $\overline{L}_{f,3D}$, η_{3D} and BV_{3D}. The growth of heterogeneous biofilms at the early phase increased SA_{3D}. However, after the biofilm had merged in the center after day 9, further growth of biofilms led to the decrease of SA_{3D}. Contrary to an expected continuing decrease, SA_{3D} increased towards the end. SE_{3D} is based on the measurement of SA_{3D} and therefore shows the same trend, also reaching its maximum on day 9. Except erosion and detachment that led to loss of biomass, a sudden decrease in $\overline{L}_{f,3D}$, BV_{3D} and η_{3D} from day 23 to day 25 can partly be attributed to the limitation in penetration depth of OCT.

Similar limitation has also been observed in the application of OCT for biofilm related research reported by Derlon et al. (2012, 2013) and Dreszer et al. (2014). Light is attenuated due to the strong reflection at the air-water interface and scattering in biofilms because of the difference in refractive index between biomaterial and water (Zhu et al., 2013). Therefore, no information could be gathered at deeper biofilm layer. Different from the treatment in Dreszer et al. (2014) to fill the false voids, the voids were not artificially filled in the current study, which directly led to the underestimation of the parameters calculated based on voxel counting, such as $\overline{L}_{f,3D}$, BV_{3D} and η_{3D}. On the contrary, the 'ISO surface' plugin of BoneJ sums up all the surface area available without distinguishing between the external and internal surface. The presence of such false voids enlarges the total surface area, thereby leading to an overestimation of the bulk-biofilm interface. To overcome such limitations, it might be helpful to use OCT with longer wavelength (Kodach et al., 2010) and/or a stronger power source, to treat biofilms using optical clearing agents (Larina et al., 2008) or work with water immersion lenses that can be used under the water surface.

2.3.3   Comparison of biofilm structure on Carrier A and B

Various types of carriers are available on the market for MBBR processes. The study of Levstek and Plazl (2009) with two carriers of fundamentally different geometries failed to conclude the influence of carrier geometry on carrier performance. So far it is still not clear how the carrier geometry affects biofilm growth. In this study the influence of carrier geometry on biofilm structure development was investigated with respect to $\overline{L}_{f,3D}$, BV_{3D} and η_{3D} and SA_{tot}. To avoid overloading of data, here only the results at low aeration rate are presented, see Figure 2.6. The indices A and B refers to Carrier A and B, respectively. Due to the difference in compartment size and substratum area, a direct comparison of BV_{3D} and SA_{3D} between A and B would not lead to any meaningful conclusion. Instead BV_{3D} and SA_{3D} were converted to values for the entire carrier and then compared, as the two carriers have the same dimension.

Referring to Figure 2.6, it is clear that till day 11, Carrier B revealed higher values for $\overline{L}_{f,3D}$, η_{3D}, and BV_{tot} than Carrier A. This suggests that Carrier B promoted quicker initial establishment of biofilm. Compared to Carrier A with a compartment size of $2.4 \times 2.4 \times 1.05\,mm^3$ and a protected
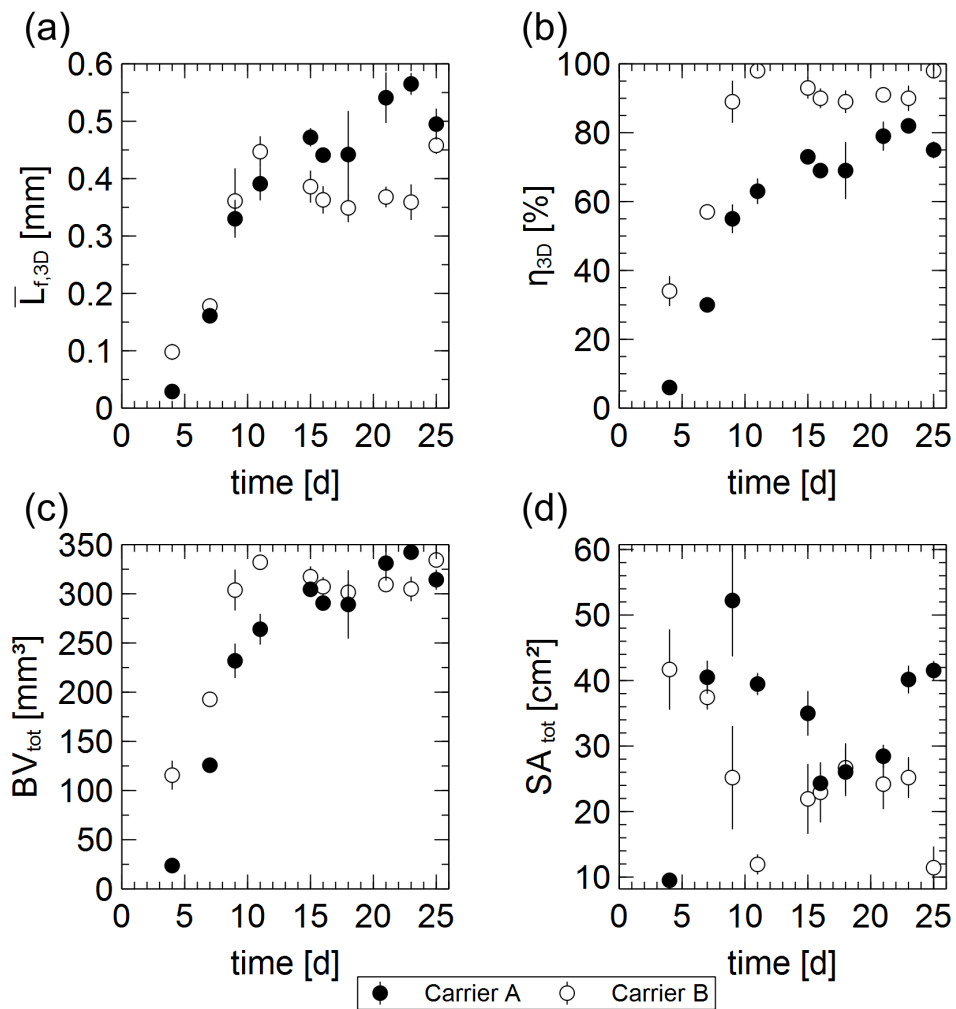
Figure 2.6: The influence of carrier geometry on biofilm structure development. Parameters shown for Carrier A and B include (a) average biofilm thickness ($\bar{L}_{f,3D}$), (b) compartment filling degree (η_{3D}), (c) total biomass volume (BV_{tot}) and (d) total surface area (SA_{tot}).

surface area of $8.84\,cm^2/carrier$, the smaller compartment size ($1.4 \times 1.4 \times 1.05\,mm^3$) of Carrier B provides more protected surface area ($13.63\,cm^2/carrier$) for biofilm to grow on. After the compartments were fully filled with biomass on day 11 for Carrier B, $\overline{L}_{f,3D}$, η_{3D}, and BV_{tot} kept relatively constant. Since the compartments of Carrier A are larger, the biofilm on Carrier A grew further, with $\overline{L}_{f,3D}$ and BV_{tot} exceeding the corresponding values of Carrier B. Nevertheless $\eta_{3D,B}$ was always higher than $\eta_{3D,A}$ (see Figure 2.6(b)), indicating that the compartments of Carrier A were not fully filled by biofilm till the end of the reactor operation. At the end of the operation, Carrier A resulted in higher values for BV_{3D} than Carrier B. Smaller compartment size of Carrier B indeed promoted quick initial growth. However, Carrier A with lower protected surface area but bigger compartment size leaves more space on the carrier for biofilm to grow. Therefore, more biomass can accumulate on Carrier A. Shown in Figure 2.6(d), biofilm surface area $SA_{tot,B}$ of Carrier B showed its maximum on day 4 and was significantly higher than $SA_{tot,A}$. Afterwards, $SA_{tot,B}$ decreased continuously until day 11 and approached a relatively stable value of around $25\,cm^2$ between days 15 to 23. $SA_{tot,A}$ increased sharply from day 4 onwards and exceeded $SA_{tot,B}$ on day 7. Decrease in SA_{tot} was also valid for Carrier A.

Boltz and Daigger (2010) pointed out that excessive growth of biofilm would lead to reduction of biofilm surface area, which is true for the inward growth of biofilm in the carriers used here. Compared to Carrier A with lower protected surface area, Carrier B with a high protected surface area actually reached a lower biofilm surface area (SA_{tot}) after the carriers are fully filled with biomass.

2.3.4 The influence of the aeration rate on biofilm structure

Agitation of the carriers in our study was achieved through aeration. By varying the aeration intensity, the movement of the carriers varied, resulting in changes of hydrodynamics in the reactor. Therefore, evolution of different biofilm structures was expected. During the experiment with a high aeration rate, OCT images were acquired only from one side of the carrier. Therefore, all the comparison in this section is based on results derived from 60% of the carrier height for both types of carriers. The comparison with respect to η_{3D}, SA_{3D} and $\overline{L}_{f,3D}$ are presented in Figure 2.7. The compartment filling degree η_{3D} at a low aeration rate was slightly higher than that at a high aeration rate for both types of carrier (Figure 2.7(a) and (b)). Larger difference can be observed for biofilms at an early phase before day 11 between low and high aeration rates. For young biofilms (younger than 11 days) on both carriers, low aeration rates resulted in fast biomass accumulation. The difference narrowed down with biofilm growth and became insignificant when η_{3D} reached relatively stable levels.

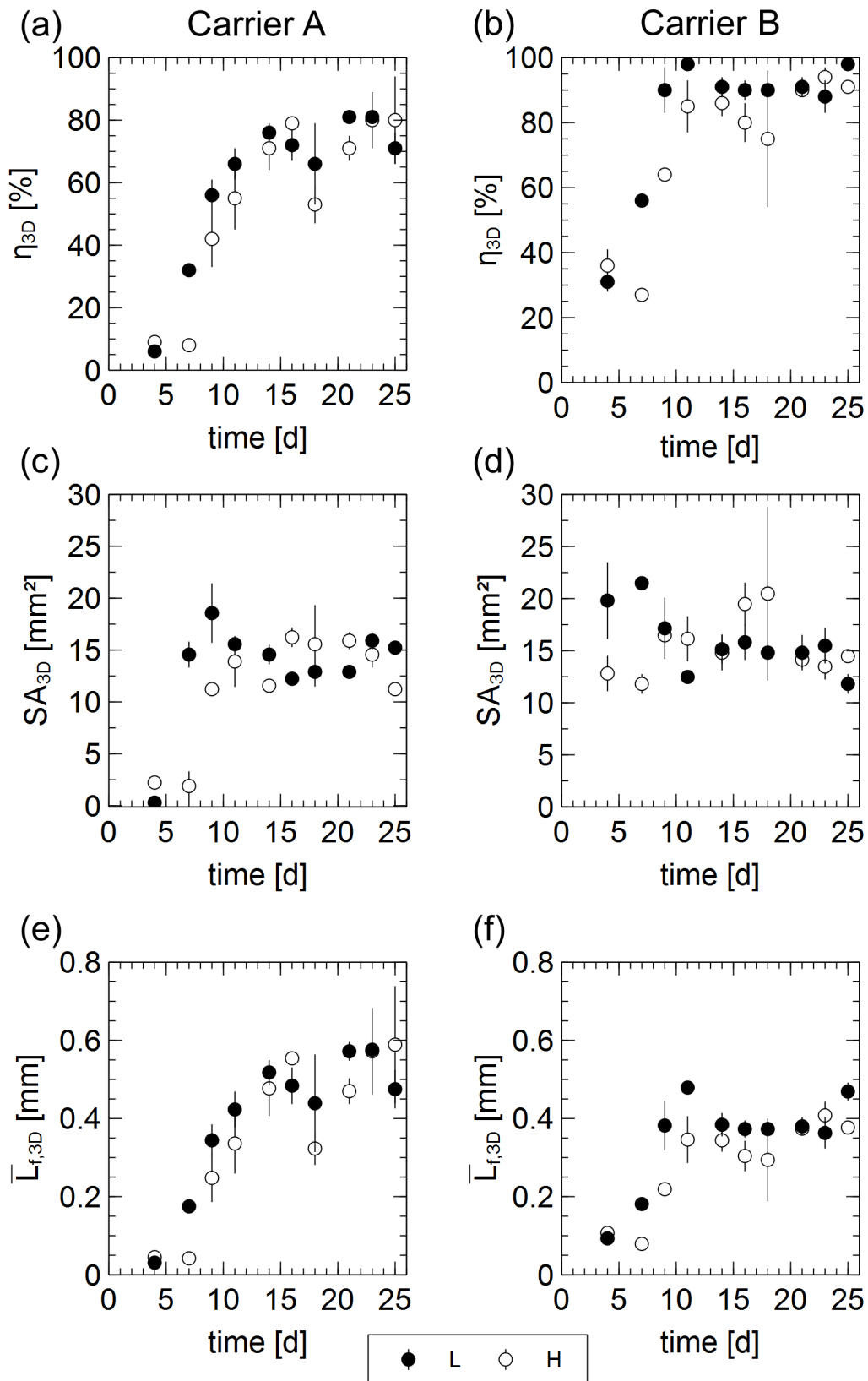For biofilm surface area SA_{3D} (for single compartment), the influence of aeration rate can be sep-

Figure 2.7: The effect of aeration rate on biofilm structure with respect to compartment filling degree (η_{3D}), surface area (SA_{3D}) and growth rate ($\mathbf{u}_{f,3D}$) for Carrier A (a), (c), (e) and Carrier B (b), (d) and (f) respectively.

arated into two phases, see Figure 2.7(c) and (d). For young biofilms (< 11 day) on both carriers, low aeration rates resulted in fast biomass accumulation thereby boosting SA_{3D}. High aeration rates led to low biofilm surface area. After day 11 the discrepancy in SA_{3D} diminished, while SA_{3D} kept relatively constant. The average biofilm thickness $\overline{L}_{f,3D}$ was always higher at low aeration rate compared to the results of high aeration rate, for both carrier geometries (Figure 2.7(e) and (f)). Although growing slower, SA_{3D} at high aeration rate enlarged steadily without decreasing trend. It is speculated that high aeration rate boosted fast movement of carriers in the reactor. Thereby, the carriers experienced higher shear forces. This led to the formation of smooth and compact biofilms, which is in accordance to the results of Liu and Tay (2002).

Despite the slight difference in biofilm structure between the low and high aeration rate at the beginning, the difference diminished when the carriers were filled with biomass. Referring to the reactor performance shown in Figure A.1, the difference in COD removal in the end was comparable, providing DO was above $7\,mg\cdot L^{-1}$ at both aeration rates. This implies that the aeration rate as high as $250\,L\cdot h^{-1}$ did not necessarily improve the COD removal. On the contrary, energy could be saved providing relatively lower aeration rate.

2.3.5   Correlation between 2D and 3D structure parameters

Imaging with light microscopy can provide a quick impression and overview of the biofilms developed on carriers. As a similar parameter set has been used to characterize biofilm structure based on both 2D and 3D images, the results were compared with respect to biofilm thickness ($\overline{L}_f$), growth rate (u_f), compartment filling degree (η) and surface enlargement (SE). The results are presented in Figure 2.8, with the same parameter pair plotted in one plot. The closer the points lying to the diagonal, the clearer the correlation between the results calculated from the two types of images.

In Figure 2.8(a), $\overline{L}_{f,2D}$ was compared with $\overline{L}_{f,3D}$. The points lying above the dashed line implies a $\overline{L}_{f,3D}$ greater than $\overline{L}_{f,2D}$, and *vice versa*. Most of the points lie close to the diagonal, which indicates that the $\overline{L}_f$ based on 2D and 3D images were close to each other, with $\overline{L}_{f,3D} = 0.5442 \times \overline{L}_{f,2D} + 0.1352$ ($R^2 = 0.76$). While on days 18, 23 and 25, $\overline{L}_{f,2D}$ were greater than $\overline{L}_{f,3D}$. As the calculation of η was similar to $\overline{L}_f$, the distribution of points for η (see Figure 2.8(b)) shows the same pattern as $\overline{L}_f$, with the majority of the points spreading along the diagonal and $\eta_{3D} = 0.7358 \times \eta_{2D} + 11.3$ ($R^2 = 0.90$). As has been illustrated in Figure 2.4(c), biofilms develop funnel-like structure with more biomass in the vertical center of the carrier and less biomass close to the two faces of the carrier. Before the compartments were blocked by biomass from the vertical center, $\overline{L}_f$ and η showed no significant difference between the results based on 2D and 3D images. However, after the compartments were blocked by biomass from the center after day 21, 2D imaging could not capture the structural differences anymore. 3D imaging with OCT could capture the further

change in biofilm structure, whereas, light microscopy was limited due to the projection of *3D* heterogeneous structure over the depth of the carriers. Therefore, the values for $\overline{L}_f$ and η on day 23 and 25 scattered further from the diagonal.
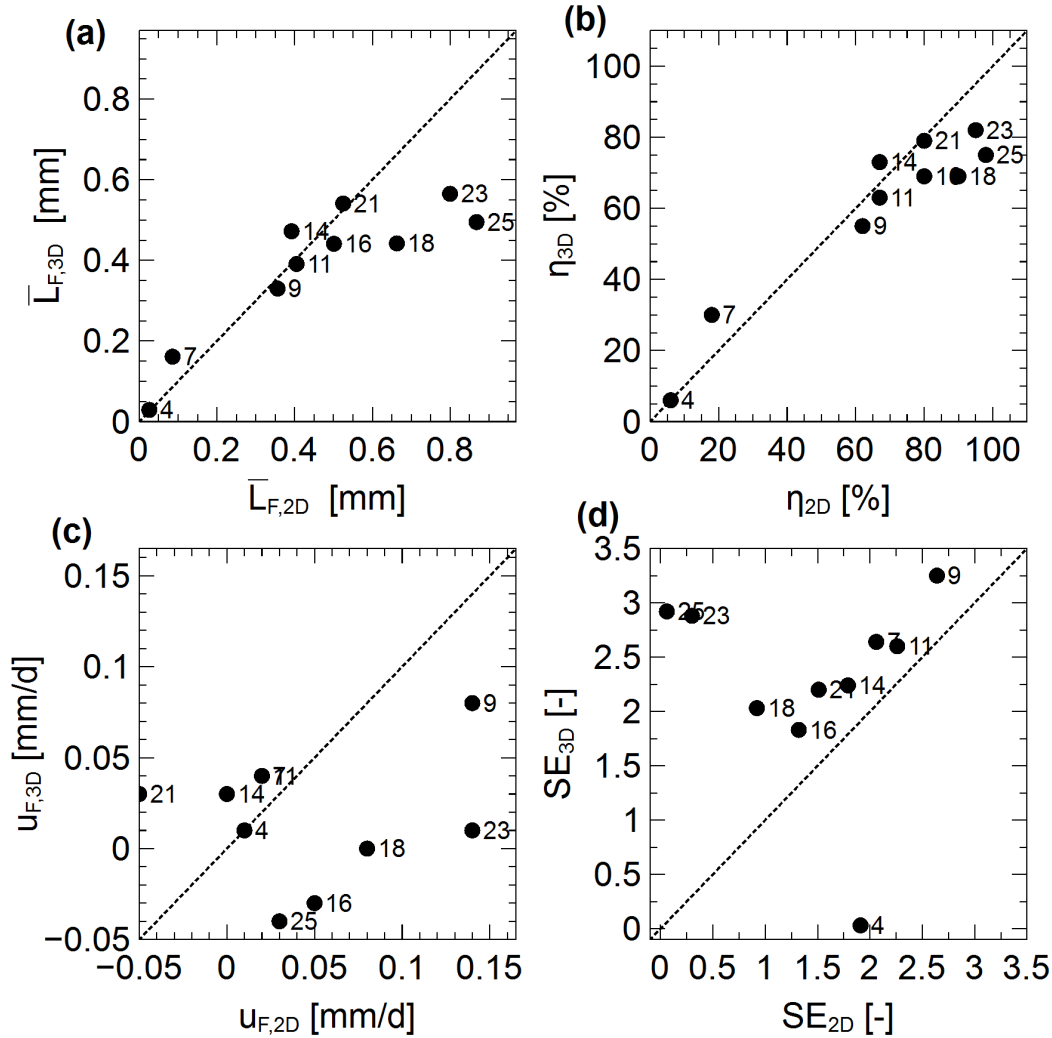
Figure 2.8: Correlation between the quantification based on light microscopy and OCT images with respect to (a) average biofilm thickness ($\overline{L}_f$), (b) compartment fill degree (η), (c) biofilm growth rate $\mathbf{u}_f$ and (d) surface enlargement (*SE*). The diagonal line represents a perfect correlation between the two variables plotted. The numbers label the day of the measurement.

The points of biofilm growth rate (u_f) in Figure 2.8(c) for the operation in the early phase (day 4 to 14) were along the diagonal. Afterward the points spread widely apart from (mostly below) the diagonal, which implies higher biofilm growth rate calculated from *2D* images. The points in Figure 2.8(d) on surface enlargement (*SE*) all lay above the diagonal except on day 4, which infers that the surface enlargement based on *3D* image dataset was always higher than that based on *2D* images. SE measures biofilm surface heterogeneity. OCT images were capable of capturing detailed *3D* hills and valleys at the biofilm surface. Projection of such *3D* structure onto a *2D* plane

led to loss of information, thereby a reduction of surface heterogeneity. The two measurements on day 23 and 25 in Figure 2.8(d) can be attributed partly to the blockage of the carrier compartments resulting in SE_{2D} approaching 0.

Comparison between the results extracted from 2D and 3D images suggests that 2D analysis could replace the 3D analysis to monitor the overall biofilm growth with respect to the development of the average biofilm thickness and carrier compartments filling degree before the compartments were completely filled with biomass. Another advantage of 2D imaging is the larger coverage allowing more area to be included in the quantification. However, 2D imaging cannot replace 3D imaging when the heterogeneous surface structure is of concern, such as surface enlargement. The study of Zielinski et al. (2012) also showed the superior accuracy of 3D over 2D analysis for CLSM images. OCT provided more detailed information on biomass distribution inside the compartment as well as the heterogeneous 3D biofilm surface structure, which cannot be captured by 2D imaging. While light microscopy only revealed the overall structural information of a compartment, OCT could explicitly visualize local variation of biofilm growth and provide more descriptive information on biofilm structure by 3D structure analysis.

2.4   Conclusion

The objective of this study was to characterize the structure development of biofilms grown on plastic carriers used in lab-scale MBBRs under high and low aeration rates. Image analysis based on light microscopic images (2D) and OCT images (3D) were conducted with respect to a set of structural parameters often used in biofilm research. The following conclusions can be drawn:

- The complex 3D biofilm structure inside the carriers was visualized and characterized with OCT. OCT images revealed funnel-like biofilm structure with more biomass in the vertical center of the compartments and less biomass at carrier surfaces, as well as heterogeneous biofilm surface structure.

- The carriers with the small compartment size and high protected surface area promoted quick establishment and growth of biofilms. Nevertheless, the carriers with the big compartment size and low protected surface area reached higher biomass volume and biofilm surface area after the carriers were filled with biomass.

- Low aeration rates allowed fast biofilm development and a higher compartment filling degree on both types of carriers.

- 2D imaging may substitute 3D imaging to monitor general structural development, based on the simple parameters, such as average biofilm thickness and compartment filling degree.

Before the carrier compartments were completely filled, there was strong correlation for $\overline{L}_f$ and η between $2D$ and $3D$ images with $\overline{L}_{f,3D} = 0.7227 \times \overline{L}_{f,2D} + 0.084$ ($R^2 = 0.82$) and $\eta_{3D} = 0.7358 \times \eta_{2D} + 11.3$ ($R^2 = 0.90$), respectively. However, $3D$ imaging with OCT provided more descriptive information on biofilm structure, such as the distribution of biomass in the compartment, biomass volume and biofilm surface area.

Chapter 3

Assessing the influence of biofilm surface roughness on mass transfer

3.1 Introduction

When microorganisms attach to surfaces in an aquatic environment, they form biofilms, the dominating style of microbial life on Earth. Depending on the cultivation environment, biofilms exhibit different structures: smooth or rough, porous or dense. It is known that biofilm structure has a strong impact on biofilm activity (Picioreanu et al., 2004). Therefore, determining biofilm structure is of great importance in biofilm research.

As one of the major approaches in biofilm research, mathematical modeling has become one of the essential tools to gain mechanistic understanding of systems with complex interactions, such as biofilms in streamers (Taherzadeh et al., 2012). A homogeneous planar biofilm structure is often assumed in simplified one-dimensional (1D) models, as in the widely used one from Wanner and Reichert (1996). This assumption limits the applicability of such models when biofilm surface heterogeneity is important and required as input. Multi-dimensional models can incorporate the spatial heterogeneity of biofilm structure and can provide insights into the spatial distribution of state variables (e.g., substrate gradients) (Picioreanu et al., 2004) and the structure-activity relationship by applying conditions close to reality (Eberl et al., 2000). So far, the behavior of biofilms can be modeled with the following approaches: cellular automata (CA) (Laspidou and Rittmann, 2004a), individual-based models (Kreft et al., 2001), particle-based models (Picioreanu et al., 2004) and the continuum approach (Alpkvist and Klapper, 2007). Even with the simplifications that still have to be made, the quantitative nature of a biofilm model provides details on a conceptual understanding and allows a rigorous evaluation of this understanding against experimental results.

In another branch of biofilm research, various imaging techniques have been applied to investigate

the physical and biochemical properties as well as the composition of biofilms, such as CLSM (Lawrence and Neu, 1999), MRI (Manz et al., 2003), RM (Ivleva et al., 2009) and SEM (Janjaroen et al., 2013), to name just a few. However, their application is limited due to incomplete staining of biofilm constitutes (CLSM) or altering the biofilm structure due to drying (SEM), not being representative due to imaging at micro-scale (CLSM, SEM) or high costs for instrumentation and time (MRI).

Originally invented for medical diagnostics (Huang et al., 1991), optical coherence tomography (OCT) has recently been introduced into biofilm research to reliably monitor biofilm development at mm-scale (meso-scale) (Wagner et al., 2010b; Xi et al., 2006). It compensates the afore-mentioned limitations and enables fast, *in situ* and non-invasive three-dimensional visualization of biofilm structure at the meso-scale and thus exhibits high potential in biofilm research. Typically biofilm imaging and mathematical modeling are used separately. There have very seldom been in-teractions between the two approaches (Böl et al., 2009; Pavissich et al., 2014). Within this study, we developed a method that combines biofilm imaging at the meso-scale by means of OCT with the purpose of using the imaging data as structural templates within a 2D biofilm model to assess the impact of biofilm structure on local mass transfer. Comparison between real biofilm structures and an artificial flat biofilm structure was conducted to investigate the impact of biofilm surface heterogeneity.

3.2 Materials and methods

3.2.1 Biofilm imaging

The biofilm samples in the current study were grown in biofilm reactors with plastic carriers as substratum. The reactor was operated with glucose as the only carbon source. A GANYMEDE spectral domain OCT (Thorlabs GmbH, Dachau, Germany) with a central wavelength of $930\,nm$ was used to visualize the biofilm structure. For image acquisition the carrier was placed in an in-house made carrier holder and immersed into filtered ($< 0.45\,\mu m$) bulk liquid from the reactor. The image spanned $2.8\,mm$ in width. The images have a lateral resolution of $10.7\,\mu m \cdot pixel^{-1}$ and an axial resolution of $2.09\,\mu m \cdot pixel^{-1}$.

3.2.2 Image analysis and characterization of biofilm structure

Image processing was conducted using Fiji software package (Schindelin et al., 2012). The com-plete biofilm structure throughout the vertical cross-section of the carrier was achieved by com-bining two B-scans acquired at the same location from both sides of the carrier, with each B-scan

contributing 50% of the carrier thickness. After binarization by setting a manual threshold, the surface of the biofilm was clearly identifiable. Isolated white noise pixels were removed with the 'Remove outlier' function of Fiji. Compact biofilm was assumed, thus the space beneath the biofilm surface was treated as completely filled with biomass. In the last step the plastic grids of the carrier were outlined and removed from the images to allow the model to distinguish between the plastic carrier and the grown biofilm.

Based on the binarized images, biofilm structures were characterized with respect to roughness coefficient (R'_a) (Murga et al., 1995) and surface enlargement factor (α) (Picioreanu et al., 1998), calculated according to Equation 3.2.1 and Equation 3.2.2, respectively.

$$R'_a = \frac{1}{N} \sum_1^N \left(\frac{|L_{f,i} - \overline{L_f}|}{\overline{L_f}} \right) \tag{3.2.1}$$

$$\alpha = \frac{L_\Gamma}{L_S} \tag{3.2.2}$$

where $L_{f,i}$ is the biofilm thickness at point i, $\overline{L_f}$ the average biofilm thickness, N the number of points engaged in the calculation, L_Γ the measured length of the liquid-biofilm interface, L_S is the length of the substratum.

3.2.3   Model structure

Binarized OCT datasets were transferred into COMSOL Multiphysics 4.4 (COMSOL Inc., Sweden) as structural templates of the biofilm grown inside two adjacent compartments of the carrier. Fluid flow, mass transport and biochemical conversion of substrates under steady state flow conditions were incorporated into the model. For simplicity, simulations in this study were restricted to steady state, incompressible flow in the space close to the carrier surface. Flow, both parallel to the carrier surface and through the compartments, was simulated. The simulation domain was extended by $1.5\,mm$ above as well as below the carrier surface so as to incorporate a fully developed flow field. Based on this adjustment, the motion of the bulk liquid in the simulation domain can be characterized by the velocity field $\mathbf{u}$, which is governed by the Navier-Stokes equations:

$$\rho(\mathbf{u} \cdot \nabla)\mathbf{u} = -\nabla P + \mu \nabla^2 \mathbf{u} \tag{3.2.3}$$

$$\nabla \cdot \mathbf{u} = 0 \tag{3.2.4}$$

where Equation 3.2.3 is the balance of inertial, pressure and viscous forces, and Equation 3.2.4 is the continuity equation that describes the incompressibility-induced mass balance. $\mathbf{u}$ is the vector

of the local liquid velocity, ρ is the liquid density, μ is the liquid dynamic viscosity and P is the pressure. A fully developed laminar velocity profile with different inflow velocities was assigned to the inlet of the simulation domain for the parallel and flow through cases, respectively. Flow leaves the domain at the right side for the parallel flow case and at the lower boundary for the flow through condition, respectively. Symmetrical boundary conditions were applied forcing the liquid to flow through the compartments in the flow through mode.

In agreement with Picioreanu et al. (2000) and Pavissich et al. (2014), rigid biofilm structure was assumed. Dissolved components include organic substrate, characterized by chemical oxygen demand (COD), and dissolved oxygen (DO). Transport of dissolved components in the bulk liquid by convection and diffusion was described by Equation 3.2.5:

$$\nabla \cdot (-D_i \nabla S_i) + \mathbf{u} \cdot \nabla S_i = r_i \tag{3.2.5}$$

where D_i is the diffusivity of substrate i, S_i the concentration of substrate i in the bulk liquid and r_i the turnover of substrate i. Inside the biofilm domain, diffusion and substrate turnover by the biomass were incorporated. The diffusivity of substrates within biofilms was assumed to equal 80% of that in the bulk liquid (Horn and Morgenroth, 2006; Stewart, 2003).

Substrate flux is continuous at liquid-biofilm interface. COD ($148\,mg \cdot L^{-1}$) concentration in the bulk liquid measured on the day when the images were taken was used for all the simulations. Substrate conversion was only considered in the biofilm domain. Aerobic conversion of COD by heterotrophic bacteria followed a dual Monod kinetic (Henze, 2000) and is given by Equation 3.2.6 and Equation 3.2.7, respectively.

$$r_{COD} = -\frac{1}{Y_H} \mu_H \left(\frac{S_{COD}}{k_{COD} + S_{COD}} \right) \left(\frac{S_{DO}}{k_{DO} + S_{DO}} \right) \tag{3.2.6}$$

$$r_{DO} = -\frac{1 - Y_H}{Y_H} \mu_H \left(\frac{S_{COD}}{k_{COD} + S_{COD}} \right) \left(\frac{S_{DO}}{k_{DO} + S_{DO}} \right) \tag{3.2.7}$$

The values for all stoichiometric and kinetic parameters were set according to the Activated Sludge Model No.1 (Henze, 2000) and are provided in Table 3.1. Growth and inactivation of microorganisms were not considered within this study. Biomass density was defined as only for the active biomass homogeneously distributed over the entire biofilm domain. Two values, low ($15,000\,g \cdot m^{-3}$) and high ($30,000\,g \cdot m^{-3}$), were used for the simulation.

3.2.4   Data evaluation

The mass conversion performance was evaluated with COD boundary flux according to Fick's law:

Table 3.1: Model parameters

Symbol	Value	Dimension	Description	Reference
Stoichiometric parameters				
Y_H	0.67	$gCOD \cdot gCOD^{-1}$	Heterotrophic yield coefficient	Henze (2000)
Kinetic parameters				
μ_H	6	d^{-1}	Maximum specific growth rate of X_H	Henze (2000)
K_{COD}	20	$gCOD \cdot m^{-3}$	Half-saturation coefficient for substrate S	Henze (2000)
K_{DO}	0.2	$gO_2 \cdot m^{-3}$	Half-saturation coefficient for O_2	Henze (2000)
Additional parameters				
D_{COD}	$1.20e^{-9}$	$m^2 \cdot s^{-1}$	Diffusivity of COD in water	Picioreanu et al. (1997)
D_{DO}	$2.00e^{-9}$	$m^2 \cdot s^{-1}$	Diffusivity of DO in water	Picioreanu et al. (1997)

$$J_{COD} = -D_{COD} \frac{\partial S_{COD}}{\partial n} |_{\Gamma} \qquad (3.2.8)$$

The local convective and diffusive fluxes were calculated based on Equation 3.2.9 and Equation 3.2.10 respectively for the whole simulation domain.

$$J_C = S_{COD} \sqrt{u_x^2 + u_y^2} \qquad (3.2.9)$$

$$J_D = D_{COD} \sqrt{(\frac{\partial S_{COD}}{\partial x})^2 + (\frac{\partial S_{COD}}{\partial y})^2} \qquad (3.2.10)$$

The Sherwood number (Sh) is a dimensionless number used to characterize the mass transfer characteristics and represents the ratio of convective to diffusive mass transport. For a given system, the higher the Sh, the better the mass transfer from the bulk liquid into the biofilms. The locally resolved Sherwood number can be calculated according to Equation 11:

$$Sh = \frac{k_S L_h}{D_S} = \frac{-L_h \frac{\partial S_i |_{\Gamma}}{\partial n}}{(S_{i,0} - S_{i,\Gamma})} \qquad (3.2.11)$$

The characteristic length (L_h) selected is of great importance to the values calculated for Sh. In this study the width of the simulation domain, $2.8\,mm$, was chosen for this calculation. Referring to Picioreanu et al. (2000), the spatial averaged Sherwood number is more convenient for the

comparison of the overall mass transfer characteristic of the whole simulation domain among the different simulation scenarios. It can be calculated by averaging Sh over biofilm surface Γ as given in Equation 12:

$$\overline{Sh} = \frac{\int_{\Gamma} Sh \cdot dL_{\Gamma}}{L_{\Gamma}} \tag{3.2.12}$$

3.3 Results

3.3.1 Biofilm images obtained with OCT

The structure of biofilms on carriers was obtained by means of OCT. Two cross-sectional OCT images, referred to as geometry 1 ($G1$) and geometry 2 ($G2$), are presented in Figure 3.1 (a) and (b). Both geometries resemble slightly different biofilm structure on the carrier with respect to L_{Γ}, R_a' and α, presented in Table 3.2. Their effect on mass transfer was investigated. Biofilms inside the carrier compartment grew inwards from the plastic carrier walls. Heterogeneous structures with small spikes developed along the carrier walls, which can be clearly seen from the binarized images in Figure 3.1 (c) and (d). The white part in Figure 3.1 (c) and (d) is referred to as biofilm area. A simplified flat geometry was generated having the same biofilm area as the real biofilm structures. However, there was a distinctive difference with respect to the liquid-biofilm interface length (L_{Γ}) as well as biomass distribution between the real and the simplified structures. Compared to the smooth geometry, the heterogeneous biofilm structure doubled L_{Γ} (see Table 3.2). With the same substratum length, the presence of spikes in the real biofilm structure enlarged the biofilm surface, namely L_{Γ}. This further led to a high roughness coefficient and a high surface enlargement factor. $G1$ had slightly higher L_{Γ}, thereby a higher surface enlargement factor and R_a'.

Table 3.2: Structure parameters for all the geometries used

			Geometry 1	Geometry 2	Simplified
Biofilm area	A	$[mm^2]$	0.98	1.00	0.98
Interface length	L_{Γ}	$[mm]$	10.7	10.08	5.32
Roughness coefficient	R_a'	$[-]$	0.34	0.31	0.23
Surface enlargement	α	$[-]$	2.50	2.34	1.24

3.3.2 Simulated velocity and concentration field

To demonstrate the applicability of the method combining biofilm imaging and biofilm modeling, geometries were transferred into COMSOL to serve as structural templates, which allowed studying

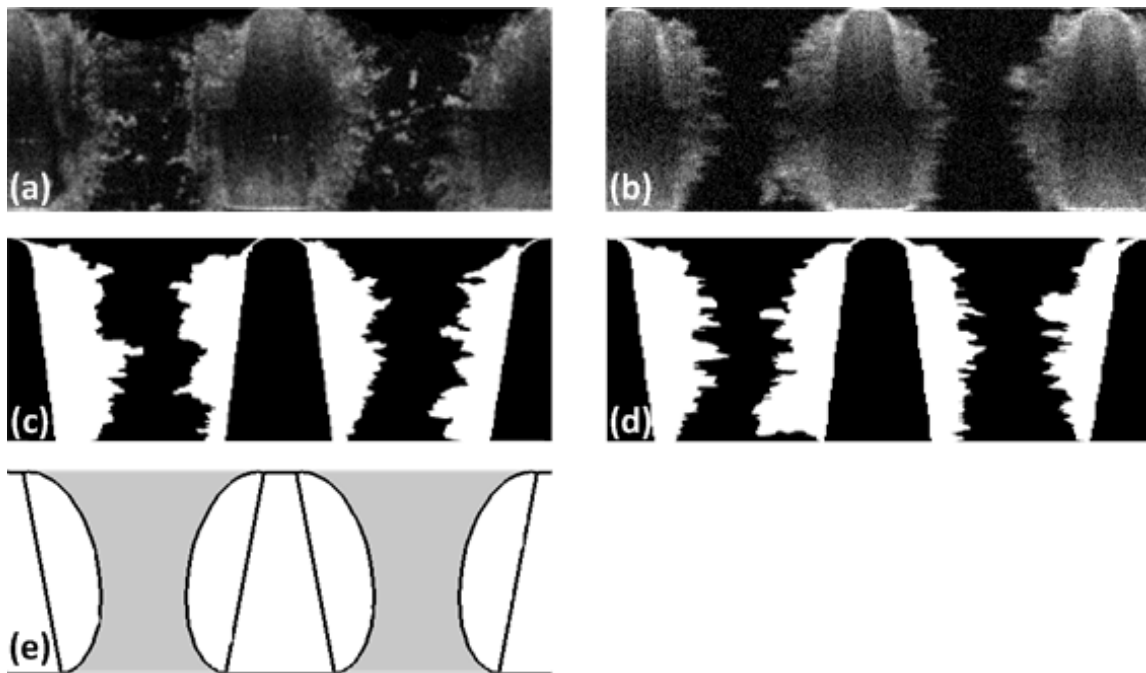Figure 3.1: Cross-sectional OCT images of biofilm developed on the carrier. (a) and (b) are raw gray scale biofilm images. (c) and (d) are the binarized images for (a) and (b) respectively. (e) presents the simplified biofilm structure that has the same area as the structures in (c) and (d). The dimension of one image is $2.8 \times 1.05 \, mm^2$ and represents a cross section through two compartments in the vertical xz-plane.

the interaction between the biofilm structure and the surrounding fluid. The simulated flow field in the vicinity of and inside the two adjacent compartments is presented in Figure 3.2(a). Figure 3.2(b) presents the simulated flow field around the simplified biofilm structure under the same simulation conditions. The arrows indicate the formation of cyclic flow inside the carrier compartments for both biofilm geometries. From red to blue color, the figure shows that fluid velocity decreases from $8\,cm \cdot s^{-1}$ to 0 near the biofilm surface.

The convective and diffusive transport of substrates was coupled to the flow simulation. Figure 3.2(c) and (d) present the simulated distribution of DO in the bulk and in the biofilm matrix under the influence of the flow field. The figures show that DO concentration decreased steadily from $8\,mg \cdot L^{-1}$ at biofilm surface to less than $1\,mg \cdot L^{-1}$ near the plastic of the carrier and became limited in the deeper layer of the biofilm. The green color inside the compartments in Figure 3.2(c) suggests that bulk liquid could not flow through the compartments, thereby forming regions with only diffusion transport. Whereas in Figure 3.2(d) the bulk liquid flew through the compartments and transported the substrate deep into the compartments. COD concentration fields exhibit the same pattern for the corresponding geometry (data not shown).

The activity of the biomass with respect to COD consumption, calculated based on Equation 3.2.6, is visualized in Figure 3.2(e) and (f) for $G1$ and the simplified biofilm structure, respectively. Biofilms reached the highest activity of $1.34\,g \cdot m^{-3} \cdot d^{-1}$ at the biofilm surface where the substrates were not limited. Away from the biofilm surface, biomass activity decreased steadily as DO concentration decreased towards the substratum and formed a distinctive 'belt'. This was even more obvious for the simplified biofilm structure (see Figure 3.2(f)).

3.3.3   The influence of flow velocity, DO and biomass density on COD fluxes

The model was also used to investigate the influence of flow velocity, substrate concentration and biomass density on COD boundary fluxes and mass transfer properties. COD fluxes were calculated to represent biomass performance. In both, parallel and through flow mode, different combinations of flow velocity (0.001, 0.01, 0.1, 1 and $5\,cm \cdot s^{-1}$) and DO concentration (0.01, 0.1, 1, 4 and $8\,mg \cdot L^{-1}$) were tested. Velocities and DO concentrations were selected in such a wide range to simulate variations in more or less realistic conditions. Thereby, the impact of the biofilm surface structure should be revealed. Additionally, the effect of biomass density was studied.

The parallel flow mode

The performances of biofilm with real and simplified geometry in terms of COD fluxes were compared for different flow conditions and DO concentrations. The results are presented in Figure 3.3(a) and (b). The relative difference of COD fluxes is derived by dividing the absolute difference
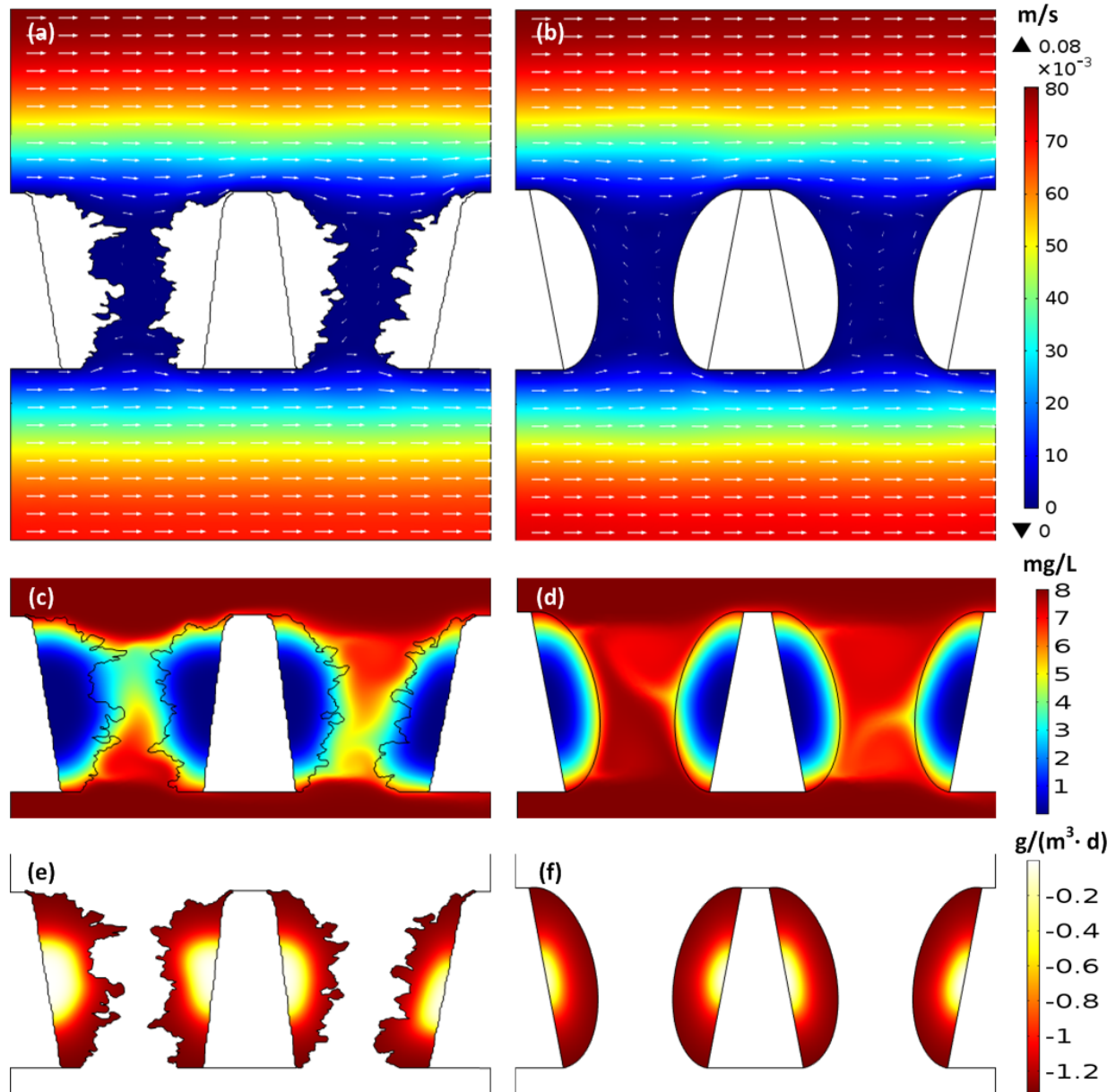
Figure 3.2: Simulated flow field (a) and (b), DO concentration field (c) and (d), and COD removal activity map (e) and (f) for real and simplified geometry respectively. The arrows in (a) and (b) indicate flow velocity. The width of the arrows is proportional to the calculated flow velocity (in $log10$ scale). The bulk liquid flows from left to right under laminar flow condition with an inflow velocity of $u = 0.05\,cm \cdot s^{-1}$. To get a closer look at the interaction between biofilm structure and fluid flow, the images for DO concentration field and the activity map were cropped to the most interesting part around biofilm and the carrier surface. DO concentration in the inflow equals $8\,mg \cdot L^{-1}$. COD removal rate has a dimension of $g \cdot m^{-3} \cdot d^{-1}$. The negative values indicate consumption of COD. The figures have a dimension of $2.8 \times 1.4\,mm^2$.

(see Figure A.2) by the COD boundary fluxes of the real geometry. Referring to Figure 3.3(a), under low flow velocity conditions ($u \leq 0.1 \, cm \cdot s^{-1}$) the differences are positive, which implies that heterogeneous biofilm geometries had better performance with respect to COD fluxes from bulk liquid into the biofilm. However, the difference is low (less than 5%). The negative differences for flow velocities higher than $0.1 \, cm \cdot s^{-1}$ indicate that the smooth biofilm had better performance (up to 20%) than biofilms with heterogeneous structure. Similar results were derived at biomass density of $30,000 \, g \cdot m^3$ (see Figure 3.3(b)).
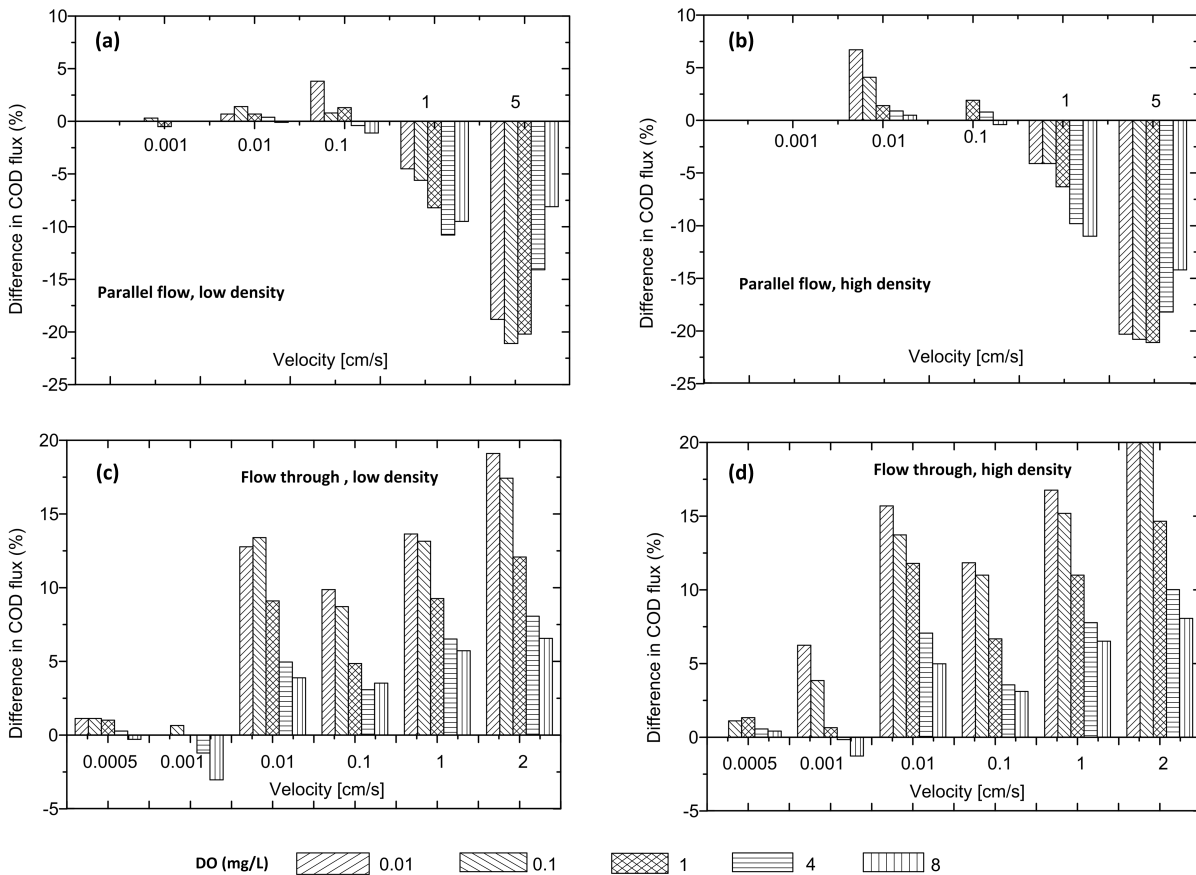
Figure 3.3: Relative difference in COD flux between the real and simplified geometries under different flow and substrate concentration conditions for parallel flow ((a) and (b)) and through flow ((c) and (d)) at low ((a) and (c)) and high ((b) and (d)) biomass density. In (d) the maximum different at DO of 0.01 and $0.1 \, mg \cdot L^{-1}$ is exactly 20%. Positive values indicate higher COD flux for the real geometry over the simplified geometry. Negative values suggest lower COD flux for the real geometry. All the simulations were conducted with same COD concentration ($148 \, mg \cdot L^{-1}$) in the inflow.

It is clear that at same DO concentration, the higher the flow velocity was, the larger the difference in COD flux between the rough and the flat biofilm got. Meanwhile, at the same flow velocity, the higher the DO concentration was, the lower the difference in COD boundary flux. For example in Figure 3.3(a), at flow velocity of $u = 5 \, cm \cdot s^{-1}$ and low biomass density, the difference was as

high as 19% at a DO concentration of $0.01\,mg \cdot L^{-1}$. It decreased to 8% at the DO concentration of $8\,mg \cdot L^{-1}$.

To illustrate the variation in the relative difference in COD fluxes presented in Figure 3.3(a) and (b), the dominance of diffusive and convective mass transport in the simulation domain was compared according to Equation 3.2.9 and Equation 3.2.10. As an example, the results for $DO = 8\,mg \cdot L^{-1}$ under different flow velocities are plotted in Figure 3.5 for both the real and simplified geometry. The color scale shows where the convective flux dominates, while the gray scale indicates where diffusive flux is higher than convective fluxes. Seen from Figure 3.5(a) and (b), at low flow velocity, diffusion was the only transport mechanism in the whole simulation domain. With increasing flow velocity, convective fluxes became more and more important compared to diffusive fluxes. As flow increased, areas of diffusion dominance shrank, and the area of convection dominance expanded. At $u = 0.1\,cm \cdot s^{-1}$ diffusion still prevailed inside the carrier compartments. However, seeing from Figure 3.5(e) and (f), the transport of substrates in the bulk liquid outside of the compartments was taken over by convection. At $u = 1\,cm \cdot s^{-1}$ in Figure 3.5(h), the compartments with the smooth geometry became dominated by convection, but not the compartment with real geometry. At $u = 5\,cm \cdot s^{-1}$, convective transport dominated the whole liquid domain (Figure 3.5(i) and (j)).

To characterize mass transfer in the simulation domain, spatially averaged Sherwood numbers ($\overline{Sh}$) were calculated and are summarized in Table 3.3. For the real geometry, at $DO = 0.01\,mg \cdot L^{-1}$, ($\overline{Sh}$) increased from 1.84 to 27.5 with flow velocity increasing from 0.001 to $5\,cm \cdot s^{-1}$. The same trend was also observed for the flat geometry: $\overline{Sh}$ increased from 3.8 to 69.4 when flow velocity increased from 0.001 to $5\,cm \cdot s^{-1}$ at $DO = 0.01\,mg \cdot L^{-1}$. However, at a given flow velocity there existed only a minor variation of $\overline{Sh}$ even with a hundred-fold increase in DO concentration (0.01 to $1\,mg \cdot L^{-1}$). At the same DO concentration and flow velocity, $\overline{Sh}$ for the smooth geometry was around twice of that for the real geometry, e.g., 3.8 and 1.8 for the flat and real geometry, respectively, at $u = 0.001\,cm \cdot s^{-1}$ and $DO = 0.01\,mg \cdot L^{-1}$.

The flow through mode

As previously presented, in the parallel flow cases not the whole biofilm surface is active, especially for the cases with low flow velocity and DO concentration. To verify how biofilm surface heterogeneity may influence biofilm performance in terms of COD flux, different flow through scenarios were tested. A maximum velocity of $2\,cm \cdot s^{-1}$ was assumed. The flow velocities investigated included 0.0005, 0.001, 0.01, 0.1, 1 and $2\,cm \cdot s^{-1}$. DO concentrations and biomass densities tested were the same as in the parallel flow cases.

Similar to the parallel flow cases, COD fluxes at the biofilm surfaces for the real and flat geometries were compared. The results (relative difference) are plotted in Figure 3.3(c) and (d). For both low $(15,000\,g \cdot m^{-3})$ and high $(30,000\,g \cdot m^{-3})$ biomass density, the differences were generally positive. There was a minor difference in COD flux between the two geometries at $u \leq 0.01\,cm \cdot s^{-1}$. A
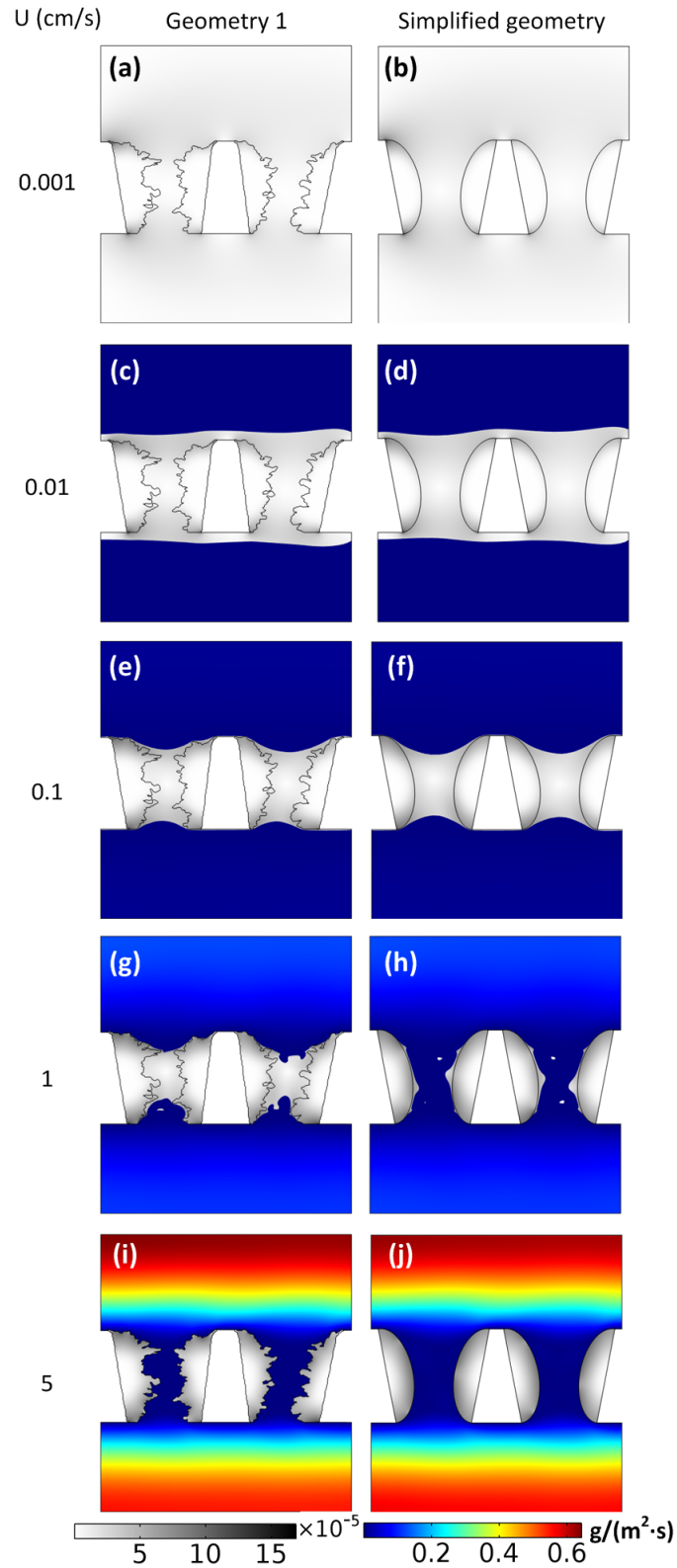
Figure 3.4: Transition from diffusion to convection dominated mass transport at DO $8\,mg \cdot L^{-1}$ for parallel flow conditions. The gray scale represents the dominance of diffusion at a magnitude of $10^{-5}g \cdot m^{-2} \cdot s^{-1}$. Convection prevails in the colored region. The legend applies for all the subfigures.

Table 3.3: Spatial averaged Sherwood number calculated for G1 under different flow and substrates conditions for low biomass density and the parallel flow conditions ($15000\,g \cdot m^{-3}$)

DO ($mg \cdot L^{-1}$)	$u(cm \cdot s^{-1})$	0.001	0.01	0.1	1	5
0.01	Real	1.8	3.5	7.2	15.6	27.5
	Simplified	3.8	7.1	14.4	33.3	69.4
0.1	Real	1.8	3.5	7.2	15.6	27.5
	Simplified	3.7	7.1	14.4	33.0	69.5
1	Real	1.8	3.5	7.3	15.6	26.7
	Simplified	3.7	7.1	14.6	33.3	69.7
4	Real	1.8	3.5	7.5	15.1	25.5
	Simplified	3.7	7.1	14.7	33.2	68.9
8	Real	1.8	3.5	7.1	14.8	24.8
	Simplified	3.7	7.1	14.6	33.0	68.3

sharp rise appeared when the flow velocity increased from 0.001 to $0.01\,cm \cdot s^{-1}$. At the same flow velocity, the difference became smaller with increasing DO concentration. At a given DO concentration, the relative differences in COD flux generally increased with rising flow velocity. The maximum difference of 19% and 20% were reached at $u = 2\,cm \cdot s^{-1}$ and $DO = 0.01\,mg \cdot L^{-1}$ for low and high biomass densities, respectively.

The diffusion-convection plots are presented in Figure 3.5 to visualize the relation between the two mass transport processes. At very low flow velocity ($0.0005\,cm \cdot s^{-1}$), the domain was dominated by diffusion for both real and smooth geometry. As flow rate increased, convection started to play a role, see Figure 3.5(d). The prevalence of convection in the domain started already at $u = 0.01\,cm \cdot s^{-1}$ for the flat biofilm. While for the real biofilm structure it was one magnitude higher at $u = 0.1\,cm \cdot s^{-1}$. From this velocity onwards the whole bulk domain is characterized by convective transport.

3.3.4 Difference in simulation results between G1 and G2

The two geometries displayed in Figure 3.1 have the same biofilm area ($0.98\,mm^2$), which implies the presence of the same amount of biomass. Nevertheless, there was a slight difference in biomass distribution inside the compartments. The length of the interface was also different, with $10.7\,mm$ for G1 and $10.08\,mm$ for G2, respectively.

To reveal the impact of the differences in biofilm structure between G1 and G2, similar simulations were implemented for G2, with $u = 5\,cm \cdot s^{-1}$ and $u = 2\,cm \cdot s^{-1}$ for the parallel and flow through mode, respectively. DO of $8\,mg \cdot L^{-1}$ was used for the comparison. The flow velocity field and substrate distribution in the compartments were mapped and compared to those derived from simulations with G1. The results are presented in Figure 3.6. In Figure 3.6(a), flow circulated inside the
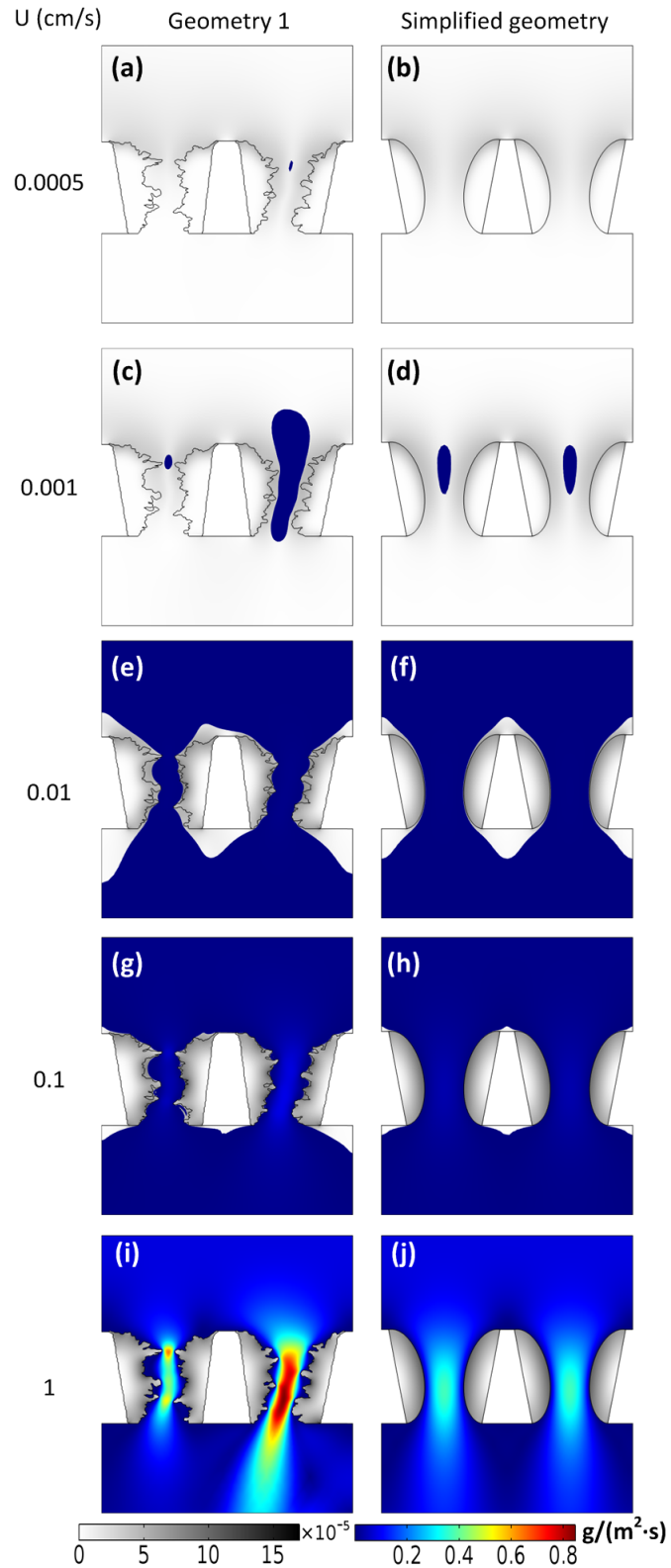
Figure 3.5: Transition from diffusion to convection dominated mass transport from low to high flow velocity at DO of $8\,mg \cdot L^{-1}$ for flow through conditions. The gray scale represents the dominance of diffusion at a magnitude of $10^{-5}\,g \cdot m^{-2} \cdot s^{-1}$. Convection prevails in the colored region. The legend applies for all the subfigures.

compartments, whereas in Figure 3.6(b) water could flow through the compartment (see the direction of the arrows). The effect of the flow pattern on the substrate distribution is shown in Figure 3.6(c) and (d). Given the same inflow conditions, stagnant zones formed inside the compartments of G1, shown in light green color. Red color prevails in Figure 3.6(d), which suggests the absence of stagnant zones. In the flow through mode, it was clear that the presence of biomass could divert the liquid into different directions, thereby changing the flow field.

In addition to the qualitative visualization of the differences in hydrodynamics surrounding the biofilm, their corresponding performance with respect to COD fluxes at $DO = 8\,mg \cdot L^{-1}$ were also compared quantitatively and are listed in Table 3.4, as well as the $\overline{Sh}$ and pressure drop (ΔP) between the inlet and outlet boundary for all the three geometries.

Table 3.4: Comparison of COD fluxes ($g \cdot m^{-2} \cdot d^{-1}$), $\overline{Sh}$ and pressure drop (ΔP) among the different simulations with different biofilm geometries.

		Parallel flow ($u = 5\,cm \cdot s^{-1}$)			Flow through ($u = 2\,cm \cdot s^{-1}$)		
		G1	G2	Simplified	G1	G2	Simplified
COD	Low density	20.4	22.8	22.0	25.6	26.3	23.9
	High density	27.9	32.4	31.8	40.4	40.9	37.2
$\overline{Sh}$	-	24.8	41.8	68.3	103.5	132.9	192.7
ΔP	-	0.87	0.75	0.53	37.4	30.6	5.6

G2 achieved an 11% (low density) and 16% (high density) higher COD flux than G1 under parallel flow conditions. This difference diminished to 2% when water flew through the compartments. Substantial disparity in $\overline{Sh}$ existed between G1 and G2. In the parallel flow cases, $\overline{Sh}$ for G2 was 46, while it was only 25 for G1, both lower than $\overline{Sh}$ of 68 for the simplified biofilm geometry. In the through flow cases, $\overline{Sh}$ was 104 for G1 and 133 for G2, both of which were far lower than that for the flat biofilm with $\overline{Sh}$ of 193. In accordance to $\overline{Sh}$, ΔP also showed the same trend of decrease with the decreasing roughness coefficient from G1 to the flat geometry.

3.4   Discussion

3.4.1   The influence of biofilm structure on local hydrodynamics and mass transfer

The influence of biofilm structure heterogeneity on substrate mass transfer and biofilm performance is of great interest for the understanding of biofilm functions (de Beer et al., 1996; Eberl et al., 2000; Picioreanu et al., 2000). Based on the comparison among biofilms with different surface heterogeneities characterized by the roughness coefficient, the influence of biofilm structure will be discussed.
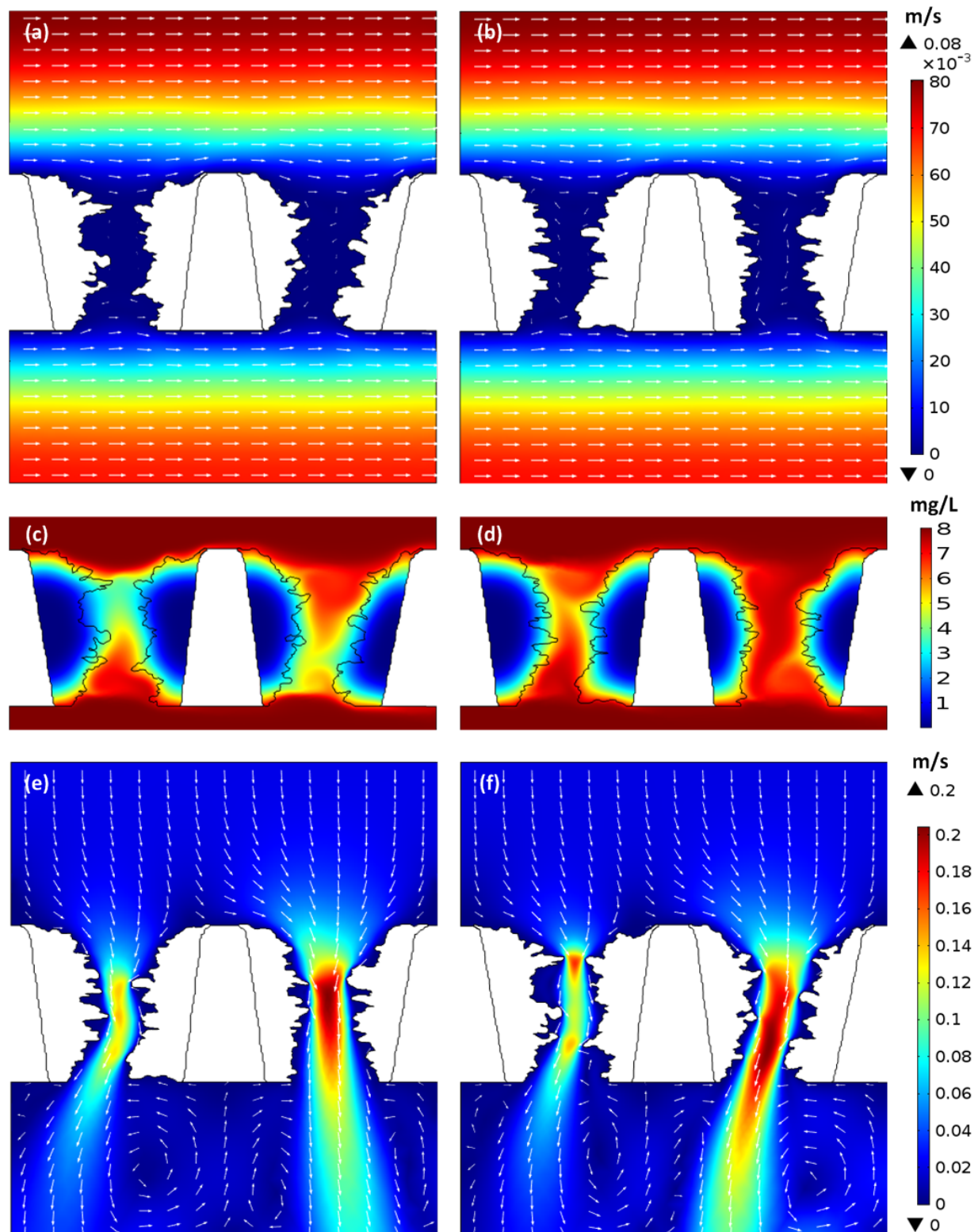
Figure 3.6: Flow field in parallel ((a) and (b)) and through flow mode ((e) and (f)) and DO concentration field simulated in parallel flow mode with G1 (left) and G2 (right).

Biofilm structure heterogeneity exerts strong influence on local flow hydrodynamics and mass transfer. As can be seen from Figure 3.2(a) and (b), with the same amount of biomass present, the flow field inside the compartments were quite different. Indicated by the arrows, cyclic flow formed inside the compartments with flat biofilm geometry. However, it was not visible in the compartments of the real biofilm geometry in Figure 3.2(a). The effect of such flow patterns was more evident in Figure 3.2(c) and (d), where the substrate distribution displayed noticeably different patterns inside the compartments of G1 and the smooth geometry. Compared to the flat biofilm geometry, the presence of small spikes on G1 weakens the formation of cyclic flow inside the compartments, leading to relatively week mass transfer, which is apparent from the light green color displayed in Figure 3.2(c). The convection-diffusion maps for G1 and the smooth biofilm structure depicted in Figure 3.4 and Figure 3.5 serve as further proof of weaker mass transfer of the heterogeneous biofilm structure under both parallel and through flow conditions. At flow velocity as low as $u = 0.001\,cm \cdot s^{-1}$, diffusion dominates the whole domain for both geometries. Within the range of the flow velocities tested, the convective mass transport picked up its importance with increasing flow velocity much faster for the smooth geometry than for G1. The influence of biofilm structure on mass transfer is further manifested by the calculation of $\overline{Sh}$ provided in Table 3.3. As expected $\overline{Sh}$ rose with increasing flow velocity, which is in accordance to the progressive increase of convection dominance illustrate in Figure 3.4. Nevertheless at a given flow velocity, $\overline{Sh}$ derived for the smooth geometry was around twice of the value for G1, which implies better mass transfer in the vicinity of biofilm surface for the smooth biofilm geometry.

Comparison between the simulations with G1 and G2 presented in Figure 3.6 revealed that despite the same amount of biomass and L_Γ present for both, slightly different distribution of biomass inside the compartments led to noticeably different local flow and substrate distributions. Presented in Figure 3.6, liquid could flow through the compartments of G2 under parallel flow conditions, thereby transporting the substrates deep into the compartments, which is not the case in Figure 3.6(c). Under flow through conditions, bulk liquid was forced to flow through the compartments. As shown in Figure 3.6(f), the presence of more biomass at the bottom right side of G2 forced the flow to change its direction after leaving the compartment. It was also clear that in the two compartments of the same geometry, the hydrodynamics can be significantly different. This is similar to the results revealed by the measurement with MRI by Herrling et al. (2014) showing that the uneven distribution of biomass in different compartments of a biofilm carrier resulted in uneven distribution of liquid flowing through the corresponding compartments. This further indicates that the small variance in biofilm structure would lead to significant differences in local hydrodynamics. Therefore, capturing biofilm structure as precise as possible is of critical importance when such detailed analysis at micro-scale is required.

Comparison of boundary COD fluxes under different flow conditions revealed that the influence

of biofilm surface heterogeneity depended strongly on flow conditions and the relative dominance of diffusive and convective mass transfer. Under the condition of pure diffusion domination, such as at $u \leq 0.1\,cm \cdot s^{-1}$ for the parallel flow and $u \leq 0.001\,cm \cdot s^{-1}$ for the flow through mode, the rough biofilm had slightly higher COD flux than the smooth biofilm. This might be explained by the difference in L_Γ. G1 has $10.7\,mm$ in L_Γ, which was twice of that for the smooth geometry. This also led to high surface enlargement as well as high roughness coefficient compared to the smooth geometry. Under the condition of weak external mass transfer, the increased roughness coefficient from 0.23 for the smooth geometry to 0.34 for rough G1 provided the rough geometry with more L_Γ (100% more), thereby more contact to substrate. For the parallel flow cases, the transition from diffusion to convection dominance led to better performance of smooth biofilm than rough biofilm. This was similar to the findings of Picioreanu et al. (2000) who concluded that the rough biofilm structure led to decreased conversion rates in the range of flow velocity simulated in that study.

In the flow through model, a sharp increase in the difference in COD flux between the two geometries appeared as convection became dominant in the compartments. This occurred when the velocity increased from 0.001 to $0.01\,cm \cdot s^{-1}$. With rising inflow velocity the difference became larger and larger, which was contradictory to the conclusion of Picioreanu et al. (2000). Picioreanu et al. (2000) stated that an advantage of the rough biofilm over the smooth one might be achieved with an increased convection. Nevertheless, due to stability and accuracy problems with the lattice Boltzmann method used in their study, biofilm behavior at high flow velocity was not simulated. In our case, as bulk liquid was forced to flow through the compartments, resulting in maximum flow velocity up to $u = 20\,cm \cdot s^{-1}$ in the compartments (see Figure 3.6(e)), the dominance of convection above biofilm surface rendered the whole biofilm surface to be active and contributed to substrate conversion. Therefore, the rough biofilm appeared to be advantageous over the smooth biofilm.

The effect of surface roughness on mass transfer can be well explained referring to the values of $\overline{Sh}$ and ΔP provided in Table 3.4. For both, parallel and flow-through conditions, $\overline{Sh}$ improved with decreasing roughness coefficient. The presence of biofilm spikes that increase the surface roughness of biofilms hindered the flow inside the compartments due to the friction at liquid-biofilm interface. The effect of the elevated friction led to more energy loss between the inlet and outlet boundary of the simulation domain, which showed in the increase of ΔP. For example, ΔP for the case of G1 ($37.4\,Pa$) was around seven times of ΔP for the smooth geometry ($5.6\,Pa$). Therefore, the mass transfer was hampered compared to their counterparts with smoother surface. By investigating the counter-diffusion autotrophic biofilms in a hydrogen-based membrane biofilm reactor, Pavissich et al. (2014) observed higher total substrate conversion in biofilms with higher roughness due to the increase of the active biofilm area. With the wide range of flow velocities, varying DO concentrations and different flow directions assessed, it seems that the influence of biofilm surface roughness on substrate removal depends strongly on the flow conditions. Under pure diffusion

conditions, the elevated roughness resulted in better substrate removal compared to the smooth geometry due to the increased liquid-biofilm interface length, thereby more contact to substrate. At high flow velocity, the improved mass transfer rendered the whole biofilm surface highly active, which also led to higher substrate removal. While for the conditions in-between, the smooth geometry exhibited better removal capacity than the rough biofilms.

3.4.2   The applicability of combining biofilm imaging and modeling

The results from the combination of imaging and modeling demonstrate the capability of this method to incorporate the real heterogeneous physical structure of biofilms into mathematical models. Our model allowed for a detailed description of the hydrodynamics at micro-scale, which is otherwise difficult to measure. It also showed that slight differences in biofilm structure led to significant difference in local hydrodynamics and thereby mass transfer characteristics.

The study of Böl et al. (2009) with a biofilm matrix converted from CLSM image stacks showed that the stress distribution in the biofilm heavily depended on biofilm structure. A change in biofilm structure influenced the stress distribution in the biofilms significantly, thereby influencing the detachment rate. Under such condition precise representation of biofilm structure is a prerequisite for the investigation. Therefore, detailed biofilm structure through imaging can offer better understanding of the system at micro-scale.

The method developed can be extended further to incorporate, for example, information on microbial composition. Information on microbial distribution that can be extracted, e.g. from FISH images, can be incorporated into the model so that the competition or synergistic effect among the species can be simulated based on the real distribution of different species. This can improve the model's accuracy by providing more realistic input, which otherwise often assumes to have homogeneous distribution of the microbial species throughout the biofilm matrix, as done in the study of Alpkvist and Klapper (2007). Nevertheless, FISH images are on a significantly smaller spatial scale compared to OCT images.

Similar to the assumption made by Pavissich et al. (2014), rigid biofilm structure was assumed in this study. Under the conditions with low flow velocity under flow through condition, the spikes may be able to withstand the shear stress so that the rough biofilm surface structure maintains. However, the (visco)elastic property of biofilms (Blauert et al., 2015; Klapper and Dockery, 2010) may alter the spikes, bending towards downstream under high flow velocity conditions. As biofilm surface becomes smooth and approaches a smooth surface, the liquid-biofilm interface would decrease to the value of the smooth biofilm structure, too. The advantage of the rough biofilm may vanish then. It might behave like biofilms with smooth surface as well. Reducing or removal of the fluid shear applied, biofilms could regain only part of their original structure (Blauert et al., 2015;

Dreszer et al., 2014). Under oscillating flow conditions, the change of biofilm structure is expected. Under this condition, the incorporation of the viscoelastic behavior of biofilms would provide more insight into the interaction between biofilm structure and the hydrodynamics.

3.5   Conclusion

The method developed in this study provides the opportunity to combine detailed biofilm structure obtained from biofilm imaging at the meso-scale by means of OCT and biofilm modeling to enhance our understanding of fluid-structure interactions at micro-scale. Two real heterogeneous biofilm geometries were extracted from OCT images. Meanwhile a simplified geometry with same amount of biomass present but distinctively different biomass distribution was generated. A model with biofilm images as structural template was developed to incorporate hydrodynamics as well as biochemical conversion of substrates. The simulation results with different geometries revealed that:

- The method developed allowed detailed analysis of fluid-structure interaction at micro-scale and revealed that slight difference in biofilm structure can lead to significant difference in local hydrodynamics. It proved to be a promising method for biofilm research, especially when precise representation of biofilm structure is of critical importance.

- Depending on the flow conditions, the heterogeneous geometry may behave different from the smooth biofilms with respect to substrate boundary flux. Under the condition of pure diffusive mass transfer, rough biofilms appeared to show higher mass transfer flux due to the large liquid-biofilm interface providing more contact to substrates. Rough biofilms also resulted in higher mass transfer fluxes than smooth biofilms with enhanced mass transfer at biofilm surface under flow through conditions.

- The method can be extended by incorporating other types of imaging data containing information about biomass activity and/or microbial distribution.

Chapter 4

Visualization of the attachment of real wastewater particle fraction to biofilm surface and its effect on mass transfer

4.1 Introduction

A large part of COD in municipal waste water is associated with particulate organic matter (Levine et al., 1985; Tchobanoglous et al., 2003) that span a range from submicron to several hundred of microns. However, substrate uptake by bacteria is limited to molecules with a molecular weight less than $1000\,Da$ (Kommedal et al., 2006), which means the organic particles cannot be used by microorganism directly. In most waste water treatment systems, the removal of carbon and nutrients is limited by the hydrolysis of organic particles (Morgenroth et al., 2002). Many researches have focused on the hydrolysis of organic particles, which is defined as the sum of all the processes that make the particulate organic matter available for microbial growth (Gujer et al., 1999). Due to the complexity of organic particles contained in real waste water with respect to their chemical composition (Huang et al., 2010) and a broad range of particle size, model compounds with simplified composition and well-defined particle characteristics are often used to investigate the mechanism of hydrolysis as well as the interaction between particles and biofilms. The model compounds often used include bovine serum albumin (Confer and Logan, 1998), starch (Mosquera-Corral et al., 2003), dextran (Confer and Logan, 1998; Kommedal et al., 2006), soy protein (Mosquera-Corral et al., 2003) and egg protein (Dimock and Morgenroth, 2006). Confer and Logan (1998) used bovine serum albumin ($65,000\,amu$) and dextran (with an average M_W of 70000 (Sigma)) as model compounds to investigate protein and polysaccharide degradation, respectively. They speculated that the hydrolysis of macromolecules repeated a loop of cell-associated hydrolysis followed by

the release of hydrolytic fragments, which diffuse back into the bulk liquid until these fragments are small enough to be assimilated by cells (less than $1000\,Da$). Very low hydrolysis rate coefficients were determined by Eliosov and Argaman (1995) for both raw primary suspended solids (obtained by centrifuging the raw municipal waste water) and for non-settleable suspended solids in an activated sludge system. Using artificially produced protein particles from hard boiled eggs, Dimock and Morgenroth (2006) clearly showed with their particle break-up model that hydrolysis rates are influenced by the size of the organic particles. By incorporating the particle break-up process from big particles into small particles, the increase of the specific surface was captured, which successfully reproduced the respirometry results that are not included into the activated sludge models.

Boltz and La Motta (2007) suggested to divide the removal of organic particles in biofilm systems into four steps, presented in Figure 4.1: (1) transport of the particles to the biofilm surface, (2) attachment of particles, (3) hydrolysis of the particles, followed by the release of the hydrolytic products, and (4) biochemical reactions of the products. The aforementioned studies mostly focused on the latter two steps. So far the removal of dissolved substances is well understood. However, there is still a lack of knowledge on the transport of organic particles and the interaction between the organic particles and biofilms. Direct contact between bacteria and organic particles is a prerequisite for hydrolysis and their subsequent removal (Confer and Logan, 1998). In the theoretical study of Bouwer (1987), the authors separated the deposition of particles in biofilm system into two steps. Particles are firstly transported from the bulk liquid to the bulk-biofilm interface, which is a physical process governed by hydrodynamics. Then the particles attach to the biofilm surface, which is a chemical process depending on the properties of biofilm surface and the chemistry of surrounding solution. Using fluorescently labeled microbeads, Drury et al. (1993) demonstrated that the $1\,\mu m$ microbeads can readily penetrate biofilms. However, increasing particle size leads to reduced mass transport into biofilms, with large particles retained at the biofilm surface (Morgenroth et al., 2002; Confer and Logan, 1997; Carlson and Silverstein, 1998). Therefore, the removal of larger particles is more complicated. Boltz and La Motta (2007) described the attachment process as bioflocculation in which particles are entrapped through chemical bounding under the influence of extracellular polymers excreted by the bacteria in the biofilms at the biofilm surface. A first-order bioflocculation kinetic expression successfully described the removal of both organic and inorganic particles in a pilot-scale trickling filter independent of biofilm thickness (Boltz and La Motta, 2007). However, there has been no study so far visualizing the process of particle attachment onto biofilm surface.

The physiology and morphology of biofilms may be altered by the attachment of organic particles at the bulk-biofilm interface, thereby influencing the mass transfer of dissolved substances. With a lab-scale rotating drum reactor, Särner and Marklund (1985) concluded that the attachment of organic particles onto the biofilm surface imposed a negative influence on the removal of dissolved
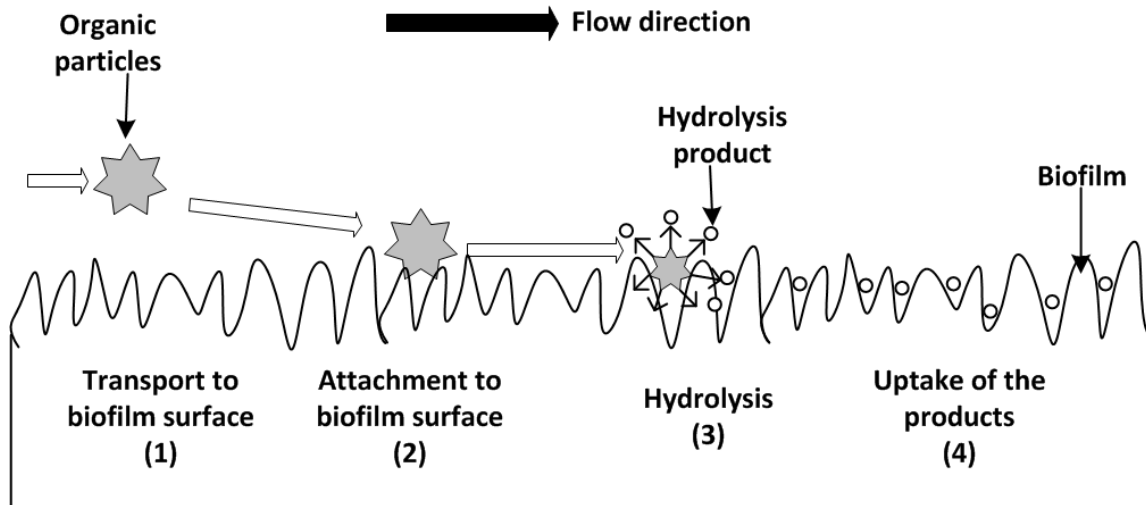
Figure 4.1: Schematic representation of the processes involved in the removal of organic particles in biofilm systems.

substances at high temperature and high glucose concentration. It was speculated that such a negative effect might be caused by a local oxygen shortage in the biofilm matrix as a result of the degradation of the organic particles attached (Särner, 1986). So far, there has been no experimental or modeling studies that examine the mechanism of this negative effect.

The objective of this study was to visualize the attachment of organic particles of different size fractions originated from raw waste water onto a biofilm surface with optical coherence tomography (OCT). The images obtained with and without particles attached were used further to simulate the hydrodynamics and to quantify its influence on mass transfer. Combined with imaging and 2D simulation, we aim to unveil the mechanism of reduced removal of dissolved substrate after the adsorption of organic particles on a biofilm surface.

4.2   Material and methods

4.2.1   Characterization of the organic particles in raw municipal waste water

Raw waste water served as the particle source and was collected after the grid chamber in the sewage plant in Neureut (Karlsruhe, Germany). Particle size classes were determined immediately in the lab. Raw waste water of $60 L$ was sieved. The particles were separated into five size fractions: $d_P \geq 500 \mu m$, $250 \leq d_P \leq 500 \mu m$, $100 \leq d_P \leq 250 \mu m$, $45 \leq d_P \leq 100 \mu m$ and $d_P \leq 45 \mu m$. Particle fractions were resuspended in tap water and stored at $4^o C$ before being used. Total suspended solids (TSS) and volatile suspended solids (VSS) were measured from the resuspension to determine the particle concentration in the raw waste water.

Densities of the different size fractions were quantified with an in-house made pycnometer. The measurements were conducted according to the procedure described in. The particles were firstly filtered to remove the bulk liquid. The particle densities (ρ_S) were calculated according to

$$\rho_s = \frac{m_2 - m_0}{(m_1 - m_0) - (m_3 - m_2)} \cdot \rho_w \tag{4.2.1}$$

where m_0 and m_1 are the mass of the empty pycnometer and the mass of the pycnometer filled with water, respectively. m_2 is the mass of the pycnometer filled with the drained particles to be determined. m_3 is the mass of the pycnometer filled with drained particles and water. ρ_w is the density of water.

4.2.2 Experimental procedure

The experiments of particle attachment onto the biofilm surface were conducted in a flume. The experimental setup is illustrated in Figure 4.2. The system consisted of a flume with dimension of $60 \times 8 \times 6.1\,cm^3$, a pump, the OCT (Thorlabs GmbH, Dachau, Germany) and a Biofilm Chip M (AnoxKaldnes) (shown in Chapter 1 Table 1.1) fully filled with biomass inside the carrier compartments. The volumetric flow rate was adjusted to $30\,mL \cdot s^{-1}$. The water depth in the flow cell was adjusted to $1\,cm$, which led to an average flow velocity of $5\,cm \cdot s^{-1}$. A weir was installed to achieve laminar flow conditions ($Re = 400$) in the flume. The bulk liquid contained $100\,mg \cdot L^{-1}$ COD (glucose) and nutrients with same composition used in Section 2.2.
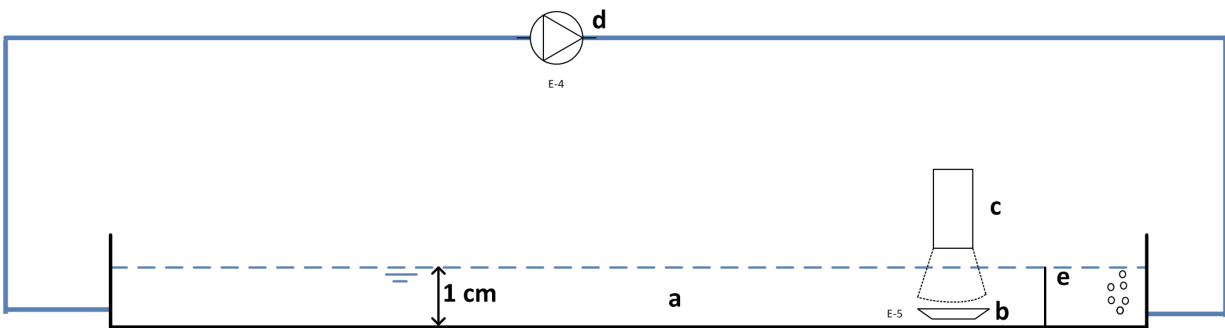
Figure 4.2: Schematic drawing of the experimental setup as seen from the side and composed of: a) flow cell, b) biofilm carrier, c) OCT, d) pump, e) a weir to stabilize the flow.

The carrier was placed $50\,cm$ away from the inlet so that laminar flow fully developed before reaching the carrier. Before any measurement, the system was aerated for $1\,h$ to achieve stable DO concentration. Before adding particles to the system, an OCT C-scan was acquired to serve as blank for the image analysis afterwards. The image was taken $2\,min$ after stopping the pump to obtain high quality images with no interference from the flow. Depending on the particle concentration in

the enriched particle solution, a certain volume of particle solution was added to the end of the flow cell to achieve particle concentration inside of the flow cell ten times the concentration of that size fraction in raw waste water. The high particle concentrations were chosen to enhance the effect of the particles on the biofilms, which otherwise would be difficult to observe if too few particles would attach and deposit on the biofilm surface.

After $1h$ of particle release, the carrier surface was covered with particles. An OCT image at the same position was taken. Afterwards the system was flushed with tap water to wash out the planktonic bacteria. The bulk liquid was filtered and the particles released back to the system. The system was then run in recirculation mode for $10h$. OCT image was obtained once more.

To quantify the thickness of the particle layer and to examine if the particle layer would be compressed by fluid shear induced by liquid flow, experiments were repeated. A similar imaging procedure was followed and OCT settings were kept constant. The only difference was that the images were taken $20min$, $1h$, $2h$, $3h$ and $4h$ after releasing the particles into the flow cell.

4.2.3   Image analysis

The general principle of image analysis in this experiment was to subtract the biofilm matrix before particle deposition from the images obtained afterwards. The procedure is described in Figure 4.3.

(a) The raw $3D$ images were firstly converted into $'8-bit'$ gray scale images.

(b) 'Brightness/Contrast' was manually adjusted to get rid of the background noise. As it is only the biofilm surface that is of importance for the quantification, the dynamic range was adjusted very narrow to emphasize the contrast at the biofilm surface. Because the imaging conditions were not exactly the same for the images from different experiments, the dynamic range was adjusted manually by checking the visual effect.

(c) The $3D$ images were then cropped to a size of $3.4 \times 3.4 \times 1.47\,mm^3$.

(d) Then followed by manual binarization. The same procedure was implemented for the images with and without particles.

(e) The 'Image calculator' function of Fiji 1.49 was employed to subtract the biomass and the plastic grid before particle deposition from the images after particle deposition. After this step, all the biomass was eliminated, with only the particles left.

(f) The 'Find connected regions...' plugin was used to find connected particles and remove the small isolated artifacts.

(g) In the end the volume of the particles was quantified with the plugin '$3D$ object counter' developed by Bolte and Cordelières (2006).
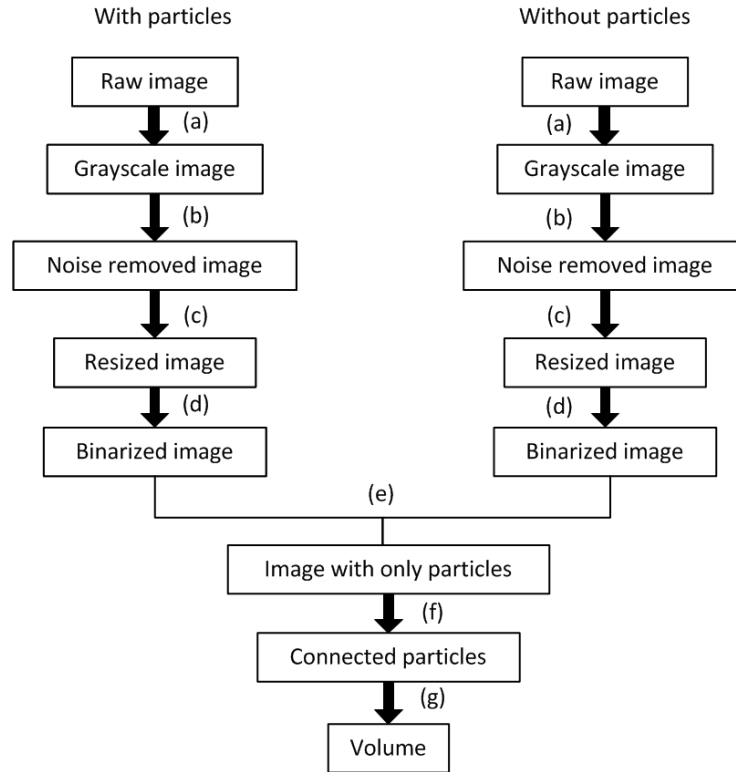
Figure 4.3: Scheme of the image processing procedure

For the calculation of the particle layer thickness, the images were also cropped to $3.4 \times 3.4 \times 1.47 \, mm^3$. The same thresholding procedure was followed. As the biofilms were fluffy with a large quantity of branches above the carrier surface, it was difficult to track the biofilm surface. Instead a reference plane was created above the carrier surface for images taken before and after particle release, which is referred to the thick, black line in Figure 4.4(a). At each pixel, the thickness above the plane was calculated. An average thickness, h_{no}, was derived by summing up all the thickness at each position above the plane and then averaging it over the plane. Similarly, the mean height above the reference plan including the particles and the biofilms, h_{with}, was calculated. Afterwards the average thickness of the particle layer $h_{particle}$ is derived according to:

$$h_{particle} = h_{with} - h_{no} \tag{4.2.2}$$

4.2.4   Model structure

In addition to the visualization of the particle deposition, the images obtained with and without particles were further employed to predict the influence of particle deposition on mass transfer. The same modeling approach developed in Chapter 3 was implemented with $2D$ images only.
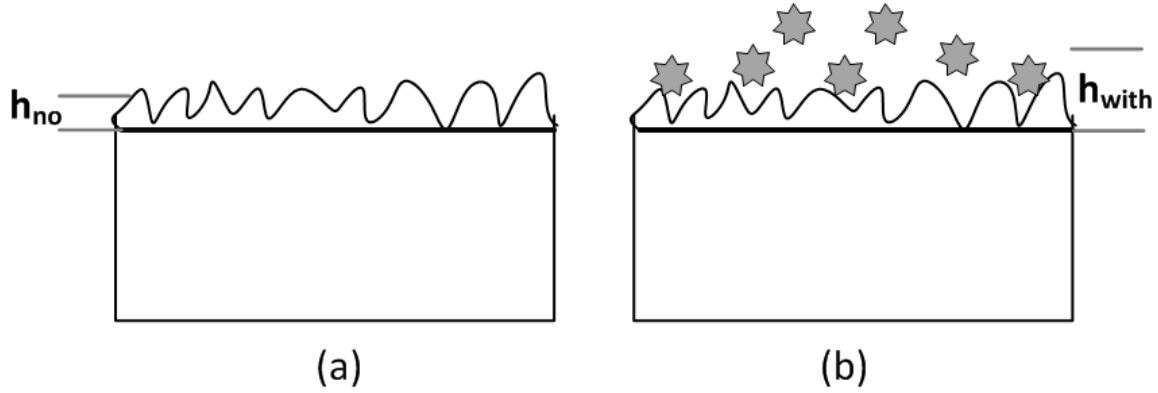
Figure 4.4: Schematic explanation for the calculation of particle layer thickness. The black thick lines indicates the reference plane created.

Therefore, one vertical slice was selected for each particle size fraction from the binarized OCT datasets with and without particles. Meanwhile for the dataset of the same particle size fraction, B-scans selected before and after adding particles were at the same position. In total six binarized images were chosen. All the vertical cross-sectional images had the same dimension of $3.4 \times 1.47 \, mm^2$. For the same size fraction, the particles were separated from the biofilm by subtracting the image without particles from the image with particles with the 'Image calculator' function of Fiji.

The binarized $2D$ images were transferred into COMSOL Multiphysics (COMSOL Inc., Sweden) with Matlab LiveLink as structural templates for the simulation with and without particles attached. A schematic drawing of the model structure is presented in Figure 4.5. The system included a bulk liquid domain, Ω_L, a domain designated to the particles, Ω_P, and a solid biofilm domain, Ω_B. The compartments were separated by the biofilm surface and the particle boundaries.

Fluid flow, mass transport and substrate conversion were incorporated into the model. Incompressible Navier-Stokes equations (Equation 4.2.3 and Equation 4.2.4) were solved to simulate the steady state laminar flow in Ω_L. Both biofilms and particles were assumed to be rigid and full of biomass (Picioreanu et al., 2000; Pavissich et al., 2014), with no liquid exchange among Ω_L, Ω_B and Ω_P. A fully developed velocity profile with an average inflow velocity of $5 \, cm \cdot s^{-1}$ parallel to the carrier surface was assigned at the inlet boundary. Zero pressure was assigned at the outlet boundary. Symmetrical boundary conditions were applied on the top boundary. No-slip wall conditions were applied both at the bulk-biofilm interface and the particle-liquid interface.

$$\rho(\mathbf{u} \cdot \nabla)\mathbf{u} = -\nabla P + \mu \nabla^2 \mathbf{u} \qquad (4.2.3)$$

$$\nabla \cdot \mathbf{u} = 0 \qquad (4.2.4)$$

where Equation 4.2.3 is the balance of inertial, pressure, viscous and viscoelastic forces; and Equation 4.2.4 is the continuity equation that describes the incompressibility-induced mass balance. $\mathbf{u}$
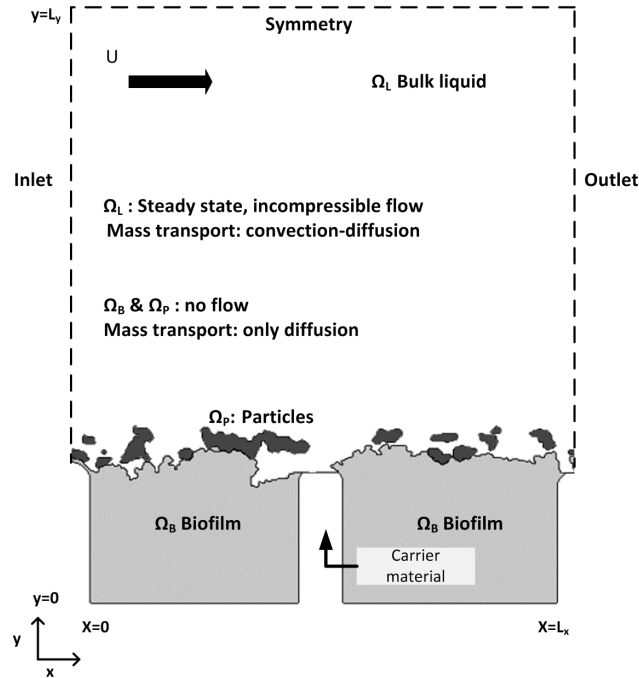
Figure 4.5: Conceptual structure of the model and the domain specifications. The simulation domain has a size of $3.4 \times 4.0\,mm^2$. The biofilm domain is shown in light gray color. The dark gray regions are occupied by the particles. The bulk liquid domain is shown in white color.

is the vector of the local liquid velocity. ρ is the liquid density. μ is the liquid dynamic viscosity and P is the pressure. It has to be emphasized that as only $2D$ cross-sectional images were used, it seems that some particles are not connect to the biofilm surface. They are actually connected to the biofilm surface at few slices before or after the slice selected according to the $3D$ images. Additionally, once attached to biofilm surface, the particles did not move or deform.

Transport of diluted species (COD and DO) were described with Equation 4.2.5.

$$\nabla \cdot (-D_i \nabla S_i) + \mathbf{u} \cdot \nabla S_i \;\; = \;\; r_i \qquad\qquad (4.2.5)$$

where D_i is the diffusion coefficient of substrate species i, S_i the concentration of diluted species i in the domain and r_i the turnover rate of substrate i. The diffusivity of substrates in both the biofilms and the organic particles reduced to 80% of that in the bulk liquid (Horn and Morgenroth, 2006; Stewart, 2003). In Ω_L convection and diffusion were solved. In Ω_B and Ω_P substrates were transported solely by diffusion. The continuity of flux and concentration of both diluted species at the bulk-biofilm interface was applied. *COD* and *DO* in the bulk liquid were measured to be $100\,mg \cdot L^{-1}$ and $7.5\,mg \cdot L^{-1}$, respectively. Substrate conversion was considered only in Ω_B. Conversion of *COD* and *DO* by heterotrophic bacteria was described by Monod kinetic (Henze, 2000), given in Equation 4.2.6 and Equation 4.2.7. The parameters are explained in Table 4.1. Growth and inactivation of microorganisms were not relevant for this study and thus not included

in the model. A biomass density of $500\,g \cdot m^{-3}$ was assigned evenly distributed in Ω_B.

$$r_{COD} = -\frac{1}{Y_H}\mu_H\left(\frac{S_{COD}}{K_{COD}+S_{COD}}\right)\left(\frac{S_{DO}}{K_{DO}+S_{DO}}\right)X_H \tag{4.2.6}$$

$$r_{DO} = -\frac{1-Y_H}{Y_H}\mu_H\left(\frac{S_{COD}}{K_{COD}+S_{COD}}\right)\left(\frac{S_{DO}}{K_{DO}+S_{DO}}\right)X_H \tag{4.2.7}$$

Table 4.1: Model parameters

Symbol	Value	Unit	Description	Reference
Y_H	0.67	$gCOD \cdot gCOD^{-1}$	Heterotrophic yield coefficient on substrate	Henze (2000)
μ_H	6	d^{-1}	Maximum specific growth rate of X_H	Henze (2000)
K_{COD}	20	$gCOD \cdot m^{-3}$	Half-saturation coefficient of X_H	Henze (2000)
K_{DO}	0.2	$gO_2 \cdot m^{-3}$	Half-saturation coefficient of X_H	Henze (2000)
D_{COD}	1.2×10^{-9}	$m^2 \cdot s^{-1}$	Diffusivity of COD in water	Picioreanu et al. (1997)
D_{O_2}	2.0×10^{-9}	$m^2 \cdot s^{-1}$	Diffusivity of O_2 in water	Picioreanu et al. (1997)

4.2.5   Evaluation of the results

The performance of the biofilms was compared with respect to the average oxygen flux into the biofilms. The local substrate flux was calculated according to

$$J_i = k_{L,i}(S_{i,0} - S_{i,\Gamma}) = -D_i\frac{\partial S_i}{\partial n}\Big|_\Gamma \tag{4.2.8}$$

where Γ denotes the bulk-biofilm interface. $k_{L,i}$ is the mass transfer coefficient for substance i. D_i is the diffusion coefficient of substance i. $\frac{\partial S_i}{\partial n}$ denotes the concentration gradients of substance i normal to the bulk-biofilm interface (Γ). The average oxygen flux was calculated by integrating the boundary flux J over the bulk-biofilm interface (Γ) and divided by the length of the two compartments L ($3.4\,mm$) according to Equation 4.2.9

$$\bar{J}_{O_2} = \frac{1}{L_\Gamma}\int_\Gamma J_{O_2} \cdot d\Gamma \tag{4.2.9}$$

Mass transfer is mostly characterized using the dimensionless Sherwood number (Sh), calculated according to Equation 4.2.10. The width of the simulation domain was chosen as the characteristic length for the calculation.

$$Sh \quad = \quad \frac{k_{L,i}L_h}{D_i} = \frac{-L_h \frac{\partial S_i}{\partial n}|_\Gamma}{(S_{i,0} - S_{i,\Gamma})} \tag{4.2.10}$$

However, when the total mass transfer is of concern, the spatially averaged Sherwood number $(\overline{Sh})$ is of more interest, which is calculated by averaging Equation 4.2.10 over the bulk-biofilm interface Γ:

$$\overline{Sh} \quad = \quad \frac{1}{L_\Gamma} \int_\Gamma Sh \cdot d\Gamma \tag{4.2.11}$$

For biofilms with a heterogeneous surface, the thickness of the concentration boundary layer (CBLT, δ_b, L_C in some literature) varies along the bulk-biofilm interface. For convenience the average CBLT $(\overline{\delta_b})$ was calculated substituting Equation 4.2.10 into Equation 4.2.8 and then average over the bulk-biofilm interface, which results in Equation 4.2.12. A qualitative comparison can be made between the cases with and without particle deposition.

$$\overline{\delta_b} \quad \cong \quad \frac{D_i}{\overline{k_{L,i}}} = \frac{L_h}{\overline{Sh}} \tag{4.2.12}$$

4.3   Results and discussion

4.3.1   Characteristics of the organic particles

Organic particles contribute to large amount of total COD in raw municipal waste water. Therefore, detailed characterization of the organic particles is required in order to better understand the behavior and the interaction between particles and biofilms. The results of particle size fraction in the raw waste water (after grit chamber) are presented in Table 4.2.

Table 4.2: Measurement of particle size, concentration and VSS/TSS ratio in raw municipal waste water

Class	Particle size (μm)	Concentration of TSS ($g \cdot L^{-1}$)	Fraction to TSS (%)	VSS/TSS ratio (%)	Density ($g \cdot L^{-1}$)
	raw WW	0.3326	–	94.6	
	$d_p \geq 500$	0.1392	41.8	–	
I	$250 \leq d_p < 500$	0.0299	9.0	99.7	1011 ± 10
II	$100 \leq d_p < 250$	0.0207	6.2	99.4	1071 ± 53
III	$45 \leq d_p < 100$	0.0307	9.2	99.2	1114 ± 44
	$d_p < 45$	0.1122	33.7	90.1	

According to Levine et al. (1991), the size distribution of particles in raw waste water is site specific. Based on the results of particle sieving, the concentration of the large fraction $d_P \geq 500\,\mu m$ and the small fraction $d_P < 45\,\mu m$ were about one third of the particle concentration quantified for raw waste water ($0.3326\,g \cdot L^{-1}$). The size fraction between 45 and $500\,\mu m$ accounted for 24.4% of total TSS loading. In the current study three size fractions of the particles were investigated in detail, namely $250 \leq d_P \leq 500\,\mu m$, $100 \leq d_P \leq 250\,\mu m$ and $45 \leq d_P \leq 100\,\mu m$. They will be referred to as particles class *I*, *II* and *III*, respectively.

The density of the three classes measured are provided in Table 4.2. The densities of all particle classes are higher than that of water. The particle class *III* had the highest density of $1114\,g \cdot L^{-1}$.

4.3.2   Visualization of the particles attached to the biofilm surface

OCT was used in this study to visualize particle deposition on the biofilm surface. Top view images before and after adding particles are presented in Figure 4.6. Cross sectional images before and after adding particles are given in Figure 4.7. See Figure 4.6(a) for the example of particle size class *I*, the biofilm surface appeared smooth and the plastic beams of the carrier can be seen clearly before adding the particles. One hour after adding particles, few particles (bright dots) were identified at the biofilm surface. After ten hours of particle circulation, more particles attached to the biofilm. The beams became less clearly visible, see Figure 4.6(c) . Similarly attachment of particles was observed with size class *II* and *III*. Comparing Figure 4.6(d) with (f) and (g) with (i), coverage of the carrier surface increased with decreasing particle size from class *I* to *III*. Comparing the images among the three particle size classes, filamentous particles were clearly visible for particle classes *I* and *II*. When the size of the particles reduced to $\leq 100\,\mu m$, the carrier surface became evenly covered with these fine particles.

A more clear view into the layer of attached particles is provided by a series of B-scans (*xz*-plane) in Figure 4.7. In Figure 4.7 (*b*), (*d*) and (*e*), the particles of all size fractions attached showed strong signals and appeared brighter than biofilm. A thin layer formed by the particles was clearly identified. For particle classes *I* and *II*, there are 'shadows' beneath the particles (Figure 4.7 (*b*) and (*d*)). This might be due to the particles blocked the signals backreflected from biofilm beneath, which further indicates that the particles are dense and reflect and absorb all the signals. For small particles of class *III* the optical signal could penetrate the particle layer.

For particle class *I*, only few big particles were present in Figure 4.7(*b*). The number of particles of class *II* attached largely increased, see Figure 4.7(*d*). Still individual particles were distinctly separated from each other. However, the small particles of class *III* touched each other and formed agglomerates. It was not possible to distinguish between individual particles (Figure

No particles	after 1h	after 10h

Particle I

Particle II
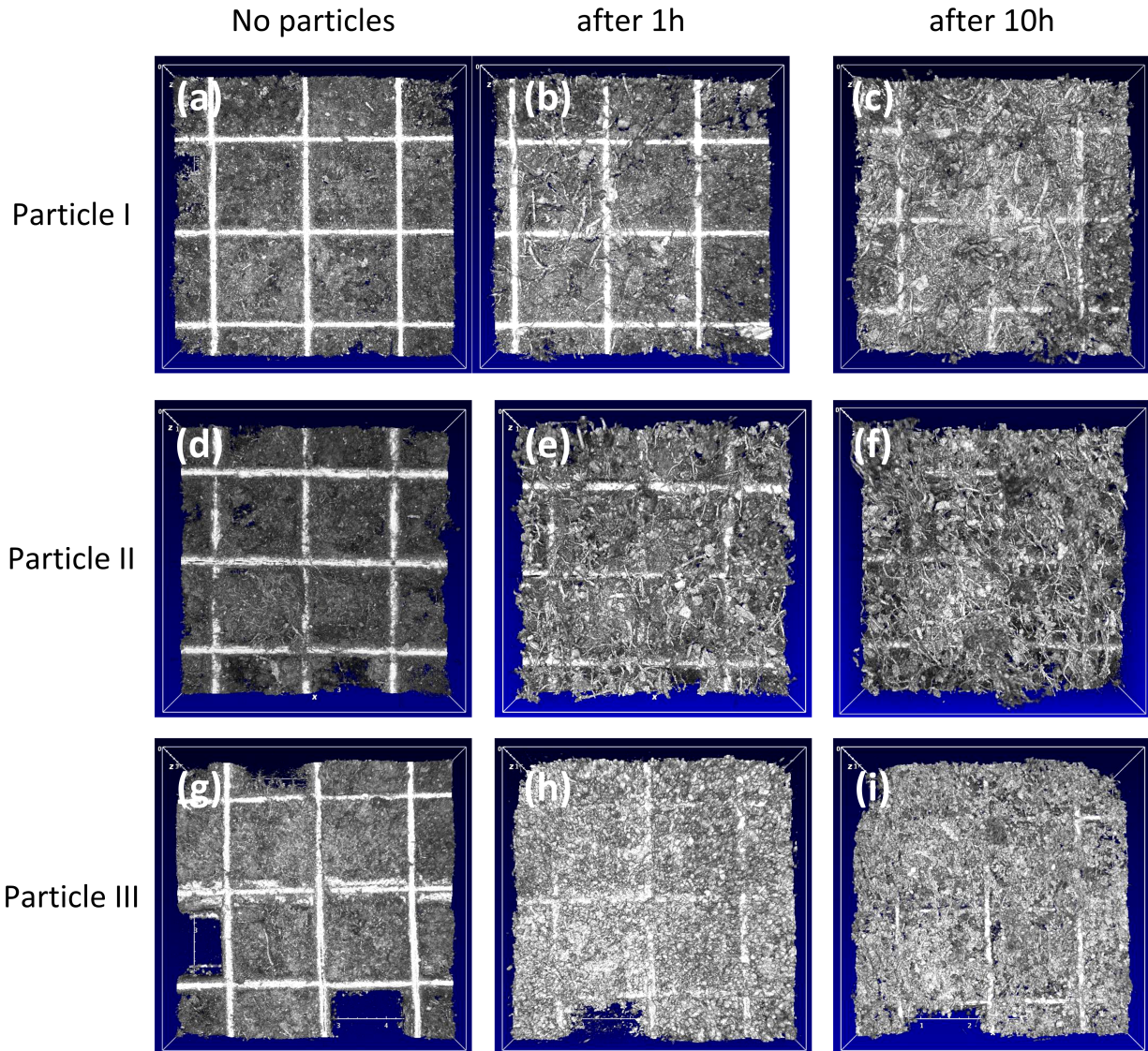
Particle III

Figure 4.6: OCT images showing the attachment of particles of different sizes on the biofilm surface from top view. (a), (d) and (g) are the images of biofilm before adding particles. (b), (e) and (h) show the deposition of particles after $1\,h$. (c), (f) and (i) are the images after $10\,h$ of particle addition. The images cover an area of $4 \times 4\,mm^2$ of carrier surface $(xy-plane)$.

4.7(f)). Therefore, it was difficult to count the number of particles attached. However, it was evident that the area covered by particles was significantly higher than that for particle classes I and II. Estimation of the amount of particles attached follows in 4.3.3.

Other differences lie in the gap between the particle layer and the biofilm surface. The big particles of class I are loosely attached to the biofilm surface, which can be seen in Figure 4.7(b) from the gap between the particles and the biofilm surface. With decreasing particle size, these gaps became narrower, and negligible for particles as small as class III, see Figure 4.7(f). It is speculated that the filamentous structures of the particles of classes I and II interact with the filaments at the biofilm

no particles   after 1h
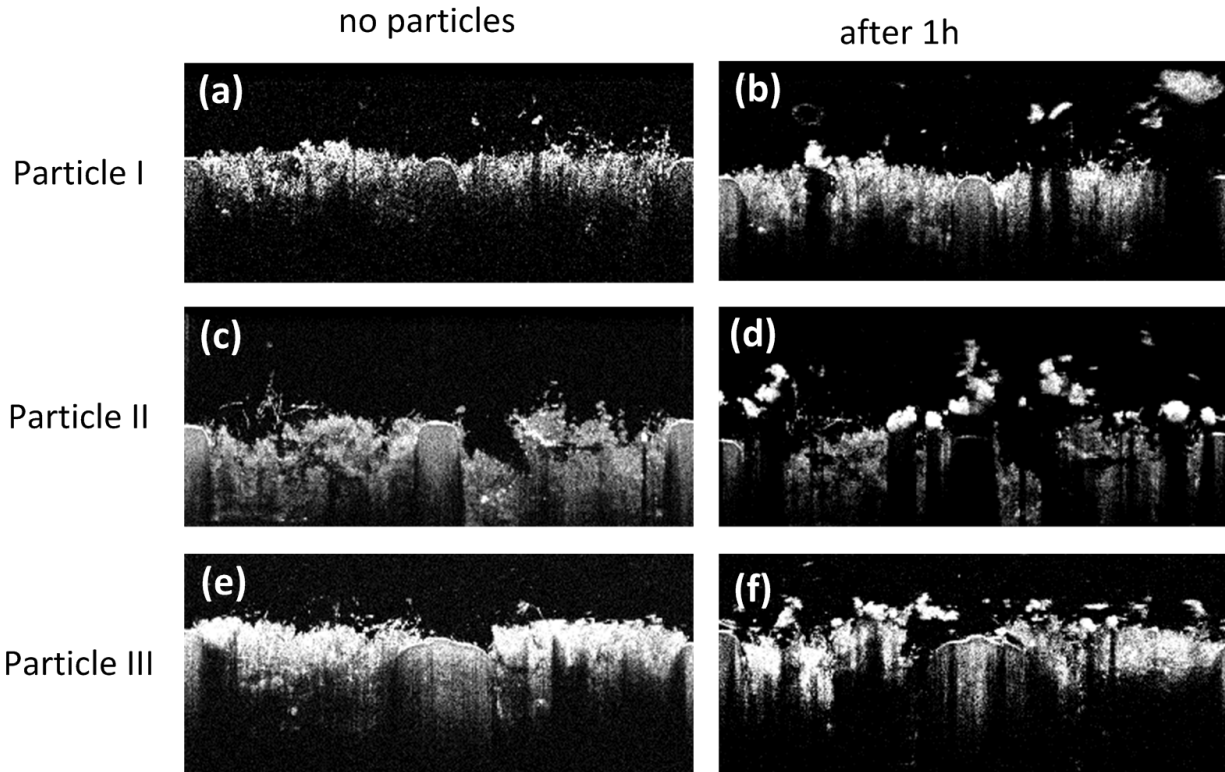
Figure 4.7: Visualization of particle attachment on biofilm surface from vertical cross-sectional view for different particle size fractions. Background is shown in black while the foreground is shown in gray scale for biomass, plastic and particles. (a), (c) and (e) are the images of biofilm structure without particles. (b), (d) and (e) are images showing the deposition of particles on the surface of biofilms $1h$ after adding particles. All the images have the same dimension of $3.4 \times 1.47 \, mm^2$.

surface, which prevented the particles to stick closer to the biofilm surface. The small particles of class *III* with more regular structure could probably readily migrate through the filaments at the biofilm surface and fill the spaces in between, thereby sticking closer to the biofilm surface. However, the particles were too big to penetrate into the biofilm matrix thereby retained on the biofilm surface.

4.3.3   Quantification of the particles attached

In addition to the qualitative visualization, particle attachment was further analyzed quantitatively with the plugin '3D *object counter*' (Bolte and Cordelières, 2006). The number and the volume of the particles attached were estimated. As described in 4.2.3, the particles were separated from the biofilm matrix by subtracting the biofilm matrix obtained without particles from the dataset with particle deposition. 3D reconstruction of the dataset containing the isolated particles deposited on the biofilm surface are presented in Figure 4.8. In addition to the 2D view in Figure 4.6, the

filamentous structure of organic particles was confirmed once more in the $3D$ view in Figure $4.8(a)$ and (b). While for particle class *III* in Figure $4.8(c)$, no filamentous structure could be observed and the particles stuck together and formed agglomerates.

Figure 4.8: $3D$ view of the isolated particles attached to the biofilm surface for the particle class of (a) *I* , (b) *II* and (c) *III*, respectively.

Table 4.3: Quantification of the particles attached on the biofilm surface

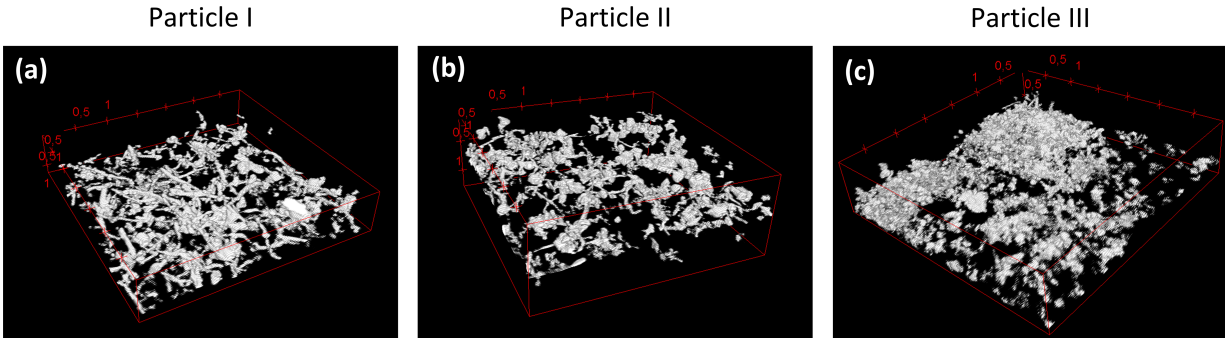| Property		*I*	*II*	*III*
Concentration in the flow cell	$(g \cdot l^{-1})$	0.116	0.094	0.129
Area for the calculation	(mm^2)	3.4×3.4	3.4×3.4	3.4×3.4
Total volume of particles	(mm^3)	0.17	0.2893	0.4679
Mean particle diameter	(μm)	375	175	72.5
Mean particle volume	$(\times 10^6 \mu m^3)$	28	2.8	0.2
Number of particles	$(-)$	5	103	2350

Quantification of the particle volume is provided in Table 4.3. Calculated over the same surface area and a similar particle concentration in the bulk liquid, the volume of the attached particle class *I* was $0.17\,mm^3$. The volume of the attached particle class *II* and *III* were almost twice and three times of that, respectively. To estimate the number of particles attached, the median diameter $(\overline{d_P})$ of the three particle classes were used, those are 375, 175 and $72.5\,\mu m$ for class *I*, *II* and *III*, respectively. Based on this assumption, the mean volume of the particles was calculated. And based on that the number of particles attached was derived. There was a significant difference in the number of particles attached among the three particle classes. Based on the calculation of using $\overline{d_P}$, there were only five particles of class *I* attached onto the biofilm surface. The number of class *II* particles increased two orders of magnitude to 103, while it increased further to 2350 for class *III*.

Although specific numbers are provided here, care shall be taken when interpreting them. Few aspects described here may lead to the inaccuracy in the counting results. First of all, as can be seen from Table 4.2, the density of all particle classes are higher than water. After being released into the flow cell, the particles settled partly before reaching the carriers. The big particles of class *I* settled faster than the other two size classes. While the smaller particles could be transported

further, thereby increasing the chance of interception with the rough biofilm surface as described by Bouwer (1987). Therefore there might be less attachment than possible for particle class *I*. The process of image analysis brought further inaccuracy. The biofilms used in the experiments were heterotrophic biofilms that are known for their fluffy surface. Although the biofilms were pretreated by rubbing two carriers against each other to remove the fluffy branches above the carrier surface, it was not possible to remove all of them. This made the subtracting process difficult. Therefore, the volume of particles attached might be overestimated. Nevertheless, the results provide qualitative and quantitative insights revealing that smaller particles attached more to the biofilm surface than the big particles.

The thickness of the particle layer was estimated according to the procedure described in Figure 4.4. For all the three particle classes, the results are presented in Figure 4.9. The large particles settled quickly at the biofilm surface already $20\,min$ after particle release. The thickness of the particle layer fluctuated throughout the experimental period. Referring to Figure 4.7(b) only few big particles attached to the biofilm surface, resulting in a strong variation of the mean thickness estimated. While for class *II* and *III*, the particles accumulated steadily over the biofilm surface, with increasing thickness of the particle layer. For class *II*, it seems that the particle layer reached a plateau with constant thickness of $160\,\mu m$ $2\,h$ after particle release. The particle layer thickness of class *III* increased dramatically, by more than 200% from $20\,min$ to $1\,h$ after particle release. Afterwards the rate of increase in thickness slowed down. It might be due to different time needed for the particles from big to small to settle. Till the end of the experiment, the particle layer thickness reached $100\,\mu m$.

Comparison of the particle layer thickness among the three particle size classes showed that class *II* had the highest mean thickness. Particles in class *III* attached slowly. In combination with Figure 4.7, the large gaps between the particles of class *I* and the biofilm surface increase the local thickness of the particle layer. With the method adopted for the thickness calculation, the large thickness was averaged out for class *I* due to the small number of particles attached, leading to thinner layer compared to class *II*. The gaps between the small particles of class *III* and the biofilm surface were very narrow. Thus the particle layer thickness was also thinner compared to class *II*.

4.3.4 The effect of particle deposition on mass transfer simulated

To investigate the influence of particle deposition at the biofilm surface on mass transfer of dissolved substrates, the images in Figure 4.7 were used as structural templates to model the hydrodynamics, biochemical activity and subsequent mass transfer characteristics. The flow field and oxygen concentration field are presented in Figure 4.10 and Figure 4.11, respectively. The maps of biomass activity with respect to oxygen consumption are attached in Figure A.3.
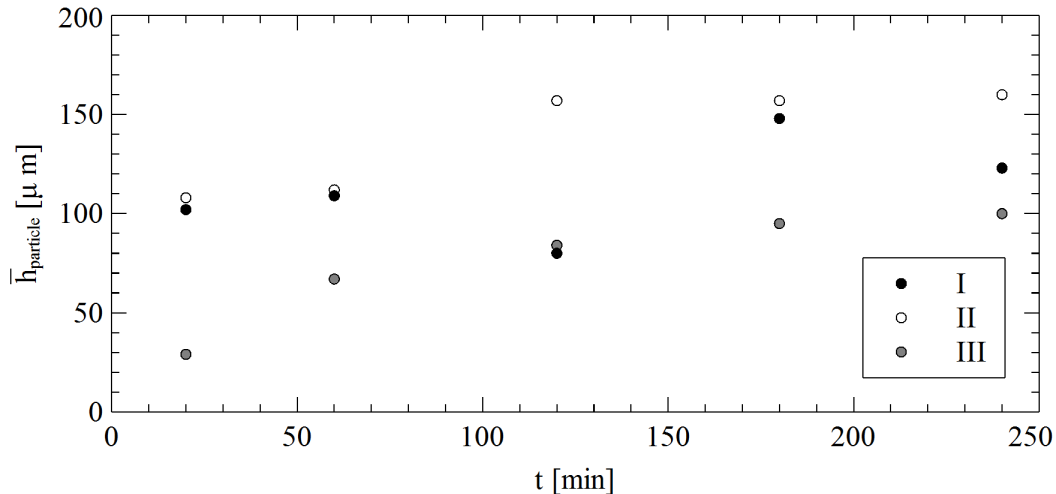
Figure 4.9: Estimation of the average particle layer thickness (μm) for all three particle classes

The presence of particles in Figure 4.10(b), (d) and (f) altered the flow field in the vicinity of the biofilm surface. Although quite small, those particles functioned as small obstacles and forced the local flow to change its pattern, which was revealed by the change of the flow lines. This influence was more pronounced in the substrate concentration field depicted in Figure 4.11. Under the same flow conditions simulated with inflow velocity of $5\,cm \cdot s^{-1}$, the concentration boundary layer (CBL) followed the biofilm surface closely when there was no particles attached, see Figure 4.11(a), (c) and (e). The presence of particles in Figure 4.11 (b), (d) and (e) modified the shape of the CBL. Visually it is clear that the CBL became thicker compared to their counterparts without particles for all particle classes. Quantification of the thickness of CBL will follow later.

Similar to the typical substrate concentration profiles often seen, the comparison between the concentration profiles before and after particle deposition at certain locations were plotted (shown in Figure 4.12). Profile lines along which the DO profiles are plotted are marked red in Figure 4.12(a), (c) and (e). To avoid the direct influence of the particles on the DO profiles, the profile lines were selected at locations that are free of particles. In Figure 4.12(b) and (f) for particle class I and III, the DO profiles after particle deposition shifted upwards, which implies that the CBL were pushed upwards also. On the contrary, the DO profile after particle deposition shifted slightly downwards in Figure 4.12(d) . Due to the residence of few particles on the left side of the profile line, small eddies developed in the downstream of the particles, which is depicted in Figure 4.11(d). The development of the small eddies improve the local mass transfer at that specific location, thereby leading to a compressed CBL. While at other locations in the case of class II, CBL seemed to be thicker compared to that without particles, see Figure 4.11(c) and (d).
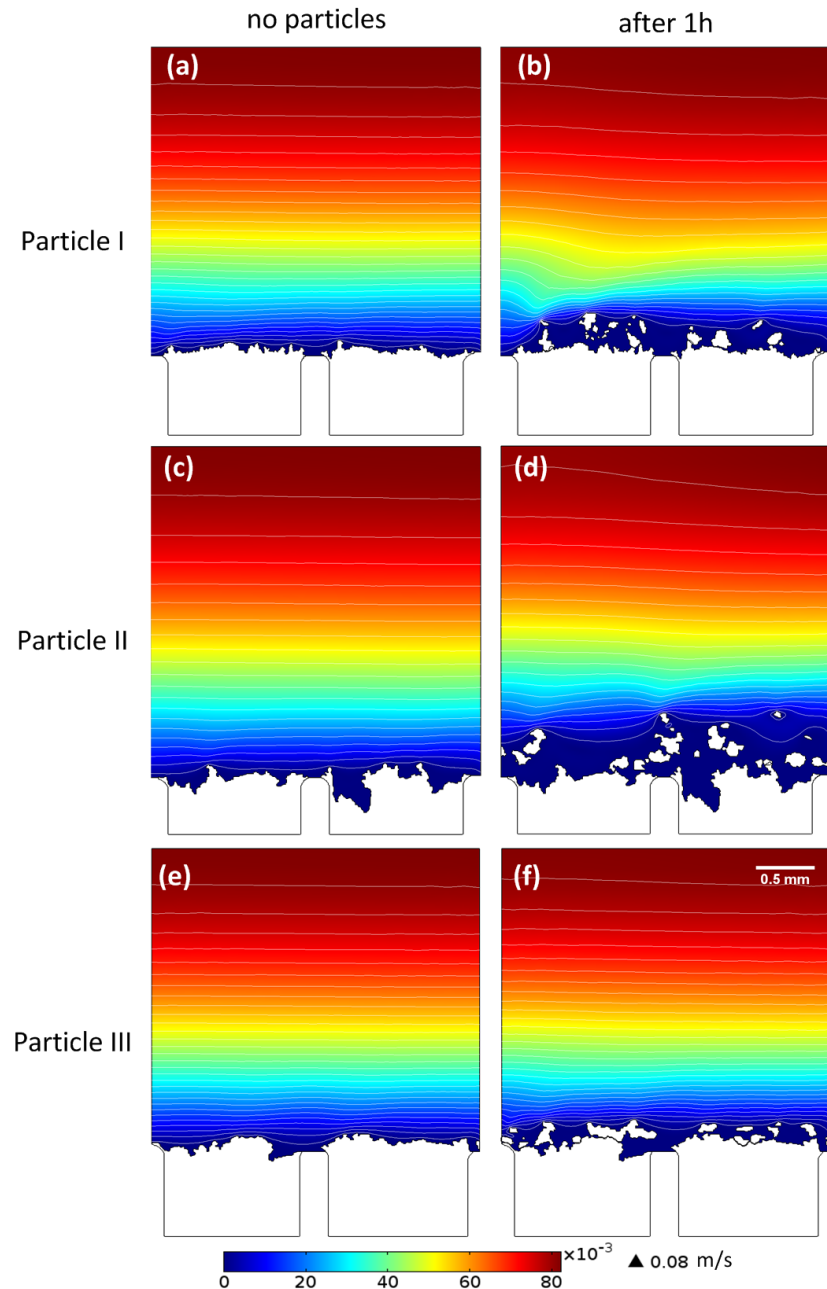
Figure 4.10: The effect of particle attachment on the local flow field for all the three particle size fractions. The white blocks at the bottom of the figures represent biofilm matrix. The small white blocks in the figures in the right column represent the particles attached. Stream lines are presented in white. The maximum flow velocity was $0.08\,m \cdot s^{-1}$.

To obtain a comprehensive understanding of the effect of particle deposition, biofilm activity with respect to oxygen flux entering the biofilm matrix was determined according to Equation 4.2.9. The results are provided in Table 4.4. For all the three particle classes, deposition of particles at the biofilm surface lead to reduction of oxygen fluxes. For class *I*, the few loosely attached par-
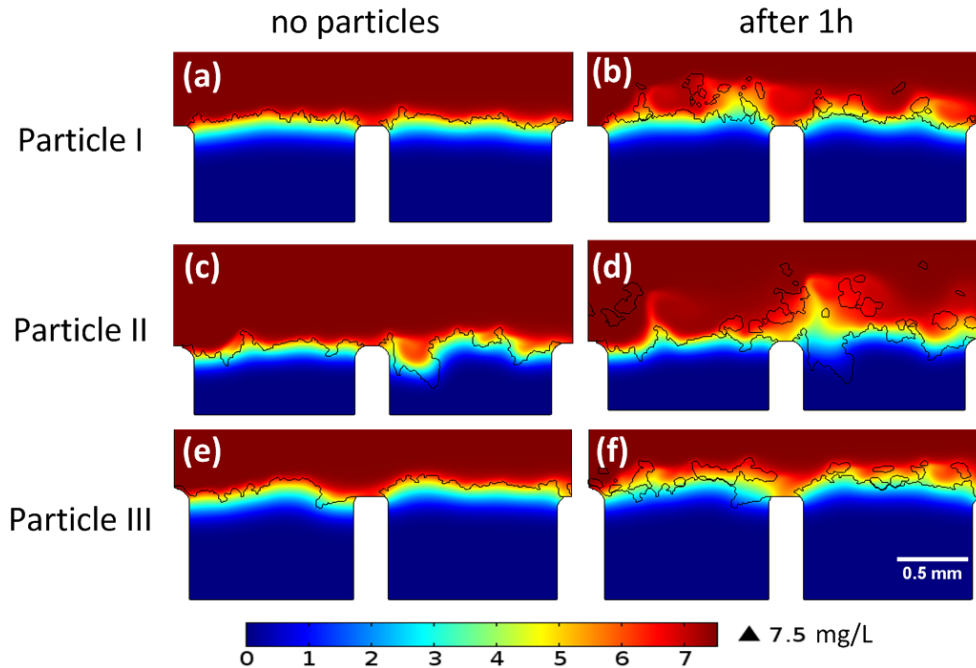
Figure 4.11: The oxygen concentration field $(mg \cdot L^{-1})$ simulated before and after particle attachment for all the three particle fractions. The color legend applies to all the figure. The oxygen concentration in the bulk is $7.5\,mg \cdot L^{-1}$. To get a closer look at the influence, the figures were cropped to view the biofilm and particles only.

ticles resulted in 12% reduction in DO flux. With decreasing particle sizes and closer attachment for class *II* and *III*, the reduction of DO fluxes increased to 18% and 21%, respectively. Särner (1981) and Särner and Marklund (1985) reported on the negative influence of particle adsorption at biofilm surface on dissolved substances in fixed-film reactors. Särner (1986) speculated that the degradation activity of the adsorbed particles caused a local oxygen shortage. However, according to our model, even without incorporating degradation by the particles attached, oxygen concentration at the biofilm surface is already lower after particles attachment than bare biofilms without particle, the results of which are plotted in Figure 4.13. For particle class *I*, the difference in DO concentration varied along the biofilm surface from left to right of the simulation domain. The large difference corresponds to the presence of particles and the stretches with no difference in DO concentration corresponds to the absence of particles. The stretches with overlap in DO concentration for class *II* also correspond to the gap between particles, in which small eddies developed and enhanced the local mass transfer. While for class *III* with a large portion of the biofilm surface covered by particles, there was no overlap of DO concentration along the whole biofilm surface. Although gaps exist among between particles, they were too narrow to form eddies. Therefore, DO concentration was always lower after particle attachment along the whole biofilm surface. It seemed that at similar particle concentration, smaller particles attach closer to the biofilm surface and had a higher coverage at the biofilm surface, thereby affecting mass transfer more.
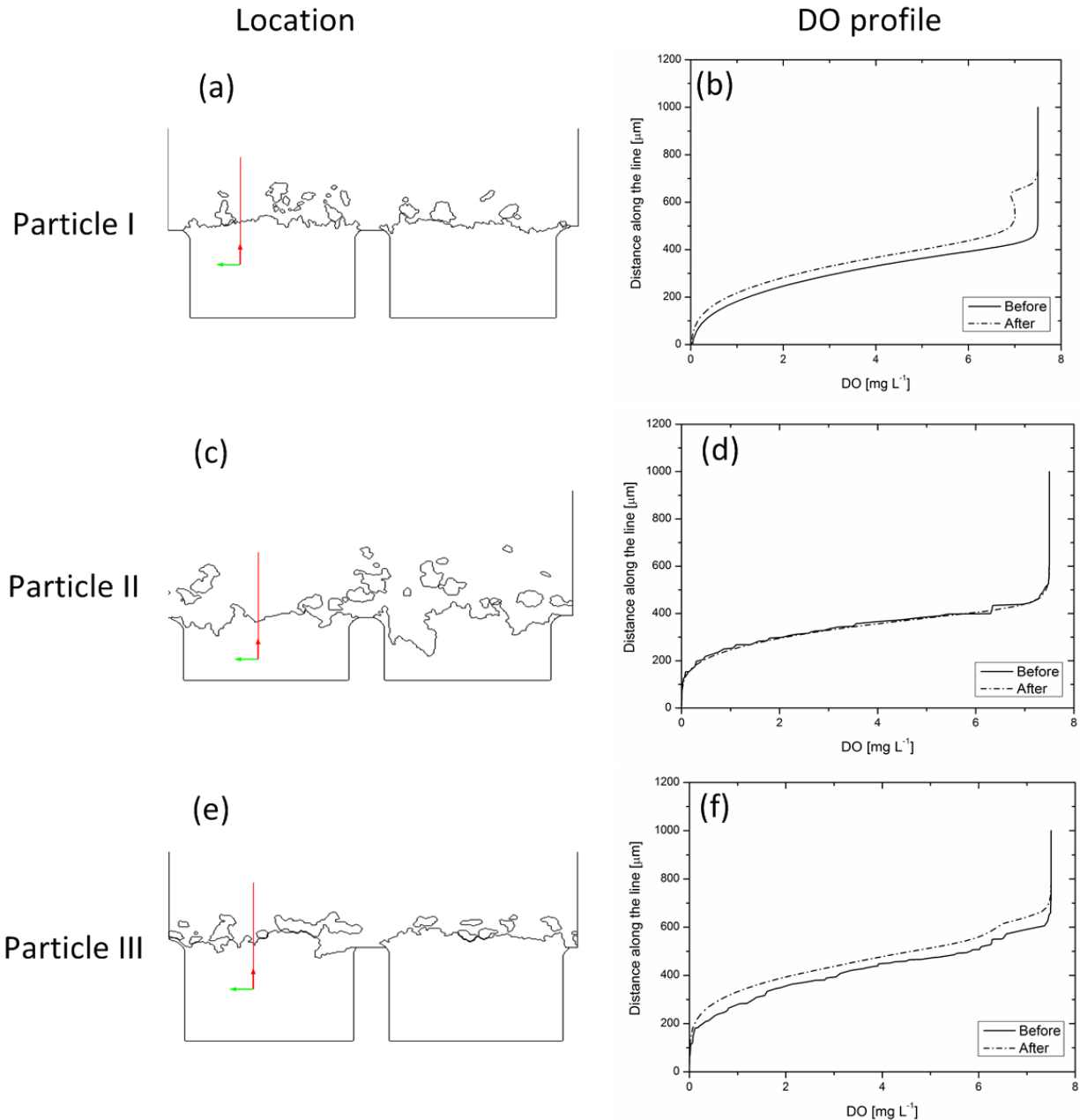
Figure 4.12: Simulated DO profiles along the profile lines before and after the attachment of particles. The profile lines are selected at locations without particles and marked red in (a), (c) and (e).

To understand the reason for the reduction of DO fluxes, the mass transfer characteristics in terms of $\overline{Sh}$ and $\overline{\delta_b}$ for the whole domain simulated were calculated according to Equation 4.2.11 and Equation 4.2.12. For all three particle classes studied, the deposition of particles on the biofilm surfaces resulted in lower $\overline{Sh}$ compared to their counterparts without particles, which implies that the presence of organic particles at the biofilm surface weakened mass transfer from the bulk liquid into the biofilm. A more straight forward comparison in terms of $\overline{\delta_b}$, presented in Table 4.4, clearly
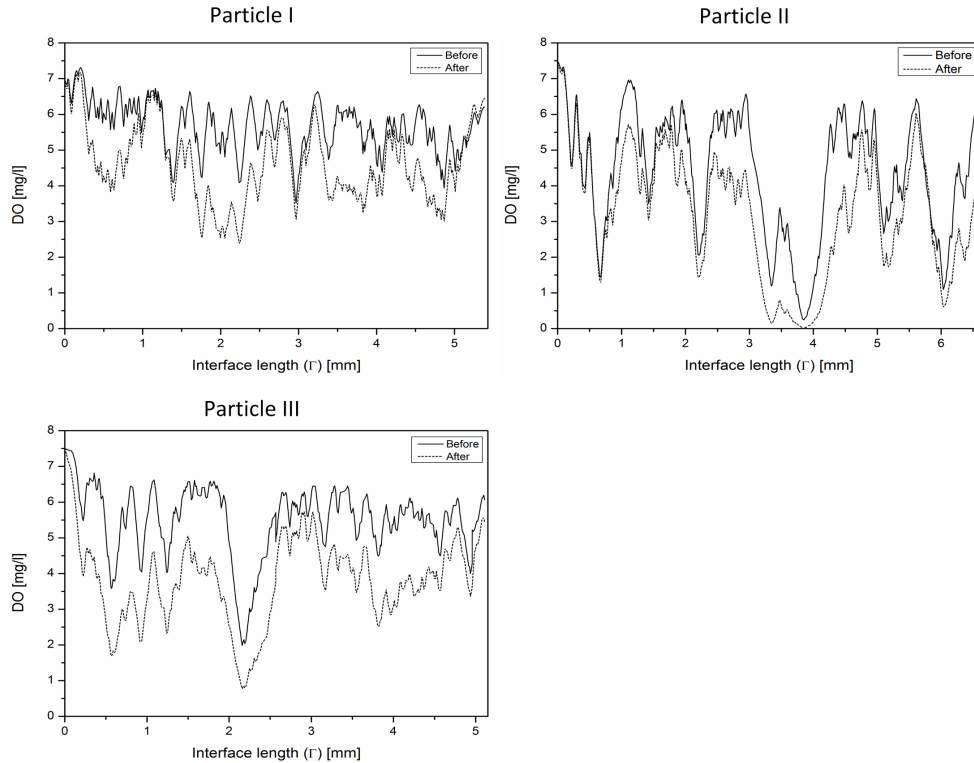
Figure 4.13: DO concentration along the biofilm surface before and after particle attachment for all three particle classes.

revealed that the CBL thickness increased dramatically (more than 60%) after the attachment of particles. Especially for class *III*, $\overline{\delta_b}$ increased by 120% from $68\,\mu m$ to $155\,\mu m$ after particle deposition. This means that the external mass transfer was weakened by more than half. The effect of this reduced mass transfer has direct influence on DO fluxes into biofilms, which implies the removal of substrates is expected to decrease too.

Table 4.4: The average DO flux simulated before and after the particle deposition.

Particle class	Interface Γ	DO flux			$\overline{Sh}$		$\overline{\delta_b}$		
		Before	After	Reduction	Before	After	Before	After	Increase
	(mm)	$(g \cdot m^{-2} \cdot d^{-1})$		$(\%)$	$(-)$			μm	
I	5.25	4.14	3.64	12	34.1	20.8	97	159	62
II	6.59	3.00	2.45	18	15.0	8.7	227	393	166
III	5.38	4.26	3.36	21	49.8	22.0	68	155	87

4.3.5   Potential improvement to the experiment and the model

In this study the experiments were conducted with carriers fixed at a certain position. While in real waste water treatment plants or MBBRs, with the constant movement of the carriers, the interaction

between particles and biofilms will be much more complex (Boltz and Daigger, 2010). Collision and/or abrasion, coarse bubble aeration may all lead to compression of particles deep into the biofilms, or on the contrary detachment of attached particles. Further research might be conducted by adding particles directly into MBBRs and observe the interaction between particles and biofilms under the conditions with constantly moving carriers and complex flow conditions.

In the model it seems the particles were not connected to the biofilm surface. However, they were bounded to biofilms in few slices before or after the slices selected. Calculation of the thickness of the particle layers also proved that under the conditions the experiments were conducted in the lab, the contact between the particles and the biofilms was strong enough for classes *II* and *III* to cope with the fluid shear and hold the particles at a fixed place without moving around. Therefore, the assumption of rigid structure of particles can be justified.

For simplification, it was assumed that the particles were inert with no active biomass attached. However, according to Ginestet et al. (2002), active biomass associated also to the particulate fraction in waste water. The partition of active biomass and its distribution on the particles were not investigated in the current study. For more accurate prediction of the influence of particle deposition on mass transfer, studies on the composition, partition of active biomass and its distribution over the particles shall be studied and incorporated as input into the model. Nevertheless, the model clearly reveals that the attachment of the particles onto biofilm surface hinders mass transfer from bulk liquid into biofilm.

4.3.6   Implication for engineering practice

As has been stated by Särner and Marklund (1985) and explained by the model results in the current study, the attachment of organic particles on the biofilm surface has negative effect on the removal of dissolved substances. If heavy loaded with particles at the biofilm surface, significant reduction in mass transfer from bulk liquid into biofilm can be expected, which will consequently lower the removal of dissolved substrates. In municipal waste water a large part of COD is associated to the organic particles of different particle sizes. Even though stated by Morgenroth et al. (2002) that particles smaller than $100\,\mu m$ can be removed by primary sedimentation to a large extent, there are still more than 28% of particles larger than $100\,\mu m$ in the primary effluent. These particles can quickly accumulate at the biofilm surface, thereby hindering the removal of dissolved substrates. Therefore, removal of particles prior to the biological treatment unit would lead to higher efficiency in the biological process, thereby to smaller treatment unit. Based on the estimation for a nitrifying activated sludge system by van Nieuwenhuijzen et al. (2004), 35% of the system volume can be reduced providing the removal of settable particles. There has been no study on the similar effect for biofilm system. Nevertheless similar effect in space saving can also be expected, providing the

mass transfer can be enhanced without the presence of a particle layer above the biofilm surface.

4.4   Conclusion

Organic particles of different size classes originated from municipal waste water were used to investigate the interaction between organic particles and biofilms developed on carriers from a lab scale MBBR. 3D volumetric images were acquired with OCT before and after particle attachment. With OCT, the attachment of organic particles of different sizes onto the biofilm surface was successfully visualized. The big particles attached sparsely and loosely to the biofilm surface. While a large amount of smaller particles covered more space and bonded closer to the biofilm surface. Furthermore, a 2D model was developed and employed the OCT images with biofilms and particles to serve as structural templates for the simulation of hydrodynamics, substrate transport and biochemical reaction. The combined approach allowed for a detailed analysis of the effect of particle attachment at biofilm surface. The results revealed that the attachment of organic particles onto the biofilm surface hindered mass transfer by up to 20%. The accumulation of particles at the biofilm surface affected the flow over biofilm surface and forced the concentration boundary layer to shift upwards, thereby weakening the mass transfer from bulk liquid into biofilms. Such negative impact shall be taken into account when designing biofilm based treatment systems.

Chapter 5

Conclusions and outlook

This work aimed at developing a method to combine the two major approaches in biofilm research, namely biofilm imaging and mathematical modeling. OCT was selected to monitor the biofilm structure development on biofilm carriers used in lab-scale MBBRs due to its advantages of label-free, *in situ*, fast image acquisition at the meso-scale. *2D* cross-sectional OCT images were incorporated into models considering the hydrodynamics, mass transport and biochemical conversion of substrates to assess the influence of biofilm surface roughness on mass transfer. The combined approach was further applied to visualize the attachment of organic particles originating from municipal waste water and to examine the effect of such attachment on mass transfer.

5.1 Biofilm structure development

Visualization of biofilm structure with different imaging techniques is an indispensable tool to study biofilms. In this work, OCT was for the first time employed to examine the structure development of biofilms grown on biofilm carriers used in lab-scale MBBRs. OCT images revealed that biofilms proceeded incrementally from carrier walls towards the center in a single compartment. Biofilms grew faster in the vertical center of the compartment and slower close to the top and bottom surfaces of the carrier, which led to the formation of a funnel-like biofilm structure with more biofilms in the vertical center of the compartment and less biomass at carrier surfaces. Comparison of the biofilms imaged (both *2D* and *3D*) at different spots on the same carrier unveiled the heterogeneous growth of biofilm with faster accumulation at the center of the carrier than that at the border. The biofilm structure quantified for both types of carriers through both *2D* and *3D* image analysis displayed the influence of carrier geometry on biofilm structure. The carrier with smaller compartment but higher protected surface area favored faster initial establishment of biofilms and the compartments were quickly filled. It took longer for biofilms to establish and to fill the compartments of the carrier with

larger compartment size. However, the final biofilm thickness, biomass volume and biofilm surface area after the carriers were filled were larger compared to those values of the carrier with smaller compartment size. Comparison of the biofilm development at different aeration rate revealed that biofilms grew faster for both types of carriers when low aeration was provided. Interestingly, compartment filling degree was also higher with low aeration rate on the cost of lower density.

Comparison of the results revealed a good correlation between the biofilm structure characteristics derived from $2D$ and $3D$ image analysis. The mean biofilm thickness and compartment filling degree obtained from $2D$ and $3D$ images were comparable before the carriers were fully filled with biofilms. This indicates that $2D$ imaging may replace $3D$ imaging to monitor the biofilm structure development. However, $3D$ images can provide more accurate description of biofilm structure which cannot be achieved by $2D$ imaging, such as biofilm distribution in the compartments, the highly heterogeneous surface morphology and the voids in biofilm matrix. The capability to image $3D$, *in situ*, non-invasive, fast and at the meso-scale renders OCT to be a powerful tool to obtain representative structural properties and for online monitoring of biofilm development.

5.2 The influence of biofilm surface roughness on mass transfer

A $2D$ biofilm model was developed to incorporate cross-sectional OCT image of biofilms grown on a carrier from a lab-scale MBBR as well as a simplified geometry. Three structures, two incorporated from OCT images and one simplified geometry, had the same amount of biomass available, but differed in terms of the liquid-biofilm interface length (L_Γ), surface enlargement factor (α) and surface roughness coefficient (R'_a). Hydrodynamics, transport and biochemical conversion of substrates were considered in the model. Detailed analysis of the hydrodynamics and substrate distribution was successfully simulated. Comparison of COD flux between the real heterogeneous geometry and the smooth geometry under different flow and DO concentrations revealed different response of biofilms to the variation of the environment conditions. Under the condition of liquid flowing parallel to the carrier surface, the real geometry with highly heterogeneous surface showed slightly higher COD removal at the inflow velocity lower than $0.1\,cm \cdot s^{-1}$. In the range of $0.1\,cm \cdot s^{-1}$ and $5\,cm \cdot s^{-1}$, the smooth structure achieved higher COD flux than the heterogeneous structure. Under the condition of liquid flowing through the compartments, the heterogeneous structure obtained mostly higher COD flux. Plot of the relative dominance of convective and diffusive mass transport unveiled that when diffusion dominated the region in the vicinity of biofilm surface, the heterogeneous structure could provide larger liquid-biofilm interface thus more contact to substrates. Based on the spatially averaged Sherwood number calculated at liquid-biofilm interface, the smooth geometry always experienced better mass transfer in the compartment. Simulation results of the two real geometries with slight difference in the length of liquid-biofilm interface and

surface roughness exhibited significant difference in local hydrodynamics. The increase of biofilm surface roughness led to increasing pressure drop, thus worse mass transfer due to more energy needed to compensate the friction loss at liquid-biofilm interface. Nevertheless, when the mass transfer was high enough so that the domain was dominated by convective transport, the heterogeneous biofilms displayed significantly higher COD boundary fluxes. The method incorporating biofilm imaging into biofilm modeling proved to be a promising approach to gain deeper understanding of biofilms.

5.3   The impact of particle attachment on mass transfer

Large amount of particulate organic matter is present in municipal waste water, which incorporate a considerable amount of COD. Removal of the organic particles in biofilm systems requires a sound understanding of the interaction between the particles and the biofilms. The approach of combining imaging with OCT and modeling developed in this study was further applied to investigate the effect of particle attachment onto biofilm surface on mass transfer. OCT was applied to visualize the attachment of organic particles of different size fractions originated from municipal waste water onto biofilm surface. From big to small, the particles were separated into three size fractions: $250 - 500\,\mu m$ (big), $100 - 250\,\mu m$ (medium) and $45 - 100\,\mu m$ (small). The experiment was conducted in a flume and with particle concentrations ten times of that in real waste water. Both top view and $2D$ cross-sectional images demonstrated the attachment of the organic particles at biofilm surface. Estimation of the particles attached showed only few big particles and significant increase of the number of particles attached with decreasing particle sizes. Further, the mean particle layer thickness fluctuated for the big particles, which implies reversible attachment of big particles. On the contrary the mean particle layer thickness increased incrementally for the medium and small particles. The model incorporated representative $2D$ cross-sectional images taken before and after particle attachment. Flow and substrate distribution before and after particle attachment showed significant difference. The presence of the organic particles at biofilm surface altered the flow field above biofilm surface. The DO concentration at biofilm surface was lowered after the deposition of particles. DO boundary flux was reduced by up to 20%. Around 50% reduction of the spatially averaged Sherwood number revealed that mass transfer at biofilm surface was hindered due to the attachment of particles. The concentration boundary layer was forced to shift towards the bulk liquid due to the accumulation of particles. Thus the concentration boundary layer became thick, which weakened the mass transfer from bulk liquid into biofilms.

5.4 Outlook

5.4.1 Potential improvement to the current study

During the early stage of biofilm growth on the carriers, OCT could penetrate the whole depth of the carriers ($1.05\,mm$) and obtained clear $3D$ images. With biofilm grew thicker and denser, OCT was not able to penetrate the whole depth. The images had to be taken from both sides and combined into one whole image stack, which lowered the image accuracy and significantly increased the time needed for image acquisition and workload for the image processing afterwards. Similar penetration limitation has also been reported. Mature biofilm thicker than $500\,\mu m$ could not be penetrated in Chen et al. (2012), in some studies even less (Derlon et al., 2012, 2013; Dreszer et al., 2014). To tackle this challenge, the enhanced depth imaging OCT used by Eroglu et al. (2015) and Li et al. (2015) may strengthen the penetration depth to reach deeper into the biofilm.

When imaging biofilm samples that are immersed in water, large amount of signals is reflected at air-water interface, which reduces the amount of energy reaching biofilm surface. The newly developed water immersible lens might be used to insert the lens into water phase, so that the energy loss at air-water interface can be reduced. This should be able to increase the imaging depth.

Another potential way to enhance imaging depth is to treat biofilms with optical clearing agents (OCAs), such as glycerol, polyethylene glycol, etc. The effect of using OCAs to obtain clearer and deeper images has been demonstrated by several studies with OCT in the field of medical research (Guo et al., 2011; Larina et al., 2008). The principle of optical clearing lies in matching the refractive index of biomaterial with extracellular fluid, thereby reducing light scattering (Zhu et al., 2013). As biofilms consist more than 90% of water, the mismatch of refractive index between water and the biomaterial leads to light attenuation, thus reducing the penetration depth of the incident light. Replacing the extracellular fluid (water) of biofilms with OCAs with high refractive index can narrow the mismatch of refractive index between biomaterial and water, thus reducing light scattering. Preliminary experiment showed significant increase from $630\,\mu m$ to $1000\,\mu m$ for compact anammox biofilm grown on carriers used in MBBR. However, further studies should be carried out to verify if the application of OCAs would have impact on the structure integrity and activity of biofilms.

In medical field, OCT has been applied to determine the diffusion coefficient of glucose (Ghosn et al., 2007) and permeability (Guo et al., 2011). Determination of the diffusion coefficient of certain species in biofilms may also be carried out with OCT based on the raw signals, which is fast then using the expensive and time consuming MRI (Ramanan et al., 2013).

The experiments with organic particles originated from municipal waste water were carried out

in a flow cell with the carrier fixed at a position. However, the interaction between the particles and biofilms would be more complex, due to the complex hydrodynamic conditions in the reactor with constant movement of the carriers. The particles may embed deeper into the biofilms or being detached from biofilm surface as a result of collision and/or abrasion between carriers and coarse bubble aeration. Further experiments may be conducted to observe the interaction closer to reality by adding organic particles directly into running MBBRs.

In the model developed for the investigation on the impact of particle attachment on biofilm surface, the organic particles were assumed to be inert for the first step with no presence of bacteria. Therefore, only the physical effect was simulated. However, according to Ginestet et al. (2002), active biomass also associate to the organic particles present in municipal waste water, varying in content depending on the particle size. Thereby the organic particles also contribute to the removal of soluble substrates. Studies on the composition, partition of the active biomass and its distribution over the particles shall be carried out and subsequently included into the model for more accurate simulation. Furthermore, the organic particles hydrolyze and release hydrolytic products, which can also be included into the model.

5.4.2   Potential applications of the combined approach

This work demonstrates the capability of the method to describe the micro-scale hydrodynamics in detail and facilitates the quantification of mass transfer characteristics. Although biofilm images on carriers used in MBBRs were used in the study, such an approach is not restricted to MBBRs. It can also be applied to membrane filtration system to investigate the impact of biofouling on membrane permeate flux and pressure drop. Blauert et al. (2015) investigated the time-resolved deformation of biofilms subjected to fluid shear stress using OCT and estimated the rheological properties of biofilms. The structures acquired in their study can be taken as structural template to impose mathematical description of the deformation, which would allow deeper mechanistic understanding of the deformation process.

Despite $2D$ gray scale OCT images were used in this study, the application of the method is not limited to OCT images only. Color images incorporating more information, such as FISH images, may also be used so that the microbial composition and distribution could be included into the model. The incorporation of more realistic and accurate microbial information can improve the accuracy of the relevant models. In addition to $2D$ images, $3D$ biofilm images could also be imported to serve as template, such as to investigate the mechanical properties of biofilms, which is difficult to be measured accurately.

Bibliography

Almstrand, R., Persson, F., Daims, H., Ekenberg, M., Christensson, M., Wilén, B.-M., Sörensson, F. and Hermansson, M. (2014). Three-dimensional stratification of bacterial biofilm populations in a moving bed biofilm reactor for nitritation-anammox. Int J Mol Sci *15*, 2191–2206.

Alpkvist, E., Bengtsson, J., Overgaard, N. C., Christensson, M. and Heyden, A. (2007). Simulation of nitrification of municipal wastewater in a Moving Bed™ biofilm process: a bottom-up approach based on a 2D-continuum model for growth and detachment. Water Sci Technol *55*, 247–255.

Alpkvist, E. and Klapper, I. (2007). A multidimensional multispecies continuum model for heterogeneous biofilm development. Bull Math Biol *69*, 765–789.

Alpkvist, E., Picioreanu, C., van Loosdrecht, M. C. and Heyden, A. (2006). Three-dimensional biofilm model with individual cells and continuum EPS matrix. Biotechnol Bioeng *94*, 961–979.

Andreottola, G., Foladori, P., Ragazzi, M. and Tatano, F. (2000). Experimental comparison between MBBR and activated sludge system for the treatment of municipal wastewater. Water Sci Technol *41*, 375–382.

Artyushkova, K., Cornejo, J. A., Ista, L. K., Babanova, S., Santoro, C., Atanassov, P. and Schuler, A. J. (2015). Relationship between surface chemistry, biofilm structure, and electron transfer in Shewanella anodes. Biointerphases *10*, 19013.

Bakke, R., Kommedal, R. and Kalvenes, S. (2001). Quantification of biofilm accumulation by an optical approach. Journal of Microbiological Methods *44*, 13–26.

Battin, T. J., Sloan, W. T., Kjelleberg, S., Daims, H., Head, I. M., Curtis, T. P. and Eberl, L. (2007). Microbial landscapes: new paths to biofilm research. Nat Rev Microbiol *5*, 76–81.

Beyenal, H., Lewandowski, Z. and Harkin, G. (2004). Quantifying biofilm structure: facts and fiction. Biofouling *20*, 1–23.

Biswas, K., Taylor, M. W. and Turner, S. J. (2014). Successional development of biofilms in moving bed biofilm reactor (MBBR) systems treating municipal wastewater. Appl Environ Microbiol *98*, 1429–1440.

Blauert, F., Horn, H. and Wagner, M. (2015). Time-resolved biofilm deformation measurements using optical coherence tomography. Biotechnol Bioeng *112*, 1893–1905.

Böhme, A., Risse-Buhl, U. and Küsel, K. (2009). Protists with different feeding modes change biofilm morphology. FEMS Microbiology Ecology *69*, 158–169.

Böl, M., Ehret, A. E., Bolea Albero, A., Hellriegel, J. and Krull, R. (2013). Recent advances in mechanical characterisation of biofilm and their significance for material modelling. Critical reviews in biotechnology *33*, 145–171.

Böl, M., Möhle, R. B., Haesner, M., Neu, T. R., Horn, H. and Krull, R. (2009). 3D finite element model of biofilm detachment using real biofilm structures from CLSM data. Biotechnol Bioeng *103*, 177–186.

Bolte, S. and Cordelières, F. P. (2006). A guided tour into subcellular colocalization analysis in light microscopy. Journal of microscopy *224*, 213–232.

Boltz, J. P. and Daigger, G. T. (2010). Uncertainty in bulk-liquid hydrodynamics and biofilm dynamics creates uncertainties in biofilm reactor design. Water Sci Technol *61*, 307.

Boltz, J. P. and La Motta, E. J. (2007). Kinetics of particulate organic matter removal as a response to bioflocculation in aerobic biofilm reactors. Water Environ Res *79*, 725–735.

Boltz, J. P., Morgenroth, E. and Sen. D. (2010). Mathematical modelling of biofilms and biofilm reactors for engineering design. Water Sci Technol *62*, 1821–1836.

Bouwer, E. J. (1987). Theoretical investigation of particle deposition in biofilm systems. Water Res *21*, 1489–1498.

Bridier, A., Le Coq, D., Dubois-Brissonnet, F., Thomas, V., Aymerich, S. and Briandet, R. (2011). The spatial architecture of Bacillus subtilis biofilms deciphered using a surface-associated model and in situ imaging. PloS one *6*, e16177.

Calderón, K., Martín-Pascual, J., Poyatos, J. M., Rodelas, B., González-Martínez, A. and González-López, J. (2012). Comparative analysis of the bacterial diversity in a lab-scale moving bed biofilm reactor (MBBR) applied to treat urban wastewater under different operational conditions. Bioresour Technol *121*, 119–126.

Cao, B., Majors, P. D., Ahmed, B., Renslow, R. S., Silvia, C. P., Shi, L., Kjelleberg, S., Fredrickson, J. K. and Beyenal, H. (2012). Biofilm shows spatially stratified metabolic responses to contaminant exposure. Environmental Microbiology *14*, 2901–2910.

Carlén, A., Nikdel, K., Wennerberg, A., Holmberg, K. and Olsson, J. (2001). Surface characteristics and in vitro biofilm formation on glass ionomer and composite resin. Biomaterials *22*, 481–487.

Carlson, G. and Silverstein, J. (1998). Effect of molecular size and charge on biofilm sorption of organic matter. Water Res *32*, 1580–1592.

Chambless, J. D. and Stewart, P. S. (2007). A three-dimensional computer model analysis of three hypothetical biofilm detachment mechanisms. Biotechnol Bioeng *97*, 1573–1584.

Chávez de Paz, Luis E, Lemos, J. A., Wickström, C. and Sedgley, C. M. (2012). Role of (p)ppGpp in biofilm formation by Enterococcus faecalis. Appl Environ Microbiol *78*, 1627–1630.

Chen, R., Rudney, J., Aparicio, C., Fok, A. and Jones, R. S. (2012). Quantifying dental biofilm growth using cross-polarization optical coherence tomography. Lett Appl Microbiol *54*, 537–542.

Confer, D. R. and Logan, B. E. (1997). Molecular weight distribution of hydrolysis products during biodegradation of model macromolecules in suspended and biofilm cultures I. Bovine serum albumin. Water Res *31*, 2127–2136.

Confer, D. R. and Logan, B. E. (1998). Location of protein and polysaccharide hydrolytic activity in suspended and biofilm wastewater cultures. Water Res *32*, 31–38.

Cunningham, A. B., Sharp, R. R., Hiebert, R. and James, G. (2003). Subsurface Biofilm Barriers for the Containment and Remediation of Contaminated Groundwater. Bioremediation Journal *7*, 151–164.

Davies, D. G. (1998). The Involvement of Cell-to-Cell Signals in the Development of a Bacterial Biofilm. Science *280*, 295–298.

de Beer, D., Stoodley, P. and Lewandowski, Z. (1996). Liquid flow and mass transport in heterogeneous biofilms. Water Res *30*, 2761–2765.

Derlon, N., Koch, N., Eugster, B., Posch, T., Pernthaler, J., Pronk, W. and Morgenroth, E. (2013). Activity of metazoa governs biofilm structure formation and enhances permeate flux during Gravity-Driven Membrane (GDM) filtration. Water Res *47*, 2085–2095.

Derlon, N., Peter-Varbanets, M., Scheidegger, A., Pronk, W. and Morgenroth, E. (2012). Predation influences the structure of biofilm developed on ultrafiltration membranes. Water Res *46*, 3323–3333.

Dimock, R. and Morgenroth, E. (2006). The influence of particle size on microbial hydrolysis of protein particles in activated sludge. Water Res *40*, 2064–2074.

Doube, M., Kłosowski, M. M., Arganda-Carreras, I., Cordelières, F. P., Dougherty, R. P., Jackson, J. S., Schmid, B., Hutchinson, J. R. and Shefelbine, S. J. (2010). BoneJ: Free and extensible bone image analysis in ImageJ. Bone *47*, 1076–1079.

Dreszer, C., Wexler, A. D., Drusová, S., Overdijk, T., Zwijnenburg, A., Flemming, H.-C., Kruithof, J. C. and Vrouwenvelder, J. S. (2014). In-situ biofilm characterization in membrane systems using Optical Coherence Tomography: Formation, structure, detachment and impact of flux change. Water Res *67*, 243–254.

Drexler, W. and Fujimoto, J. G. (2008). Optical coherence tomography: Technology and applications. Biological and medical physics, biomedical engineering, Springer, Berlin and New York.

Drury, W. J., Characklis, W. G. and Stewart, P. S. (1993). Interactions of 1 μm latex particles with pseudomonas aeruginosa biofilms. Water Res *27*, 1119–1126.

Eberl, H., Picioreanu, C., Heijnen, J. and van Loosdrecht, M. (2000). A three-dimensional numerical study on the correlation of spatial structure, hydrodynamic conditions, and mass transfer and conversion in biofilms. Chem Eng Sci *55*, 6209–6222.

Eberl, H. J., Parker, D. F. and van Loosdrecht, M. C. M. (2001). A new deterministic spatio-temporal continnum model for biofilm development. Journal of Theoretical Medicine *3*, 161–175.

Eldyasti, A., Nakhla, G. and Zhu, J. (2013). Impact of calcium on biofilm morphology, structure, detachment and performance in denitrifying fluidized bed bioreactors (DFBBRs). Chemical Engineering Journal *232*, 183–195.

Eliosov, B. and Argaman, Y. (1995). Hydrolysis of particulate organics in activated sludge systems. Water Res *29*, 155–163.

Eroglu, F. C., Asena, L., Simsek, C., Kal, A. and Yılmaz, G. (2015). Evaluation of choroidal thickness using enhanced depth imaging by spectral-domain optical coherence tomography in patients with pseudoexfoliation syndrome. Eye (London, England) *29*, 791–796.

Feng, Q., Wang, Y., Wang, T., Zheng, H., Chu, L., Zhang, C., Chen, H., Kong, X. and Xing, X.-H. (2012). Effects of packing rates of cubic-shaped polyurethane foam carriers on the microbial community and the removal of organics and nitrogen in moving bed biofilm reactors. Bioresour Technol *117*, 201–207.

Flemming, H.-C. and Wingender, J. (2010). The biofilm matrix. Nat Rev Micro *8*, 623–633.

Fu, B., Liao, X., Ding, L., Xu Ke and Ren, H. (2010). Microbial morphology and community structure in a suspended carrier biofilm reactor as a function of substrate loading rates. African Journal of Microbiology Research *4*, 2235–2242.

Ghosn, M. G., Tuchin, V. V. and Larin, K. V. (2007). Nondestructive quantification of analyte diffusion in cornea and sclera using optical coherence tomography. Invest Ophthalmol Vis Sci *48*, 2726–2733.

Ginestet, P., Maisonnier, A. and Spérandio, M. (2002). Wastewater COD characterization: biodegradability of physico-chemical fractions. Water Sci Technol *45*, 89–97.

Gjaltema, A., Arts, P. A., van Loosdrecht, M. C., Kuenen, J. G. and Heijnen, J. J. (1994). Heterogeneity of biofilms in rotating annular reactors: Occurrence, structure, and consequences. Biotechnol Bioeng *44*, 194–204.

Gjersing, E. L., Codd, S. L., Seymour, J. D. and Stewart, P. S. (2005). Magnetic resonance microscopy analysis of advective transport in a biofilm reactor. Biotechnol Bioeng *89*, 822–834.

Goode, C. and Allen, D. G. (2011). Effect of Calcium on Moving-Bed Biofilm Reactor Biofilms. Water Environ Res *83*, 220–232.

Gu, Q., Sun, T., Wu, G., Li, M. and Qiu, W. (2014). Influence of carrier filling ratio on the performance of moving bed biofilm reactor in treating coking wastewater. Bioresour Technol *166*, 72–78.

Gujer, W., Henze, M., Mino, T. and van Loosdrecht, M. C. M. (1999). Activated sludge model No. 3. Water Sci Technol *39*, 183–193.

Guo, X., Guo, Z., Wei, H., Yang, H., He, Y., Xie, S., Wu, G., Deng, X., Zhao, Q. and Li, L. (2011). In vivo comparison of the optical clearing efficacy of optical clearing agents in human skin by quantifying permeability using optical coherence tomography. Photochem Photobiol *87*, 734–740.

Habimana, O., Heir, E., Langsrud, S., Asli, A. W. and Møretrø, T. (2010). Enhanced surface colonization by Escherichia coli O157:H7 in biofilms formed by an Acinetobacter calcoaceticus isolate from meat-processing environments. Appl Environ Microbiol *76*, 4557–4559.

Haisch, C. and Niessner, R. (2007). Visualisation of transient processes in biofilms by optical coherence tomography. Water Res *41*, 2467–2472.

Haralick, R. M., Shanmugam, K. and Dinstein, I. (1973). Textural Features for Image Classification. IEEE Transactions on Systems, Man, and Cybernetics *3*, 610–621.

Heijnen, J. J., van Loosdrecht, M. C. M., Mulder, A. and Tijhuis, L. (1992). Formation of biofilms in a biofilm air-lift suspension reactor. Water Sci Technol *26*, 647–654.

Henze, M. (2000). Activated sludge models ASM1, ASM2, ASM2d and ASM3. IWA Pub., London.

Herrling, M. P., Guthausen, G., Wagner, M., Lackner, S. and Horn, H. (2014). Determining the flow regime in a biofilm carrier by means of magnetic resonance imaging. Biotechnol Bioeng *112*, 1023–1032.

Heydorn, A., Nielsen, A. T., Hentzer, M., Sternberg, C., Givskov, M., Ersbøll, B. K. and Molin, S. (2000). Quantification of biofilm structures by the novel computer program COMSTAT. Microbiology *146 (Pt 10)*, 2395–2407.

Horn, H. and Lackner, S. (2014). Modeling of biofilm systems: a review. Advances in biochemical engineering/biotechnology *146*, 53–76.

Horn, H. and Morgenroth, E. (2006). Transport of oxygen, sodium chloride, and sodium nitrate in biofilms. Chem Eng Sci *61*, 1347–1356.

Horn, H., Reiff, H. and Morgenroth, E. (2003). Simulation of growth and detachment in biofilm systems under defined hydrodynamic conditions. Biotechnol Bioeng *81*, 607–617.

Huang, D., Swanson, E., Lin, C., Schuman, J., Stinson, W., Chang, W., Hee, M., Flotte, T., Gregory, K. and Puliafito, C. (1991). Optical coherence tomography. Science *254*, 1178–1181.

Huang, J. and Pinder, K. L. (1995). Effects of calcium on development of anaerobic acidogenic biofilms. Biotechnol Bioeng *45*, 212–218.

Huang, M.-h., Li, Y.-m. and Gu, G.-w. (2010). Chemical composition of organic matters in domestic wastewater. Desalination *262*, 36–42.

Ivleva, N. P., Wagner, M., Horn, H., Niessner, R. and Haisch, C. (2009). Towards a nondestructive chemical characterization of biofilm matrix by Raman microscopy. Anal Bioanal Chem *393*, 197–206.

Janjaroen, D., Ling, F., Monroy, G., Derlon, N., Mogenroth, E., Boppart, S. A., Liu, W.-T. and Nguyen, T. H. (2013). Roles of ionic strength and biofilm roughness on adhesion kinetics of Escherichia coli onto groundwater biofilm grown on PVC surfaces. Water Res *47*, 2531–2542.

Kievit, T. R. d. (2009). Quorum sensing in Pseudomonas aeruginosa biofilms. Environmental Microbiology *11*, 279–288.

Klapper, I. and Dockery, J. (2002). Finger Formation in Biofilm Layers. SIAM J Appl Math *62*, 853–869.

Klapper, I. and Dockery, J. (2010). Mathematical description of microbial biofilms. SIAM Rev *52*, 221.

Klausen, M., Aaes-Jørgensen, A., Molin, S. and Tolker-Nielsen, T. (2003). Involvement of bacterial migration in the development of complex multicellular structures in Pseudomonas aeruginosa biofilms. Molecular Microbiology *50*, 61–68.

Kodach, V. M., Kalkman, J., Faber, D. J. and van Leeuwen, T. G. (2010). Quantitative comparison of the OCT imaging depth at 1300 nm and 1600 nm. Biomedical optics express *1*, 176–185.

Kommedal, R., Milferstedt, K., Bakke, R. and Morgenroth, E. (2006). Effects of initial molecular weight on removal rate of dextran in biofilms. Water Res *40*, 1795–1804.

Kreft, J. and Wimpenny, J. (2001). Effect of EPS on biofilm structure and function as revealed by an individual-based model of biofilm growth. Water Sci Technol *43*, 135–141.

Kreft, J. U., Picioreanu, C., Wimpenny, J. W. and van, Loosdrecht, M.C.M. (2001). Individual-based modelling of biofilms. Microbiology *147*, 2897–2912.

Lardon, L. A., Merkey, B. V., Martins, S., Dötsch, A., Picioreanu, C., Kreft, J.-U. and Smets, B. F. (2011). iDynoMiCS: next-generation individual-based modelling of biofilms. Environmental Microbiology *13*, 2416–2434.

Larina, I. V., Carbajal, E. F., Tuchin, V. V., Dickinson, M. E. and Larin, K. V. (2008). Enhanced OCT imaging of embryonic tissue with optical clearing. Laser Phys Lett *5*, 476–479.

Laspidou, C. S. (2014). Erosion probability for biofilm modeling: Analysis of trends. Desalination and Water Treatment *52*, 6342–6347.

Laspidou, C. S., Kungolos, A. and Samaras, P. (2010). Cellular-automata and individual-based approaches for the modeling of biofilm structures: Pros and cons. Desalination *250*, 390–394.

Laspidou, C. S. and Rittmann, B. E. (2004a). Evaluating trends in biofilm density using the UM-CCA model. Water Res *38*, 3362–3372.

Laspidou, C. S. and Rittmann, B. E. (2004b). Modeling the development of biofilm density including active bacteria, inert biomass, and extracellular polymeric substances. Water Res *38*, 3349–3361.

Lawrence, J. R. and Neu, T. R. (1999). Confocal laser scanning microscopy for analysis of microbial biofilms. In Biofilms vol. 310, of Methods in Enzymology pp. 131–144. Elsevier.

Levine, A. D., Tchobanoglous, G. and Asano, T. (1985). Characterization of the Size Distribution of Contaminants in Wastewater: Treatment and Reuse Implications. Journal (Water Pollution Control Federation) *57*, 805–816.

Levine, A. D., Tchobanoglous, G. and Asano, T. (1991). Size distributions of particulate contaminants in wastewater and their impact on treatability. Water Res *25*, 911–922.

Levstek, M. and Plazl, I. (2009). Influence of carrier type on nitrification in the moving-bed biofilm process. Water Sci Technol *59*, 875–882.

Lewandowski, Z. and Walser, G., eds (1991). Influence of hydrodynamics on biofilm accumulation EE Div/ASCE. American Society of Civil Engineers.

Lewandowski, Z., Webb, D., Hamilton, M. and Harkin, G. (1999). Quantifying biofilm structure. Water Sci Technol *39*, 71–76.

Li, Z., Wang, W., Zhou, M., Huang, W., Chen, S., Li, X., Gao, X., Wang, J., Du, S. and Zhang, X. (2015). Enhanced depth imaging-optical coherence tomography of the choroid in moderate and severe primary angle-closure glaucoma. Acta ophthalmologica *93*, e349–55.

Liu, Y. and Tay, J.-H. (2002). The essential role of hydrodynamic shear force in the formation of biofilm and granular sludge. Water Res *36*, 1653–1665.

Manz, B., Volke, F., Goll, D. and Horn, H. (2003). Measuring local flow velocities and biofilm structure in biofilm systems with Magnetic Resonance Imaging (MRI). Biotechnol Bioeng *84*, 424–432.

Melo, L. F. (2005). Biofilm physical structure, internal diffusivity and tortuosity. Water Sci Technol *52*, 77–84.

Milferstedt, K., Pons, M.-N. and Morgenroth, E. (2006). Optical method for long-term and large-scale monitoring of spatial biofilm development. Biotechnol Bioeng *94*, 773–782.

Milferstedt, K., Pons, M.-N. and Morgenroth, E. (2008). Textural fingerprints: a comprehensive descriptor for biofilm structure development. Biotechnol Bioeng *100*, 889–901.

Milferstedt, K., Pons, M.-N. and Morgenroth, E. (2009). Analyzing characteristic length scales in biofilm structures. Biotechnol Bioeng *102*, 368–379.

Milferstedt, K., Santa-Catalina, G., Godon, J.-J., Escudié, R. and Bernet, N. (2013). Disturbance frequency determines morphology and community development in multi-species biofilm at the landscape scale. PloS one *8*, e80692.

Morgenroth, E., Kommedal, R. and Harremoës, P. (2002). Processes and modeling of hydrolysis of particulate organic matter in aerobic wastewater treatment–a review. Water Sci Technol *45*, 25–40.

Morgenroth, E. and Milferstedt, K. (2009). Biofilm engineering: linking biofilm development at different length and time scales. Rev Environ Sci Biotechnol *8*, 203–208.

Mosquera-Corral, A., Montràs, A., Heijnen, J. and van Loosdrecht, M. (2003). Degradation of polymers in a biofilm airlift suspension reactor. Water Res *37*, 485–492.

Murga, R., Stewart, P. S. and Daly, D. (1995). Quantitative analysis of biofilm thickness variability. Biotechnol Bioeng *45*, 503–510.

Neu, T. R., Manz, B., Volke, F., Dynes, J. J., Hitchcock, A. P. and Lawrence, J. R. (2010). Advanced imaging techniques for assessment of structure, composition and function in biofilm systems. FEMS Microbiology Ecology *72*, 1–21.

Nogueira, B. L., Pérez, J., van Loosdrecht, Mark C M, Secchi, A. R., Dezotti, M. and Biscaia, E. C. (2015). Determination of the external mass transfer coefficient and influence of mixing intensity in moving bed biofilm reactors for wastewater treatment. Water Res *80*, 90–98.

Ødegaard, H. (2006). Innovations in wastewater treatment: –the moving bed biofilm process. Water Sci Technol *53*, 17.

Ødegaard, H., Rusten, B. and Westrum, T. (1994). A new moving bed biofilm reactor - applications and results. Water Sci Technol *29*, 157–165.

Patel, A., Nakhla, G. and Zhu, J. (2005). Detachment of multi species biofilm in circulating fluidized bed bioreactor. Biotechnol Bioeng *92*, 427–437.

Pavissich, J. P., Aybar, M., Martin, K. J. and Nerenberg, R. (2014). A methodology to assess the effects of biofilm roughness on substrate fluxes using image analysis, substrate profiling, and mathematical modelling. Water Sci Technol *69*, 1932–1941.

Percival, S. L., Knapp, J. S., Wales, D. S. and Edyvean, R. G. J. (1999). The effect of turbulent flow and surface roughness on biofilm formation in drinking water. Journal of Industrial Microbiology and Biotechnology *22*, 152–159.

Phoenix, V. R., Holmes, W. M. and Ramanan, B. (2008). Magnetic resonance imaging (MRI) of heavy-metal transport and fate in an artificial biofilm. Mineralogical Magazine *72*, 483–486.

Picioreanu, C., Kreft, J.-U. and van Loosdrecht, M. C. M. (2004). Particle-Based Multidimensional Multispecies Biofilm Model. Appl Environ Microbiol *70*, 3024–3040.

Picioreanu, C., van Loosdrecht, M. and Heijnen, J. J. (1998). A new combined differential-discrete cellular automaton approach for biofilm modeling: Application for growth in gel beads. Biotechnol Bioeng *57*, 718–731.

Picioreanu, C., van Loosdrecht, M. C. M. and Heijnen, J. (1997). Modeling the effect of oxygen concentration on nitrite accumulation in a biofilm airlift suspension reactor. Water Sci Technol *36*, 147–156.

Picioreanu, C., van Loosdrecht, M. C. M. and Heijnen, J. (1998). Mathematical modeling of biofilm structure with a hybrid differential-discrete cellular automaton approach. Biotechnol Bioeng *58*, 101–116.

Picioreanu, C., van Loosdrecht, M. C. M. and Heijnen, J. J. (2001). Two-dimensional model of biofilm detachment caused by internal stress from liquid flow. Biotechnol Bioeng *72*, 205–218.

Picioreanu, C., van Loosdrecht, M C and Heijnen, J. J. (2000). A theoretical study on the effect of surface roughness on mass transport and transformation in biofilms. Biotechnol Bioeng *68*, 355–369.

Piculell, M., Welander, T. and Jönsson, K. (2014). Organic removal activity in biofilm and suspended biomass fractions of MBBR systems. Water Sci Technol *69*, 55.

Plattes, M., Fiorelli, D., Gillé, S., Girard, C., Henry, E., Minette, F., O'Nagy, O. and Schosseler, P. M. (2007). Modelling and dynamic simulation of a moving bed bioreactor using respirometry for the estimation of kinetic parameters. Biochemical Engineering Journal *33*, 253–259.

Plattes, M., Henry, E. and Schosseler, P. M. (2008). A zero-dimensional biofilm model for dynamic simulation of moving bed bioreactor systems: Model concepts, Peterson matrix, and application to a pilot-scale plant. Biochem Eng J *40*, 392–398.

Priester, J. H., Horst, A. M., Van de Werfhorst, Laurie C, Saleta, J. L., Mertes, L. A. K. and Holden, P. A. (2007). Enhanced visualization of microbial biofilms by staining and environmental scanning electron microscopy. Journal of Microbiological Methods *68*, 577–587.

Purevdorj, B., Costerton, J. W. and Stoodley, P. (2002). Influence of Hydrodynamics and Cell Signaling on the Structure and Behavior of Pseudomonas aeruginosa Biofilms. Appl Environ Microbiol *68*, 4457–4464.

Ramanan, B., Holmes, W. M., Sloan, W. T. and Phoenix, V. R. (2013). Magnetic resonance imaging of mass transport and structure inside a phototrophic biofilm. Current microbiology *66*, 456–461.

Renslow, R., Lewandowski, Z. and Beyenal, H. (2011). Biofilm image reconstruction for assessing structural parameters. Biotechnol Bioeng *108*, 1383–1394.

Resat, H., Renslow, R. S. and Beyenal, H. (2014). Reconstruction of biofilm images: combining local and global structural parameters. Biofouling *30*, 1141–1154.

Särner, E. (1981). Removal of dissolved and particulate organic matter in high-rate trickling filters. Water Res *15*, 671–678.

Särner, E. (1986). Removal of Particulate and Dissolved Organics in Aerobic Fixed-Film Biological Processes. Journal (Water Pollution Control Federation) *58*, 165–172.

Särner, E. and Marklund, S. (1985). Influence of particulate organics on the removal of dissolved organics in fixed-film biological reactors. Water Sci Technol *17*, 15–26.

Schindelin, J., Arganda-Carreras, I., Frise, E., Kaynig, V., Longair, M., Pietzsch, T., Preibisch, S., Rueden, C., Saalfeld, S., Schmid, B., Tinevez, J.-Y., White, D. J., Hartenstein, V., Eliceiri, K., Tomancak, P. and Cardona, A. (2012). Fiji: an open-source platform for biological-image analysis. Nat Methods *9*, 676–682.

Shen, Y., Monroy, G. L., Derlon, N., Janjaroen, D., Huang, C., Morgenroth, E., Boppart, S. A., Ashbolt, N. J., Liu, W.-T. and Nguyen, T. H. (2015). Role of Biofilm Roughness and Hydrodynamic Conditions in Legionella pneumophila Adhesion to and Detachment from Simulated Drinking Water Biofilms. Environ Sci Technol *49*, 4274–4282.

Song, B. and Leff, L. G. (2006). Influence of magnesium ions on biofilm formation by Pseudomonas fluorescens. Microbiological research *161*, 355–361.

Srinandan, C. S., D'souza, G., Srivastava, N., Nayak, B. B. and Nerurkar, A. S. (2012). Carbon sources influence the nitrate removal activity, community structure and biofilm architecture. Bioresour Technol *117*, 292–299.

Stewart, P. S. (2003). Diffusion in Biofilms. J Bacteriol *185*, 1485–1491.

Stoodley, P., Boyle, J. D., DeBeer, D. and Lappin-Scott, H. M. (1999). Evolving perspectives of biofilm structure. Biofouling *14*, 75–90.

Stoodley, P., Boyle, J. D., Dodds, I. and Lappin-Scott, H. M., eds (1997). Consensus model of biofilm structure Cardiff, UK. BioLine.

Stoodley, P., Dodds, I., Boyle, J. D. and Lappin-Scott, H. M. (1998a). Influence of hydrodynamics and nutrients on biofilm structure. J Appl Microbiol *85 Suppl 1*, 19S–28S.

Stoodley, P., Lewandowski, Z., Boyle, J. D. and Lappin-Scott, H. M. (1998b). Oscillation characteristics of biofilm streamers in turbulent flowing water as related to drag and pressure drop. Biotechnol Bioeng *57*, 536–544.

Taherzadeh, D., Picioreanu, C. and Horn, H. (2012). Mass transfer enhancement in moving biofilm structures. Biophysical Journal *102*, 1483–1492.

Taherzadeh, D., Picioreanu, C., Kuttler, U., Simone, A., Wall, W. and Horn, H. (2010). Computational study of the drag and oscillatory movement of biofilm streamers in fast flows. Biotechnol Bioeng *105*, 600–610.

Tchobanoglous, G., Burton, F. L. and Stensel, H. D. (2003). Wastewater engineering: Treatment and reuse. McGraw-Hill series in civil and environmental engineering, 4th ed. edition, McGraw-Hill, Boston.

Telgmann, U., Horn, H. and Morgenroth, E. (2004). Influence of growth history on sloughing and erosion from biofilms. Water Environ Res *38*, 3671–3684.

van Loosdrecht, M., Eikelboom, D., Gjaltema, A., Mulder, A., Tijhuis, L. and Heijnen, J. J. (1995). Biofilm structures. Water Sci Technol *32*, 35–43.

van Nieuwenhuijzen, A. F., van der Graaf, J.H.J.M, Kampschreur, M. J. and Mels, A. R. (2004). Particle related fractionation and characterization of municipal wastewater. Water Sci Technol *50*, 125–132.

Villasenor, J. C., van Loosdrecht, M. C. M., Picioreanu, C. and Heijnen, J. (2000). Influence of different substrates on the formation of biofilms in a biofilm airlift suspension reactor. Water Sci Technol *41*, 323–330.

Wagner, M., Manz, B., Volke, F., Neu, T. R. and Horn, H. (2010a). Online assessment of biofilm development, sloughing and forced detachment in tube reactor by means of magnetic resonance microscopy. Biotechnol Bioeng *107*, 172–181.

Wagner, M., Taherzadeh, D., Haisch, C. and Horn, H. (2010b). Investigation of the mesoscale structure and volumetric features of biofilms using optical coherence tomography. Biotechnol Bioeng *107*, 844–853.

Wang, Q. and Zhang, T. (2010). Review of mathematical models for biofilms. Solid State Communications *150*, 1009–1022.

Wang, R., Wen, X. and Qian, Y. (2005). Influence of carrier concentration on the performance and microbial characteristics of a suspended carrier biofilm reactor. Process Biochemistry *40*, 2992–3001.

Wanner, O. (2006). Mathematical modeling of biofilms. IWA Publishing, London.

Wanner, O. and Gujer, W. (1986). A multispecies biofilm model. Biotechnol Bioeng *28*, 314–328.

Wanner, O. and Reichert, P. (1996). Mathematical modeling of mixed-culture biofilms. Biotechnol Bioeng *49*, 172–184.

Wichern, M., Lindenblatt, C., Lübken, M. and Horn, H. (2008). Experimental results and mathematical modelling of an autotrophic and heterotrophic biofilm in a sand filter treating landfill leachate and municipal wastewater. Water Res *42*, 3899–3909.

Wijeyekoon, S., Mino, T., Satoh, H. and Matsuo, T. (2004). Effects of substrate loading rate on biofilm structure. Water Res *38*, 2479–2488.

Wimpenny, J. W. and Colasanti, R. (1997). A unifying hypothesis for the structure of microbial biofilms based on cellular automaton models. FEMS Microbiology Ecology *22*, 1–16.

Wu, M., Sendamangalam, V., Xue, Z. and Seo, Y. (2012). The influence of biofilm structure and total interaction energy on Escherichia coli retention by Pseudomonas aeruginosa biofilm. Biofouling *28*, 1119–1128.

Wuertz, S., Bishop, P. L. and Wilderer, P. A. (2003). Biofilms in wastewater treatment: An interdisciplinary approach. IWA, London.

Xavier, J., Picioreanu, C. and Van, L. (2005a). A framework for multidimensional modelling of activity and structure of multispecies biofilms. Environmental Microbiology *7*, 1085–1103.

Xavier, J. d. B., Picioreanu, C. and van Loosdrecht, Mark C M (2005b). A general description of detachment for multidimensional modelling of biofilms. Biotechnol Bioeng *91*, 651–669.

Xi, C., Marks, D., Schlachter, S., Luo, W. and Boppart, S. A. (2006). High-resolution three-dimensional imaging of biofilm development using optical coherence tomography. J Biomed Opt *11*, 034001–1–6.

Yamamoto, T. and Ueda, S. (2013). Numerical simulation of biofilm growth in flow channels using a cellular automaton approach coupled with a macro flow computation. Biorheology *50*, 203–216.

Yang, L., Liu, Y., Wu, H., Hóiby, N., Molin, S. and Song, Z.-j. (2011). Current understanding of multi-species biofilms. International journal of oral science *3*, 74–81.

Yang, X., Beyenal, H., Harkin, G. and Lewandowski, Z. (2000). Quantifying biofilm structure using image analysis. Journal of Microbiological Methods *39*, 109–119.

Zhang, S., Wang, Y., He, W., Xing, M., Wu, M., Yang, J., Gao, N., Sheng, G., Yin, D. and Liu, S. (2013). Linking nitrifying biofilm characteristics and nitrification performance in moving-bed biofilm reactors for polluted raw water pretreatment. Bioresour Technol *146*, 416–425.

Zhu, D., Larin, K. V., Luo, Q. and Tuchin, V. V. (2013). Recent progress in tissue optical clearing. Laser Photon Rev *7*, 732–757.

Zielinski, J. S., Zielinska, A. K. and Bouaynaya, N., eds (2012). Three-Dimensional Morphology Quantification of Biofilm Structures from Confocal Laser Scanning Microscopy Images IACSIT Press, Singapore.
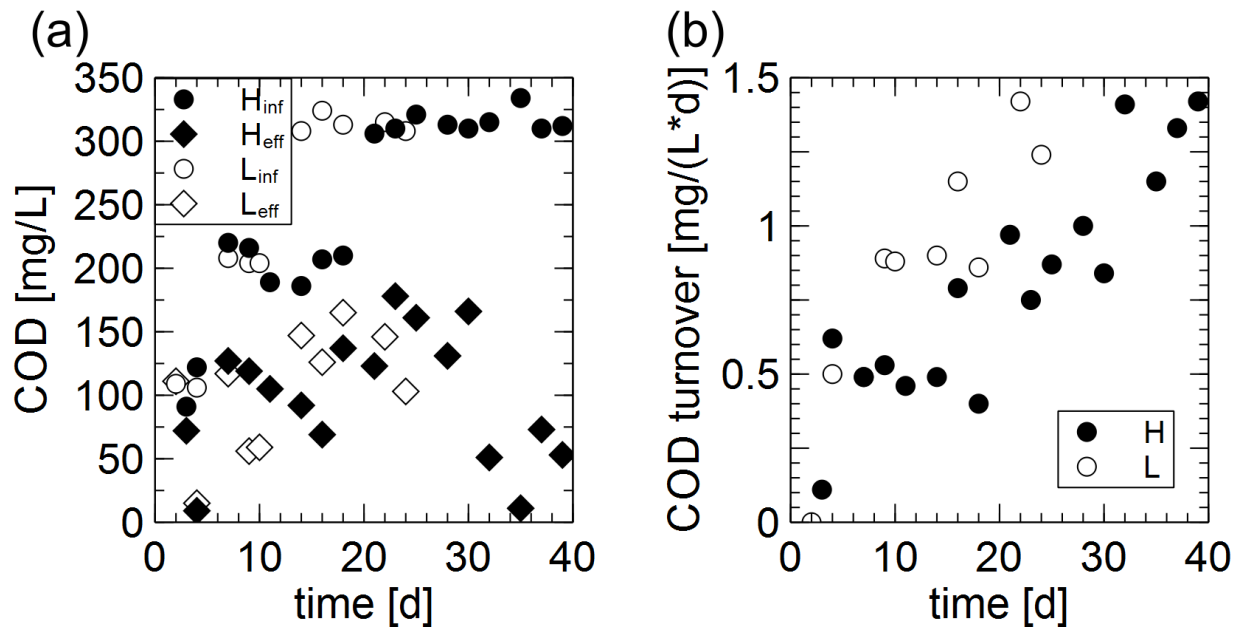
Appendix A

Appendix

A.1 Image analysis

Figure A.1: Reactor operation with respect to (a) COD concentration in the influent and effluent and (b) COD turnover rate for high (H, $250\,L\cdot h^{-1}$) and low (L, $150\,L\cdot h^{-1}$) aeration rate.

Table A.1: Spatial averaged Sherwood number ($\overline{Sh}$) calculated for different flow and substrates conditions for low biomass density for the flow through conditions ($15,000\,g \cdot m^{-3}$)

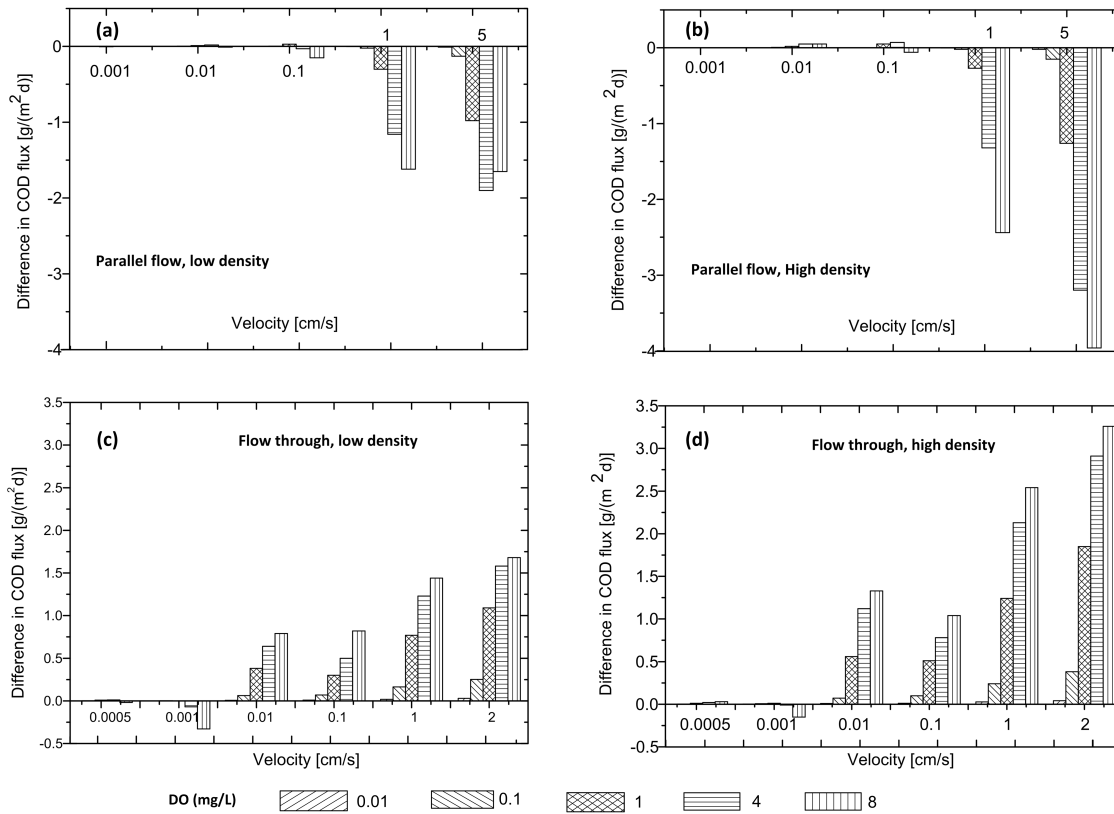| DO ($mg \cdot L^{-1}$)	$\mathbf{U}(cm \cdot s^{-1})$	0.0005	0.001	0.01	0.1	1	2
0.01	Real	2.06	3.69	13.5	29.4	82.7	134.1
	Simplified	4.09	7.22	22.6	51.6	129.1	182.0
0.1	Real	2.06	3.69	13.5	29.2	80.9	129.9
	Simplified	4.10	7.23	22.6	51.7	129.6	182.8
1	Real	2.09	3.72	13.2	27.8	74.0	115.5
	Simplified	4.13	7.31	22.8	52.3	131.8	186.3
4	Real	2.15	3.82	12.7	26.5	69.2	106.5
	Simplified	4.24	7.57	23.3	53.2	134.2	190.2
8	Real	2.23	3.93	12.5	25.9	67.6	103.7
	Simplified	4.40	7.88	23.6	53.7	135.7	192.7

Figure A.2: The difference in COD flux between the real and simplified geometries under different flow and substrate concentration conditions for parallel flow ((a) and (b)) and through flow ((c) and (d)) at low ((a) and (c)) and high ((b) and (d)) biomass density.
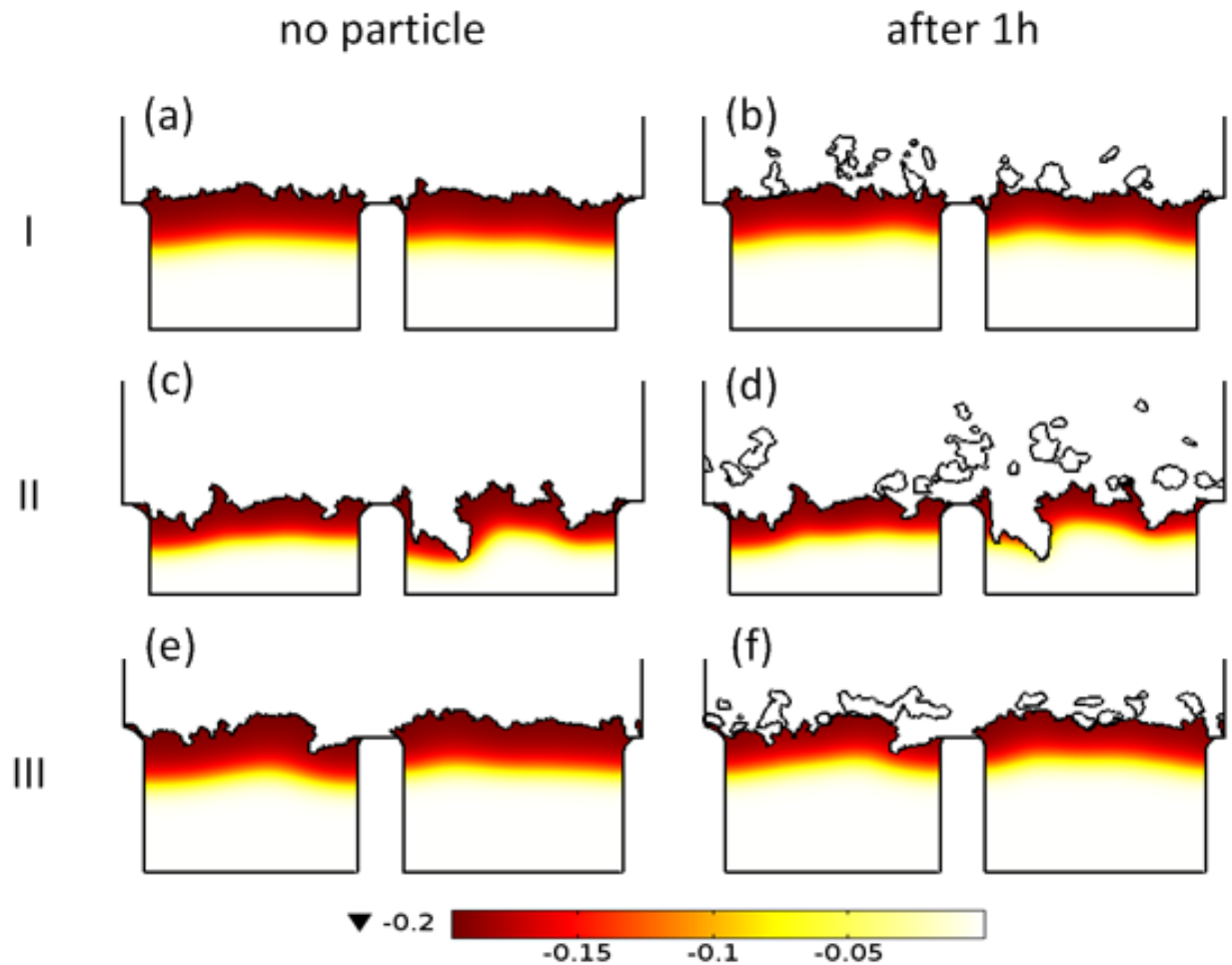
A.2 Simulation

A.3 Particle experiment

Figure A.3: The oxygen reaction rate $(g \cdot m^{-3} \cdot d^{-1})$ simulated before and after particle attachment for all the three particle fractions. The negative values indicate consumption of oxygen. The color legend applies to all. Similar to Figure 6.7, the figures were cropped to view only the biofilm and the particles. The width of each subfigure is $2.8\,mm$.

A.4   Verification of the contribution from the co-authors

Title: Investigating biofilm structure developing on carriers from lab-scale moving bed biofilm reactors based on light microscopy and optical coherence tomography

Journal: Bioresources Technology, $(2015)\,200$: $128-136$. *doi* : $10.1016/j.biortech$.2015.10.013

Authors :   Chunyan Li, Simon Felz, Michael Wagner, Susanne Lackner, Harald Horn

Position in the dissertation:

The content of the article has been included into Chapter 2.

Contribution of Chunyan Li (First author) (70%):

- Project idea and experiment planning
- Guidance on the biofilm cultivation process
- Guidance on image acquisition and processing
- Discussion on the results
- Rewrite and correction of the manuscript

Contribution of Simon Felz (Second author) (20%):

- Experiment setup and biofilm cultivation
- Image acquisition and processing
- Composition of the first draft manuscript
- Discussion on the results

Contribution of Michael Wagner (Third author) and Susanne Lackner (Fourth author) (8%):

- Project idea and guidance on the experiment process
- Discussion on the results
- Correction of the manuscript

Contribution of Harald Horn (Last author) (2%):

- Project idea
- Discussion on the results

- Correction of the manuscript

All the co-authors have agreed with the distribution of the contribution presented above.

Permission from Elsevier:

The authors can include their articles in full or in part in a thesis or dissertation for non-commercial purposes.

Source:$https://www.elsevier.com/about/company-information/policies/copyright/permissions$

Retrieved on $Jan. 20^{th}$, 2016

Title: Assessing the influence of biofilm surface roughness on mass transfer by combining optical coherence tomography and two-dimensional modeling

Journal :   Biotechnology and Bioengineering (2016). In press. *doi* : $10.1002/bit.258$

Authors :   Chunyan Li, Michael Wagner, Susanner Lackner, Harald Horn

Position in the dissertation:

The content of this article has been included in Chapter 3.

Contribution of Chunyan Li (First author) (85%):

- Project idea, experiment planning, biofilm cultivation
- Biofilm image acquisition and processing
- Model setup and simulation
- Discussion on the results
- Writing of the manuscript

Contribution of Michael Wagner (Second author) (5%):

- Project idea and guidance on image acquisition and processing
- Discussion on the results
- Correction of the manuscript

Contribution of Susanne Lackner (Third author) (5%):

- Project idea and guidance on model setup
- Discussion on the results
- Correction of the manuscript

Contribution of Harald Horn (Last author) (5%):

- Project idea and guidance on model setup
- Discussion on the results
- Correction of the manuscript

All the co-authors have agreed with the distribution of the contribution presented above.

Permission obtained from Wiley:

Permission is granted for you to use the material requested for your thesis/dissertation subject to the usual acknowledgements (author, title of material, title of book/journal, ourselves as publisher) and on the understanding that you will reapply for permission if you wish to distribute or publish your thesis/dissertation commercially. You must also duplicate the copyright notice that appears in the Wiley publication in your use of the Material; this can be found on the copyright page if the material is a book or within the article if it is a journal.

Permission is granted solely for use in conjunction with the thesis, and the material may not be posted online separately.

Any third party material is expressly excluded from this permission. If any of the material you wish to use appears within our work with credit to another source, authorisation from that source must be obtained.

Jan. 21st, 2016